Model-based design of solar thermal power plants

Dissertation

zur Erlangung des Doktorgrades an der Fakultät für Mathematik, Informatik und Naturwissenschaften der Universität Hamburg vorgelegt am Fachbereich Mathematik von

Hamzah Bakhti

aus Al-Huceima, Marokko

Hamburg, Januar 2024

Hiermit erkläre ich an Eides statt, dass ich die vorliegende Dissertationsschrift selbst verfasst und keine anderen als die angegebenen Quellen und Hilfsmittel benutzt habe.

Hamburg, den 15.1.2024

Unterschrift

Betreuer.

Prof. Dr. Ingenuin Gasser

Gutachter.

Prof. Dr. Ingenuin Gasser (Erstgutachter)
Dr. Camilla Nobili (Zweitgutachterin)
Dr. Alessandro Coclite (Drittgutachter)

Prüfungskommission.

Prof. Dr. Ulf Kühn (Vorsitz)
Prof. Dr. Winnifried Wollner (stellv. Vorsitz)
Priv.-Doz. Dr. Philipp Lücke (Schriftführung)
Prof. Dr. Ingenuin Gasser (Erstgutachter)
Dr. Camilla Nobili (Zweitgutachterin)

Datum der Disputation: 28.03.2024

Eigenanteilserklärung

This dissertation is based on four co-authored publications and pre-publications, listed in the bibliography as [1–4]:

[1] Bakhti, H., I. Gasser, S. Schuster, and E. Parfenov, "Modelling, simulation and optimisation of parabolic trough power plants," European Journal of Applied Mathematics, vol. 34, no. 3, 592–615, 2023.

[2] Bakhti, H. and I. Gasser, "Modeling and simulation of parabolic trough collectors using nanofluids: Application to NOOR I plant in Ouarzazate, Morocco," Lecture Notes in Computational Science and Engineering, vol. 148, pp. 21–33, 2023.

[3] Bakhti, H. and I. Gasser, "Network-based analysis and optimization of parabolic trough power plant operating with nanofluids: Application to Ouarzazate solar power station in Morocco," Submitted to International Journal of Applied and Computational Mathematics, Springer Nature, 2023.

[4] Bakhti, H. and I. Gasser, "Modeling and simulation of parabolic trough power plant using molten salt: Case study of NOOR I solar power station in Ouarzazate, Morocco," in The 9th International Conference on Modeling, Simulation and Applied Optimization, AIP Conference Proceedings, 2023.

Paper [1] was a collaboration with roughly equal contributions of the four authors; papers [2–4] were collaborations in which the majority of the work was done by Hamzah Bakhti. In the following, the contributions of the co-authors Ingenuin Gasser, Evgeny Parfenov, and Susanne Schuster are declared.

The *General Introduction* was conceptualized and written by Hamzah Bakhti with content derived from the co-authored publications.

This chapter is a collaboration of Ingenuin Gasser and the candidate. The overwhelming majority of the work was done by the candidate.

Chapter 1 was conceptualized and written by Hamzah Bakhti with content derived from the co-authored publications, in particular [1].

This chapter is a collaboration of Ingenuin Gasser and the candidate. The overwhelming majority of the work was done by the candidate.

Chapter 2 was conceptualized and written by Hamzah Bakhti with content derived from the co-authored publications, in particular [1–3].

This chapter is a collaboration of Ingenuin Gasser, Evgeny Parfenov, Susanne Schuster, and the candidate. More than half of the work of the chapter was done by the candidate and Ingenuin Gasser, Evgeny Parfenov, Susanne Schuster made minor contributions.

Chapter 3 was conceptualized and written by Hamzah Bakhti with with content derived from the co-authored publications, in particular [1, 3].

This chapter is a collaboration of Ingenuin Gasser, Susanne Schuster, and the candidate. More than half of the work of the chapter was done by the candidate and Ingenuin Gasser, Susanne Schuster made minor contributions.

Chapter 4 was conceptualized and written by Hamzah Bakhti with content derived from the co-authored publications.

This chapter is a collaboration of Ingenuin Gasser and the candidate. The overwhelming majority of the work was done by the candidate.

The *Conclusion* was conceptualized and written by Hamzah Bakhti with with content derived from the co-authored publications, in particular [3].

This chapter is a collaboration of Ingenuin Gasser and the candidate. The overwhelming majority of the work was done by the candidate.

English Summary

This thesis studies the dynamics of parabolic trough power plants (PTPPs) with the objective of optimizing their performance. The present study delves into the complexities of heat transfer flow within these power plants, by developing mathematical models to find a balance between comprehensive descriptions of physical phenomena and computational efficiency.

The use of various heat transfer fluids (HTFs) within the PTPPs, such as thermal oil, nanofluids and molten salt, is a major aspect of the investigation. Therminol VP-1, a type of thermal oil, is initially used in a complete thermo-fluid model of a network system with spatio-temporal dependency that is derived following various asymptotic processes that simplifies the model significantly.

Concerning nanofluids, the integration of nanoparticles into a basefluid, usually thermal oil, allows the simulation of the effects of different nanoparticles such as Copper Oxide, Alumina, and Titanium Oxide. This research aims to analyze the nanofluids impact on the thermal performance and energy efficiency. Results obtained from NOOR I power plant in Morocco reveal that adding nanoparticles, even in small volume fractions, enhances both energetic and exergetic efficiencies. Such enhancement however, is accompanied by a slight increase in friction loss.

This study further examines the use of molten salt as an alternative HTF in PTPPs. A network-based mathematical model is introduced to describe the fluid dynamics of molten salt in the solar field of these plants. The data collected from NOOR I power plant is utilized in the creation of simulations that closely replicate real-world scenarios, emphasizing the advantages of this approach over traditional single-collector models.

In addition to modeling, the thesis delves into optimization techniques to enhance the thermal efficiency of PTPPs. The formulation of optimization problems and the employment of suitable control variables serve the purpose of maximizing the energy output of parabolic solar systems. Parameter studies based on the application of optimization algorithm to the presented models demonstrate a promising boost to the thermal output of PTPPs.

The thesis also comprises various simplified simulation models that are presented and compared for single-pipe case, row of series-connected PTCs, and larger network

configurations resembling real-world solar fields as in the case of NOOR I power plant. Each case study provides valuable insights into computational costs associated with different models, shedding light on optimal approaches for modeling and simulating PTPPs.

Ultimately, this thesis offers a comprehensive understanding of modeling, simulation, and optimization of PTPPs, highlighting the potential of network-based models using advanced types of HTFs that would immensely enhance the efficiency of these power plants.

Keywords: Parabolic Trough Power Plant; Parabolic Trough Collector; Heat Transfer Flow; Heat Transfer Fluid; Network System; Therminol VP-1; Nanofluid; Molten Salt; Modeling; Simulation; Optimization; Energy efficiency.

Deutsche Zusammenfassung

Diese Arbeit untersucht die Dynamik von Parabolrinnenkraftwerken (PTPPs) mit dem Ziel, deren Leistung zu optimieren. Die vorliegende Studie befasst sich mit der Komplexität des Wärmeübertragungsflusses in diesen Kraftwerken, indem mathematische Modelle entwickelt werden, um einen Kompromiss zwischen umfassenden Beschreibungen physikalischer Phänomene und Recheneffizienz zu finden.

Der Einsatz verschiedener Wärmeübertragungsflüssigkeiten (HTFs) innerhalb der PTPPs, wie Spezialöle, Nanofluide und geschmolzenes Salz, ist ein wichtiger Aspekt der Untersuchung. Therminol VP-1, ein Spezialöl, wird zunächst in einem komplexen Thermofluidmodell eines Netzwerksystems mit räumlich-zeitlicher Abhängigkeit verwendet. Verschiedene asymptotische Prozessen vereinfachen das Modell erheblich.

Bei Nanoflüssigkeiten ermöglicht die Integration von Nanopartikeln in eine Grundflüssigkeit, in der Regel Thermonol VP-1, die Simulation der Auswirkungen verschiedener Nanopartikel wie Kupferoxid, Aluminiumoxid und Titanoxid. Ziel dieser Forschung ist es, die Auswirkungen von Nanoflüssigkeiten auf die thermische Leistung und Energieeffizienz zu analysieren. Ergebnisse des Kraftwerks NOOR I in Marokko zeigen, dass die Zugabe von Nanopartikeln, selbst in kleinen Volumenanteilen, sowohl die energetische als auch die exergetische Effizienz steigert. Eine solche Verbesserung geht jedoch mit einem leichten Anstieg des Reibungsverlusts einher.

Diese Studie untersucht weiter die Verwendung von geschmolzenem Salz als alternatives HTF in PTPPs. Zur Beschreibung der Fluiddynamik geschmolzenen Salzes im Solarfeld dieser Anlagen wird ein netzwerkbasiertes mathematisches Modell eingeführt. Die vom Kraftwerk NOOR I gesammelten Daten werden zur Erstellung von Simulationen genutzt, die reale Szenarien genau nachbilden und die Vorteile dieses Ansatzes gegenüber herkömmlichen Einzelkollektormodellen hervorheben.

Zusätzlich zur Modellierung befasst sich die Arbeit mit Optimierungstechniken zur Verbesserung der thermischen Effizienz von PTPPs. Die Formulierung von Optimierungsproblemen und der Einsatz geeigneter Steuergrößen dienen der Maximierung der Energieausbeute parabolischer Solaranlagen. Parameterstudien, die auf der Anwendung von Optimierungsalgorithmen auf die vorgestellten Modelle

basieren, zeigen eine vielversprechende mögliche Steigerung der Wärmeleistung von PTPPs.

Die Arbeit umfasst auch verschiedene vereinfachte Simulationsmodelle, die für den Fall eines Einzelrohrs, einer Reihe in Reihe geschalteter PTCs und größerer Netzwerkkonfigurationen, die realen Solarfeldern ähneln, wie im Fall des Kraftwerks NOOR I, vorgestellt und verglichen werden. Jede Fallstudie liefert wertvolle Einblicke in die mit verschiedenen Modellen verbundenen Rechenkosten und gibt Aufschluss über optimale Ansätze zur Modellierung und Simulation von PTPPs.

Letztendlich bietet diese Arbeit ein umfassendes Verständnis der Modellierung, Simulation und Optimierung von PTPPs und unterstreicht das Potenzial netzwerkbasierter Modelle unter Verwendung fortschrittlicher Arten von HTFs, die die Effizienz dieser Kraftwerke enorm steigern können.

Schlüsselwörter: Parabolrinnenkraftwerk; Parabolrinnenkollektor; Wärmeübertragungsfluss; Wärmeübertragungsflüssigkeit; Netzwerk System; Therminol VP-1; Nanofluid; Geschmolzenes Salz; Modellieren; Simulation; Optimierung; Energieeffizienz.

Acknowledgements

Throughout the writing of this dissertation I have received a great deal of support and assistance from my wife, family, friends, academics and professionals.

A special thanks to my parents, Naima Menouar Menari and Mohammed Bakhti, my wife, Najat Magouh, and my siblings, Mossaâb, Zainab, Zoubair and Ahmad Yassin, for their love and the unconditional support. You are always there for me.

I would like also to thank my thesis supervisor, Prof. Ingenuin Gasser, for his advice, support, and the patience during my PhD study. Special thanks go to Susanne Schuster and Evgeny Parfenov for the fruitful collaboration in my first year.

I could not have completed this dissertation without the support of my colleagues and friends within the RTG 2583 who provided stimulating discussions as well as happy distractions to rest my mind outside of my research.

Finally, I acknowledge the support by the Deutsche Forschungsgemeinschaft (DFG) within the Research Training Group GRK 2583 "Modeling, Simulation and Optimization of Fluid Dynamic Applications".

Contents

List of Figures

List of Tables

General Introduction

0.1 Context and Background

0.1.1 Energy Demand and Environmental Imperatives

The world's energy consumption has been on a steady rise, driven by both industrialization and urbanization. However, this increasing demand for energy has come at a significant environmental cost, primarily due to the use of fossil fuels, which contribute to climate change and environmental pollution. To mitigate these impacts, there is a critical need to transition away from traditional non-renewable energy sources and embrace renewable alternatives.

In December 2019 the European Commission established a EU binding renewable energy target for 2030 of at least 32% and for becoming a climate neutral continent by 2050 [5]. Available data of the energy consumption in EU shows that the share of renewable energy in Germany is linearly increasing and reached the 19% mark in 2021 compared to around 22% in the EU [6], as shown in Fig. 1.

Solar radiation emerges as a key renewable energy source with immense potential. It provides a clean and abundant energy that can be harnessed for various applications, including heating and electricity generation. Solar power plants, particularly those utilizing parabolic trough technology, offer an efficient means of converting solar radiation into electricity on a significant scale [7, 8].

0.1.2 Solar Energy and Parabolic Trough Technology

Solar energy is a sustainable and renewable source that holds great promise in mitigating the world's energy challenges. Among the various technologies used to harness solar energy, parabolic trough power plants (PTPPs) has become on of most pre-eminent, reliable and efficient methods over the past few decades. The

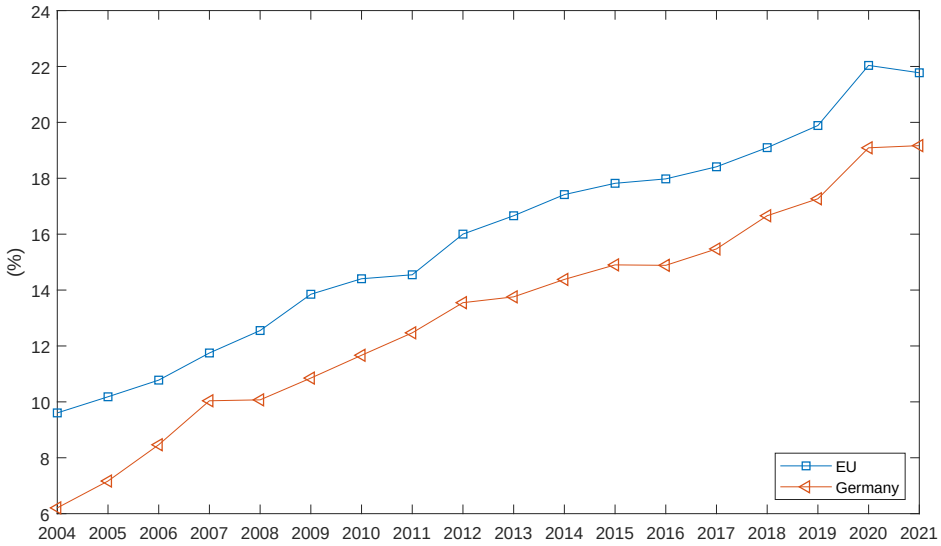

FIG. 1: Share of renewable energy in gross final energy consumption in German and EU [6].

PTPP's mode of operation depends on curved mirrors that concentrate sunlight onto linear absorbers, thereby generating heat. This heat is then used to produce steam, which drives turbines to generate electricity [9]. The reflectors in PTPPs are meticulously designed to track the sun's movement, ensuring maximum efficiency throughout the day. The heat transfer fluid (HTF) circulates through a network of tubes within the system, storing and transporting heat to facilitate the power generation process.

According to the NREL database of existing and planned power plants, this prominent type of power plant can be found in many places all over the world, [10]. As of the date of this research, thousands of gigawatts of power already have been made available by parabolic trough power stations worldwide. A typical modern parabolic trough power plant has an electricity generation capacity in the order of magnitude $10^2 - 10^3, MW$.NOOR I power plant in Morocco is often referred to throughout this thesis.

0.1.3 The Moroccan Solar Initiative and NOOR I Power Plant

Recent publications show that investments in the renewable energy sectors in the Middle East and North Africa region can be very useful for the EU to achieve its targets by 2050 [11, 12]. Trieb et al. [13] provides a detailed analysis in the examination of the potential of the Middle East and North Africa region for importing concentrated solar power and its significance in shaping Europe's future energy systems. The work of Komendantova et al. [14] investigates the potential investment risks of the development of large-scale solar power plants in the North Africa region with regard to the European renewable power production.

FIG. 2: Google maps satellite image of NOOR I plant in Ouarzazate, Morocco [1].

The Moroccan Solar Initiative, led by the Moroccan Agency For Solar Energy (MASEN) [15], represents a genuine effort to harness solar power in the region. This initiative aims to develop multiple solar power plants across different regions,

with NOOR I being the first prominent step. NOOR I, as seen from Google satellite image in Fig. 2, operational since 2016, stands as a testament to the successful implementation of parabolic trough collectors (PTCs) in solar power generation. The power complex in Ouarzazate is part of Morocco's broader plan to integrate renewable energy into its energy portfolio, showcasing the country's commitment to sustainability. According to Aqachmar et al. [16], NOOR I relies on thermal oil as the HTF and has significantly contributed to Morocco's solar power generation capacity . Furthermore, by conducting a thorough analysis of the major renewable energy projects in Morocco, Boulakhbar et al. [17] evaluates the current state of the Moroccan energy strategy.

0.2 State of Solar Power Technology

A parabolic trough power plant is a type of solar thermal power plant that employs curved mirrors to concentrate sunlight onto a receiver tube located at the focal point of the parabolic shape. The receiver tube contains a fluid that is heated by the collected sunlight, which then flows through a heat exchanger to generate steam. The parabolic trough power plant has a history that dates back to the 1800s, when the parabolic trough reflector was invented by French engineer Auguste Mouchout [18]. However, it wasn't until the 1970s and 80s that parabolic trough technology began to be developed for large-scale power generation. The first parabolic trough power plant was built in the Mojave Desert in California in 1984 [19], and it is still successfully operating for commercial purposes to this date[20]. PTPPs has already reached a commercial level on a bigger size in the last few decades. In comparison to present-day models of PTPPs, which utilize advanced types of HTFs within the collectors such as thermal oil or Molten Salt [9, 21], early models generate steam directly [22, 23]. In addition, the low cost of fossil fuels has never affected nor thwarted the significant investments in solar thermal power technology [24]. For the above mentioned reasons, and for current circumstances that created an instability in the price of fossil fuels, a renewed interest in this technology has come to light recently. This shift has significantly improved the efficiency and effectiveness of these solar power plants. With advancements in materials, engineering, and understanding of solar thermal dynamics, parabolic trough technology has matured into a commercially viable option for large-scale solar power generation [22]. This technology is still a subject

of ongoing development and improvement, while larger plants are now being built around the globe. Noor I, a gigantic PTPP in Morocco, has a capacity production equal to 160 MW, making it one of the largest solar power plant in the world [25]. Today, parabolic trough power plants are one of the most widely deployed type of solar thermal power plant in the world, with over 60 plants in operation globally [10].The continuity of research and refinement regarding the PTPPs makes this technology very desirable, driving its adoption and commercial success to unprecedented levels.

In recent years, there have been growing efforts to enhance the performance of PTPPs, aiming to maximize energy output and improve overall efficiency. Works in the literature on parabolic trough power plants already exist, where various aspects are thoroughly studied and discussed. Fernandez-Garc et al. study collectors in a general overview article [26], while other literature compares the parabolic trough and the heliostat technology [27] using space independent models for a single pipe. The study and comparison of the parabolic trough plants with thermo-fluids to direct steam generating power plants are also present in the literature [28, 29]. A number studies investigate the benefit of using innovative HTF's such as molten salt [30–32] and nanofluids [33–35]. Nanofluids, in particular, have shown promise in improving heat transfer rates due to the enhanced thermal properties brought about by the nanoparticles [21, 36]. In a recent review paper by Nawsud et al. [37], the potential of nanofluids in PTCs is presented where better performance is recorded in the case of using such nanofluids. Furthermore, for medium and high temperature PTCs, Allouhi et al. [38] investigates the effect of suspending various types of nanoparticles in the base HTF by doing heat transfer flow simulations using a one-dimensional mathematical model.

Many models that focus on the detailed cross-sectional physics and dynamics in a tube are also presented, i.e. in [39–41]. Literature also includes works that provides a space independent thermal analysis for a single pipe, in [23], with related optimization tasks in [42]. In addition, other investigations based on simple algebraic models or space independent models are done, with the purpose of optimizing economic [43], control [44] or structural [45, 46] aspects. Network simulations based on algebraic models can also be found in [47], optimization based on complex 3D models can be found in [48], while thermo-fluid dynamic simulations with optimization tasks on tailored software tools such as *ColSimCSP* can be found in [49]. Finally, Research has identified various control parameters such as inlet temperature, mass flow rate of the HTF, wind speed, pressure or

vacuum in the annulus, solar irradiance, and nanoparticle concentration, as crucial factors for improving PTPP performance [38, 50].

0.3 Challenges and Opportunities

0.3.1 Modeling, Simulation and Optimization of PTPPs

Modeling and simulation of parabolic trough power plants is an important and practical tool for understanding and optimizing their performance. It involves creating a mathematical model of the power plant, which can be used to simulate its behavior under different operating conditions. This can help identify areas where improvements can be made, such as optimizing the design of the parabolic trough mirrors or the performance of the heat transfer fluid. Modeling and simulation can also be used to evaluate the impact of different climatic and operating factors on plant performance [1]. By simulating plant behavior under different scenarios, it is possible to identify potential issues before they occur and optimize the performance of the plant. Overall, modeling, simulation and optimization are essential tools for designing, operating, and improving parabolic trough power plants, thus helping to ensure they provide a reliable and cost-effective source of renewable energy.

0.3.2 Single Tube vs. Network Tubes Analysis

Realized research has predominantly focused on the analysis of individual PTCs, offering valuable insights into their behavior. However, this approach overlooks the complex interplay of variables and dynamics present in a network system of interconnected PTCs [37]. Understanding the behavior of PTPPs as networked systems is essential for comprehensive optimization. A discernible research gap exists in the in-depth analysis of network systems comprising multiple PTCs, a prevalent feature of large-scale solar power generation. These networked PTPPs require a thorough understanding of their dynamics, thermal interactions, and overall behavior for performance optimization [37]. To maximize energy output, comprehensive modeling and simulation studies of these networked systems are required.

0.3.3 Complex Interplay of Variables

Generally, to enhance the performance of PTCs, various theoretical and numerical studies were conducted to demonstrate the impact of environmental and operational parameters on the thermal efficiency of such systems. The performance of PTPPs is influenced by a number of interdependent variables, including but not limited to inlet velocity, temperature, HTF type, system tubes diameter. The complex interplay of these variables compels the need for a comprehensive and systemic approach to optimization. With the objective of designing high-performance and more cost effective PTCs, the effect of geometric parameters on the performance of PTC system is studied by Cheng et al. [51] using combined numerical and optimization techniques. In the work of Padilla et al. [50] and Allouhi et al. [38] the considered optimization parameters are the inlet temperature, mass flow rate of the HTF, wind speed, pressure or vacuum in annulus, solar irradiance and nanoparticle concentration.

0.3.4 Heat Transfer Fluids (HTFs) in Network Systems

Recently, scientists introduced various improvements to PTPPs in order to enhance the performance and maximize the energy output. PTCs typically work with classical thermal fluids. Various studies investigate the benefit of using innovative HTF's such as molten salt [30–32] and nanofluids [33–35]. Numerous recent papers show the advantage of adding nanoparticles to the base HTF in order to improve the heat transfer in PTCs [21, 36]. A recent review paper by Nawsud et al. [37] demonstrates the potential of nanofluids in PTCs for their perceptible superior performance in application. Furthermore, for medium and high temperature PTCs, Allouhi et al. [38] investigates the effect of suspending various types of nanoparticles in the base HTF by running heat transfer flow simulations using a one-dimensional mathematical model. One interesting result is that the thermal efficiency of the PTC slightly increases when using nanofluids. Nevertheless, aside from studies on a single PTC, there is still a scarcity of studies on modeling, simulation and optimization of PTPP's in more realistic large network systems. Research on network systems is therefore required for a better understanding of the application of nanofluids or of the thermal performance in PTPP.

Molten salt is another type of liquid used as a heat transfer fluid in some parabolic trough power plants. The use of molten salt in solar thermal power generation dates back to 1990s, when the Solar Energy Research Institute (SERI) in the US constructed the Solar Two project, the first large-scale molten salt solar power plant [52]. In a parabolic trough power plant, molten salt has several advantages over other heat transfer fluids due to the high specific heat capacity and the high boiling point. During periods of high solar radiation, molten salt is heated to a high temperature by the concentrated sunlight, and then stored in insulated tanks. When electricity is required, molten salt is circulated through a heat exchanger, generating steam that drives a turbine to produce electricity. The use of molten salt allows parabolic trough power plants to produce electricity continuously, even during periods of low sunlight or at night, rendering them more reliable for renewable energy production [21].

0.4 Objectives and Scope

This thesis aims to develop complete thermo-fluid network-based models with time and/or spatial dependency starting from the work of Susanne Schuster [53], Evgeny Parfenov [54] and Ingenuin Gasser [55–58]. The models are the result of various asymptotic processes that simplify the model significantly. Appropriate node conditions for the network are assumed in the study and the models are robust and fast in the simulations. Based on the abovementioned, optimization attempts are feasible with reasonable effort. To our knowledge, the models presented here are unique and one of the most complete models available to describe a parabolic trough power station. In particular, the models are based on first principal thermo-fluid equations and not exclusively consider energy balances but also set the ground for a wide range of applicability. Adaptive numerical techniques are then presented for the proposed models [1–4].

Optimizing PTPP performance is another primary objective in this thesis, with the aim to maximize the output energy by formulating a mathematical optimization problem considering real-world parameters and operational conditions. By exploring various parameters such as inlet velocity, temperature, HTF type, and network structure, this research seeks to identify the optimal configurations that lead to enhanced energy output [1, 3].

This thesis also looks into the impact of different HTFs, such as Therminol VP-1, nanofluids and molten salt, on the thermal efficiency and energy output of PTPPs. Concerning nanofluids, Copper Oxide, Alumina and Titanium Oxide are three types of nanoparticles in the HTF, and in different concentrations, that are analyzed in order to understand how they affect the heat transfer dynamics within the collectors, subsequently influencing the overall performance [1–4].

The present thesis aims as well to enhance the real-world applicability of PTPP models by incorporating data from the NOOR I power plant and the specific climatic conditions of Ouarzazate, Morocco. The proposed models are validated against real-world data for accuracy and applicability, ensuring that the research findings can be effectively translated into practical implementations for improved PTPP performance.

Chapter 1

Parabolic Trough Power Plants

1.1 Introduction

Parabolic trough power plants are a significant advancement in the field of solar energy technology, harnessing the sun's energy to generate electricity. As shown in Fig. 1.1, PTPP is a solar thermal power plant that usually consists of: solar collector field, thermal storage tanks, heat exchanger, turbine/generator system [59]. This chapter presents a comprehensive exploration of parabolic trough power plants, covering their solar field design, components, heat transfer mechanisms, the Moroccan solar energy initiative, and finally, the modeling, simulation and optimization of such energy systems.

1.2 Solar Field Design

Parabolic trough power plants stand as one of the pioneering technologies in solar thermal energy generation. A crucial element of these power plants is the solar field, which constitutes the foundation for effective energy capture and conversion. Solar field is a pivotal player in various solar technologies, the solar field serves as the stage where the process of harnessing solar radiation unfolds [61].

At its core, the solar field comprises a sophisticated ensemble of meticulously engineered elements for the purpose of maximizing the capture, conversion, and utilization of solar energy. These elements include parabolic trough structures, receiver tubes, support and tracking systems, and others [62]. These elements represent the integration of cutting-edge technology, scientific precision, and sustainable engineering practices aimed at optimizing the thermal output and

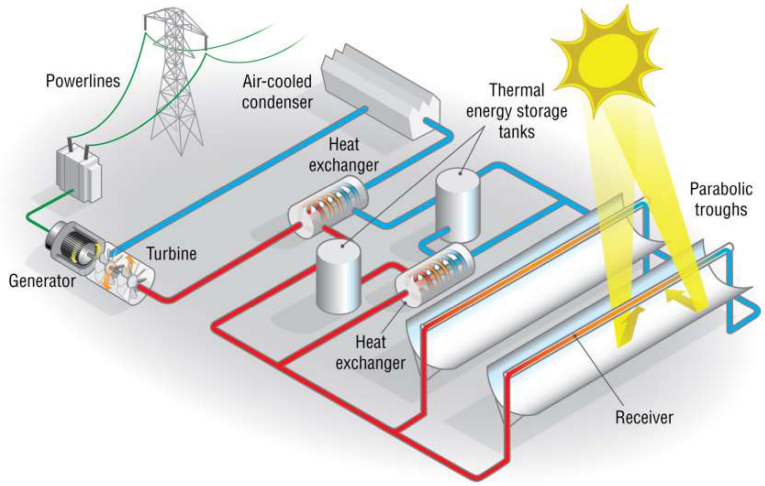

FIG. 1.1: Parabolic trough power plant [60]

enhancing the efficiency of PTPPs in order to unlock the immense potential of the sun as a clean energy source. This chapter delves into the design principles and considerations governing the solar field in parabolic trough power plants.

1.2.1 Parabolic Trough Structure

The parabolic trough structure constitutes the backbone of a solar field within a parabolic trough power plant. For an efficient harness of solar energy, these curved reflective surfaces play a pivotal role in concentrating sunlight onto a focal line, where receiver tubes are positioned to capture and convert the solar energy into thermal power [61, 62].

The materials chosen for these troughs are critical for their reflective properties and durability. High-quality reflective materials, such as specialized coatings on metal surfaces or advanced polymers, are selected to endure harsh weather conditions and maintain reflective efficiency over their operational lifetime [63]. The construction process involves assembling these materials onto a supporting structure, typically made of steel or other robust materials, ensuring the troughs maintain their shape and orientation [64].

Maintaining the reflective surfaces is crucial for optimal performance. Regular maintenance involves cleaning to remove dust, debris, or other obstructions that

FIG. 1.2: Solar-tracking parabolic trough collectors part of NOOR I power plant in Morocco [1, 65].

might hinder sunlight absorption. Protective coatings applied to the reflective surfaces not only enhance reflectivity but also protect against corrosion, extending the life of the troughs [66].

Innovation in parabolic trough design continues to evolve. Ongoing research explores newer materials and coatings that improve reflectivity, durability, and cost-effectiveness. Efforts are underway to simplify installation processes and

reduce maintenance requirements, making these solar field structures more accessible and adaptable to various environmental conditions [63].

The future of parabolic trough structures lies in their continued refinement and integration into larger energy systems. Efforts are being made to combine them with energy storage solutions, enhancing their capacity to provide consistent power even during periods of low sunlight [67]. Furthermore, the quest for more modular and scalable designs aims to facilitate their integration into diverse geographical locations and operational settings.

1.2.2 Receiver Tubes

One of the core components of the solar field are receiver tubes, where solar energy is absorbed and converted into heat. Receiver tubes endure extreme conditions, including high temperatures and thermal cycling. Thus, they are often fabricated from high-quality, corrosion-resistant materials such as stainless steel or alloys capable of withstanding temperatures upwards of 600°C (1112°F). The material's ability to efficiently transfer absorbed heat to the working fluid is crucial for optimal energy conversion [63].

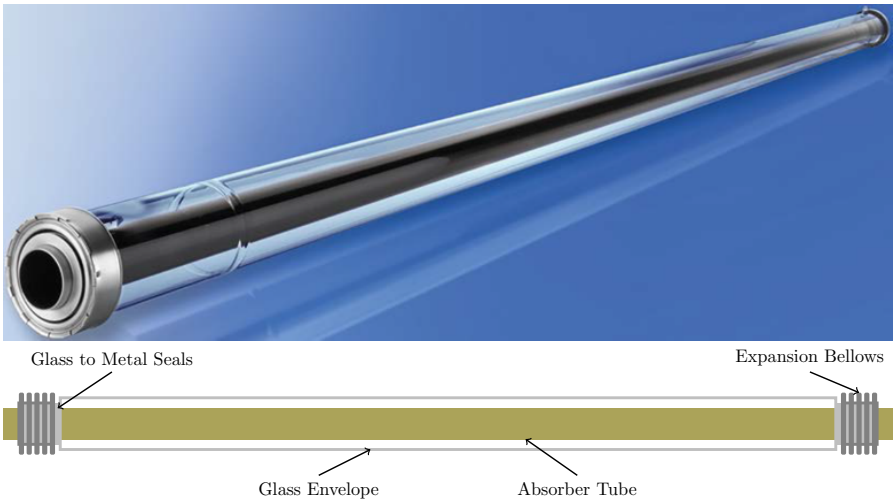

FIG. 1.3: Sketch of a receiver tube from a typical parabolic trough collector [68].

Enhancing the absorption of solar radiation is vital for efficient energy conversion. Receiver tubes are coated with selective absorber coatings that maximize the absorption of sunlight while minimizing radiative and convective losses. These coatings are tailored to have high absorptance (ability to absorb sunlight) and low emittance (ability to radiate absorbed heat) [69].

The geometry of receiver tubes influences the surface area exposed to sunlight and the heat transfer characteristics. Engineers consider factors such as tube diameter, length, and geometry to optimize the absorption of sunlight and the transfer of thermal energy to the heat-transfer fluid circulating within the tubes [63].

Receiver tubes contain a heat-transfer fluid that absorbs the heat from concentrated sunlight and carries it to the power plant's steam generator. The choice of HTF is critical, considering its thermal stability, heat capacity, and freezing/boiling points. Common fluids include steam, synthetic oils or molten salts in advanced designs [63].

To maximize energy conversion efficiency, minimizing heat losses from the receiver tubes is imperative. Insulation layers and vacuum-sealed receiver tubes are employed to reduce conductive and convective heat losses, ensuring that most of the captured solar energy is effectively transferred to the HTF [63].

Receiver tubes should be robust and resistant to degradation from prolonged exposure to high temperatures, weather conditions, and thermal stresses. Materials and coatings are chosen to withstand these harsh environments, thereby reducing maintenance needs and extending the operational life of the solar field [61, 63].

Accumulation of dust, dirt, or other contaminants on the receiver tubes can diminish their efficiency. Implementation of automated or manual cleaning systems, such as brushes or air jets, helps to maintain the reflective and absorptive properties of the tubes, ensuring optimal sunlight absorption [66].

Ongoing research and development efforts aim to enhance receiver tube performance. Advancements include novel materials with higher thermal efficiency, improved coatings that further optimize sunlight absorption, and innovative designs that mitigate heat losses, ultimately striving for increased energy output and cost-effectiveness in solar thermal power generation.

1.2.3 Support and Tracking Systems

Efficient solar field performance relies on stable support structures and precise tracking mechanisms to orient the parabolic troughs perpendicular to incoming sunlight. Advanced tracking systems, often employing motorized drives and sensors, ensure optimal alignment throughout the day to maximize energy capture [70].

Support structures in parabolic trough solar fields are engineered for stability and precision. They are crafted from durable materials like steel or aluminum, designed to withstand environmental forces and maintain precise alignment of the reflective troughs. Factors such as foundation design, elevation adjustments, and accessibility for maintenance are crucial considerations. Foundations must ensure stability in various soil types and conditions, while elevation adjustments optimize solar incidence angles. Maintenance access points and safety features are integrated into the design for efficient upkeep without disrupting operations [70].

Solar tracking systems are pivotal for maximizing energy capture. Single-axis and dual-axis tracking mechanisms continuously orient the troughs perpendicular to incoming sunlight. Single-axis tracking follows the sun's daily east-west path, while dual-axis systems account for seasonal variations, optimizing angles for higher efficiency. Control systems driven by sensors and automation algorithms ensure precise tracking, minimizing errors and maximizing energy yield. Ongoing research aims to improve tracking accuracy, reduce maintenance needs, and explore innovative materials and control mechanisms for even greater efficiency [70].

1.2.4 Design Considerations

In the intricate landscape of parabolic trough collectors, the design considerations encompass a multifaceted approach that intertwines geometry, network systems of receiver pipes, and the impact of operating and environmental conditions.

Geometry stands as the foundational cornerstone dictating the efficacy of parabolic trough collectors. The precise curvature and dimensions of these troughs determine their ability to concentrate sunlight onto the receiver pipes effectively. The optimal shape and alignment play a crucial role in capturing and focusing solar radiation onto the receiver pipes. Designers meticulously calculate the parabolic shape and dimensions to ensure maximum solar energy absorption while considering factors like material durability and manufacturability.

Within the collector system, the network of receiver pipes orchestrates the conversion of sunlight into thermal energy. These pipes, often made of high-grade materials capable of withstanding high temperatures, carry a heat-transfer fluid. The intricate network layout, including the arrangement of these pipes and the flow of the heat-transfer fluid, is meticulously designed to efficiently capture and transfer heat. Optimization of this network system involves considerations of fluid dynamics, heat transfer rates, and pressure drops to ensure uniform heating and maximum energy extraction from the solar radiation.

Operating conditions significantly influence the efficiency and longevity of parabolic trough collectors. Factors such as the operating temperature range, fluid flow rates, and maintenance schedules are meticulously factored into the design. Engineers aim to strike a balance between achieving high operating temperatures for efficient energy conversion and ensuring the longevity of components by avoiding thermal degradation and material fatigue. The design must also accommodate variations in solar irradiance levels throughout the day and across different seasons, maintaining optimal performance under varying conditions.

Environmental considerations also play a pivotal role in the design of parabolic trough collectors. With exposure to harsh weather elements, wind loads, temperature fluctuations, and potential dust or debris accumulation, robust design features become imperative. Durability against environmental stressors is a critical aspect, necessitating weather-resistant materials, sturdy support structures, and efficient cleaning mechanisms to maintain optimal performance over the collector's lifespan.

In essence, the design considerations of parabolic trough collectors intricately weave together geometry optimization, intricate network systems of receiver pipes, and the profound influence of operating and environmental conditions. Balancing efficiency, durability, and adaptability to varying environmental and operational contexts remains at the forefront of engineering endeavors, driving advancements toward more efficient and sustainable solar energy technologies.

1.3 Heat Transfer and Thermal Energy

HTFs play a very significant role in parabolic trough systems. HTF acts as a medium for transporting heat that is collected by the solar collectors to the actual water that is required to be heated up in order to generate steam [63]. The selection

of an HTF depends on several factors, which include thermodynamic and heat transfer properties of HTF. For the successful operation of such solar power plants, careful selection of the working fluid is essential as it is a critical aspect influencing its efficiency. The selected fluid must have most of the desirable properties from the viewpoint of thermodynamics and heat transfer [71]. Traditional thermal fluids have been extensively used, but recent studies explore the use of innovative HTFs like molten salt and nanofluids to enhance heat transfer efficiency [21, 38]. However, there is a need for further research, especially considering network systems and the application of nanofluids in parabolic trough power plants.

1.3.1 Thermal Oil

Thermal oil is an exceptional ultra-high temperature synthetic heat transfer fluid designed to excel in demanding vapor phase systems or liquid phase systems [61, 63, 70]. Its superior thermal stability and remarkably low viscosity ensure efficient and dependable performance across a broad operating range from 12°C to 400°C. Therminol VP-1, one of the most know synthetic oil, boasts the highest thermal stability, making it an optimal choice for applications requiring consistent and reliable heat transfer. With its eutectic mixture of diphenyl oxide (DPO) and biphenyl, it can be utilized both as a liquid heat transfer fluid and as a boiling-condensing heat transfer medium, showcasing versatility and adaptability. Furthermore, its precise temperature control capabilities make it ideal for systems necessitating accurate thermal management, reinforcing its role as a top-tier heat transfer fluid [72].

Properties of Thermal Oil

Key properties of these oils include [63]:

- *High Thermal Stability:* Thermal oils possess high thermal stability to endure the extreme temperatures encountered within the parabolic trough system without significant degradation.
- *Optimal Heat Transfer:* Their formulation enables efficient heat transfer, ensuring maximum utilization of solar energy captured by the troughs.
- *Low Viscosity:* This property aids in the smooth circulation of the fluid within the system, reducing energy losses due to friction.

- *Chemical Stability:* They exhibit chemical inertness to prevent reactions that could deteriorate the fluid's quality over time.

Utilization of Thermal Oil in Parabolic Trough Power Plants

Parabolic trough power plants are a type of solar thermal energy system that utilizes concentrated sunlight to generate electricity using thermal oil as in the following context [63]:

- *Absorption of Solar Energy:* The parabolic troughs concentrate sunlight onto a receiver tube located at the focal line. Within this tube, the thermal oil circulates, absorbing the concentrated solar energy.
- *Heat Transfer:* As the thermal oil absorbs heat, it reaches high temperatures while maintaining its liquid state. This heated fluid is then circulated through a heat exchanger where it transfers its thermal energy to water or another fluid, generating steam.
- *Electricity Generation:* The generated steam drives a turbine connected to a generator, producing electricity. Meanwhile, the now-cooled thermal oil is recirculated back to the troughs to absorb more solar energy, continuing the cycle.

Advantages and Challenges

The advantages of using thermal oil in PTPPs include [73]:

- *Efficiency:* Thermal oil enhances the efficiency of the energy conversion process, facilitating the capture and utilization of solar energy effectively.
- *Storage Capability:* It allows for the storage of thermal energy, enabling power generation even during periods of limited sunlight.
- *Reliability:* Properly managed thermal oil systems exhibit reliability, contributing to the consistent operation of parabolic trough power plants.

While the challenges of using thermal oil in PTPPs include [64]:

- *Degradation:* Over time, thermal oil can undergo degradation due to prolonged exposure to high temperatures and other operating conditions, necessitating periodic maintenance or replacement.
- *Cost Considerations:* The selection and maintenance of thermal oil systems can contribute to the overall cost of constructing and operating parabolic trough power plants.

In conclusion, thermal oil serves as a crucial medium in parabolic trough power plants, facilitating the efficient conversion of solar energy into electricity. Its properties and proper management are essential for maximizing the performance and longevity of these solar thermal systems.

1.3.2 Nanofluids

Nanofluids have attracted the interest of numerous researchers from a wide range of disciplines owing to their intriguing thermal behavior and different applications in heat transfer systems. Numerous studies have been conducted over the last several decades to determine the thermophysical characteristics of nanofluids to find their applicability in heat transfer systems. Consequently, nanofluids are used in various heat transfer applications due to their improved thermal and physical characteristics compared to normal fluids [74]. Nanofluids are the results of nanoparticles dispersion into base fluid which results in an enhancement in its thermal properties. These properties are influenced by the volume fraction of the nanoparticles and their typology. Generally, this volume fraction does not exceed 5% [38]. The solid nanomaterials thermal properties, including specific heat, thermal conductivity and density, are presented in Table 1.1. This thesis focuses on three distinct types: titanium oxide (TiO_2), alumina (Al_2O_3) and copper oxide (CuO).

Composition and Properties of Nanofluids with Thermal Oil Base

Key aspects of these nanofluids include [63]:

- *Enhanced Thermal Conductivity:* Nanoparticles dispersed in the thermal oil significantly increase its thermal conductivity, improving heat transfer efficiency.

TABLE 1.1: Thermal properties of the solid nanoparticles [4, 38].

Nanoparticle	Specific heat (J/(kg K))	thermal conductivity (W/(m K))	Density (kg/m^3)
Titanium Oxide (TiO_2)	692	8.4	4230
Alumina (Al_2O_3)	773	40	3960
Copper Oxide (CuO)	551	33	6000

- *Stability and Dispersion:* Properly engineered nanofluids exhibit stable dispersion of nanoparticles, avoiding sedimentation or agglomeration issues.
- *Viscosity and Flow Characteristics:* Nanofluids may experience changes in viscosity due to nanoparticle addition, impacting flow characteristics within the system.
- *Thermal Stability:* Maintaining thermal stability is crucial to ensure the prolonged performance of nanofluids in high-temperature environments.

Utilization in Parabolic Trough Power Plants

The integration of nanofluids with thermal oil in parabolic trough power plants offers potential advantages [63, 64]:

- *Enhanced Heat Absorption:* Nanofluids with improved thermal conductivity enhance the absorption of concentrated solar energy within the troughs.
- *Improved Heat Transfer Efficiency:* Higher thermal conductivity allows for more efficient heat transfer from the receiver to the working fluid, enhancing overall system efficiency.
- *Reduced Fluid Volume:* Enhanced thermal properties of nanofluids might enable the use of smaller volumes of fluid for the same heat transfer, potentially reducing system size and cost.

Advantages and Challenges

The advantages of using nanofluids when compared to thermal oil include [63, 64]:

- *Increased Thermal Conductivity:* Nanofluids exhibit significantly higher thermal conductivity compared to traditional thermal oils, leading to improved heat transfer efficiency.
- *Enhanced Heat Absorption:* The use of nanofluids can potentially increase the amount of solar energy captured due to their superior heat absorption capabilities.
- *Potential for Size Reduction:* Higher heat transfer efficiency might enable the design of more compact systems due to reduced fluid volume requirements.

While the challenges and considerations when using Nanofluids in PTPPs include [64]:

- *Cost and Nanoparticle Dispersion:* Nanoparticle synthesis and dispersion within the fluid can add to production costs and require careful engineering to maintain stability.
- *Viscosity Changes:* Alterations in viscosity might impact pump performance and system dynamics, necessitating adjustments in system design.

In conclusion, Nanofluids with thermal oil as the base fluid present an innovative approach to enhance the efficiency of parabolic trough power plants. Their improved thermal properties offer potential benefits in heat transfer and energy capture, although challenges such as cost and system adjustments should be carefully considered.

1.3.3 molten salt

molten salt is a type of liquid used as a heat transfer fluid in some parabolic trough power plants. In a parabolic trough power plant, molten salt has several advantages over other heat transfer fluids due to the high specific heat capacity and the high boiling point. During periods of high solar radiation, the molten salt is heated to a high temperature by the concentrated sunlight, and then stored in insulated tanks. When electricity is required, the molten salt is circulated through a heat exchanger, generating steam that drives a turbine to produce electricity. The use of molten salt allows parabolic trough power plants to produce electricity continuously, even during periods of low sunlight or at night, making them a reliable source of renewable energy [21].

Properties and Composition of molten salt

molten salt used in solar thermal applications typically consists of a mixture of alkali nitrate salts, such as a combination of sodium nitrate and potassium nitrate. Key properties include [63, 64]:

- *High Heat Capacity:* molten salts possess high specific heat capacities, allowing them to store substantial amounts of thermal energy per unit volume or mass.
- *Thermal Stability:* They exhibit excellent thermal stability, capable of withstanding high temperatures encountered in CSP systems without significant degradation.
- *Low Vapor Pressure:* molten salts operate at relatively low vapor pressures, reducing the risk of pressurization-related issues in the system.

Utilization in Parabolic Trough Power Plants

molten salt is employed in parabolic trough power plants primarily for two purposes [63, 64]:

- *Heat Transfer:* In the primary loop, molten salt absorbs thermal energy from the solar collectors, reaching high temperatures. This hot salt is then circulated to a heat exchanger, transferring its heat to a secondary fluid, typically water or steam, for electricity generation.
- *Thermal Storage:* molten salt's high heat capacity enables it to store excess thermal energy during periods of high solar insolation. This stored energy can be tapped during periods of reduced sunlight, ensuring continuous power generation.

Advantages and Challenges

The advantages of using molten salt when compared to nanofluids and thermal oil include [63, 64]:

- *High Heat Capacity:* molten salt exhibits superior heat storage capacity compared to thermal oil and nanofluids, allowing for extended thermal energy storage.

- *Thermal Stability:* Its exceptional thermal stability enables operation at higher temperatures without significant degradation, surpassing the limitations of thermal oil and nanofluids.
- *Longer Storage Duration:* molten salt's ability to store thermal energy for extended periods provides greater flexibility in power generation scheduling compared to other fluids.

While the challenges and considerations when using molten salt in PTPPs include [63, 64]:

- *Operational Temperature Limits:* While capable of operating at higher temperatures, system components must be designed to withstand the corrosive nature of molten salts at elevated temperatures.
- *Complexity and Cost:* Implementing and maintaining molten salt systems can be more complex and costly due to specialized materials and safety considerations.

In conclusion, molten salt stands out as an efficient heat transfer and storage medium in parabolic trough power plants, offering superior heat storage capabilities and thermal stability. However, its implementation requires careful consideration of system design, materials, and operational costs.

1.4 Solar Energy in Morocco

Morocco's energy landscape has undergone a transformative shift, driven by a concerted effort to harness its abundant renewable resources, notably solar energy. The nation's heavy reliance on imported gas and oil had long posed economic challenges, prompting a strategic pivot towards renewable energy. With a diverse range of renewable resources including hydroelectric, wind, and particularly promising solar power, Morocco is charting a new course towards sustainability and energy independence [7, 8, 16, 17].

Solar energy emerges as the beacon of promise within Morocco's renewable energy portfolio. The country's geographic advantage, characterized by high solar radiation levels and expansive desert regions, positions solar energy as a pivotal solution [7, 16]. At the forefront of this green revolution stands the Moroccan

Agency for Sustainable Energy (MASEN), a pioneering force in the development of solar energy [15]. Estimates by the Agency suggest Morocco possesses the potential to generate a staggering 5,000 MW of solar energy annually – a capacity capable of meeting the nation's entire electricity demand. The Noor complex stands as a testament to Morocco's ambition and progress in the solar energy domain.

However, despite commendable strides, challenges persist. Expansion of renewable energy capacity demands substantial infrastructure investments, regulatory reforms, and innovative storage solutions to stabilize the grid. Cost considerations also loom large, hindering widespread adoption of renewable technologies within Morocco's energy sector [8, 17].

This immense solar potential, with an average solar radiation of 6 to 7 kWh/m^2 per day and around 85% of the nation's terrain covered by desert, has spurred significant governmental investments in solar energy projects. The inception of the National Solar Plan in 2009 signaled Morocco's commitment to increasing solar energy's contribution to its electricity mix. Ambitious targets were set, aiming for a 14% share of solar energy by 2020 and a monumental leap to 52% by 2030 [15].

1.4.1 Overview of NOOR Solar Power Complex

The NOOR Solar Power Complex represents a groundbreaking initiative in Morocco's pursuit of renewable energy dominance. Nestled in the scenic expanse of Ouarzazate, this complex stands as a testament to Morocco's ambitious strides toward harnessing solar energy on a monumental scale [7, 8, 16, 17].

Comprising multiple phases of development, the NOOR Solar Power Complex is a flagship project under the National Solar Plan, an initiative aimed at significantly increasing the share of renewable energy in Morocco's power mix. Notably, NOOR is a concentrated solar power (CSP) plant, distinguished by its innovative use of mirrors to concentrate sunlight and generate heat, subsequently converted into electricity [16].

The complex's significance is underscored by its colossal scale, with various phases adding substantial capacities to the nation's renewable energy grid. The first phase, NOOR I, began operations in 2016, featuring a combination of parabolic troughs and a molten salt storage system. NOOR II and III followed suit, further amplifying the complex's capacity. The fourth phase, NOOR IV, has also been envisioned to bolster the complex's energy output [10].

One of NOOR's standout features is its ability to store thermal energy, a vital aspect in sustaining power generation beyond daylight hours. The molten salt storage system enables the plant to continue producing electricity even during periods of reduced or no sunlight, ensuring a more consistent and reliable energy supply [8, 16, 17].

Moreover, NOOR's strategic location in Ouarzazate, a region characterized by ample sunshine and favorable climatic conditions, optimizes its efficiency and output. This location, coupled with Morocco's ambitious renewable energy targets, positions the NOOR Solar Power Complex as a beacon of progress within the nation's energy transition [7, 16].

Beyond its technical prowess, NOOR serves as a symbol of Morocco's commitment to renewable energy on the global stage. Its successful implementation and operation showcase the nation's capacity for innovation and its dedication to reducing dependence on fossil fuels while combating climate change.

In essence, the NOOR Solar Power Complex epitomizes Morocco's vision of a sustainable future powered by renewable energy. As a flagship project underpinning the country's National Solar Plan, NOOR stands tall as a testament to innovation, technological advancement, and a bold stride towards a cleaner, more sustainable energy landscape.

1.4.2 NOOR I Power Plant

The NOOR I Solar Power Plant stands as a groundbreaking endeavor in Morocco's renewable energy landscape, engineered to harness solar energy on a colossal scale [16]. With a capacity of 160 MW, this power plant spans an expansive 450 hectares, representing a pivotal investment of 176 million euros. Operational since February 4th, 2016, its construction initiated on May 10th, 2013, marking a transformative leap in the nation's energy trajectory [15].

Background and Design

Operated by Nomac and engineered by Sener, TSK, and Acciona, NOOR I's strategic design encompasses a sophisticated storage capacity of 3 hours, a crucial feature enabling its operation during periods of low solar radiation or at night. The electricity generated by this facility is supplied to the National Office of Electricity

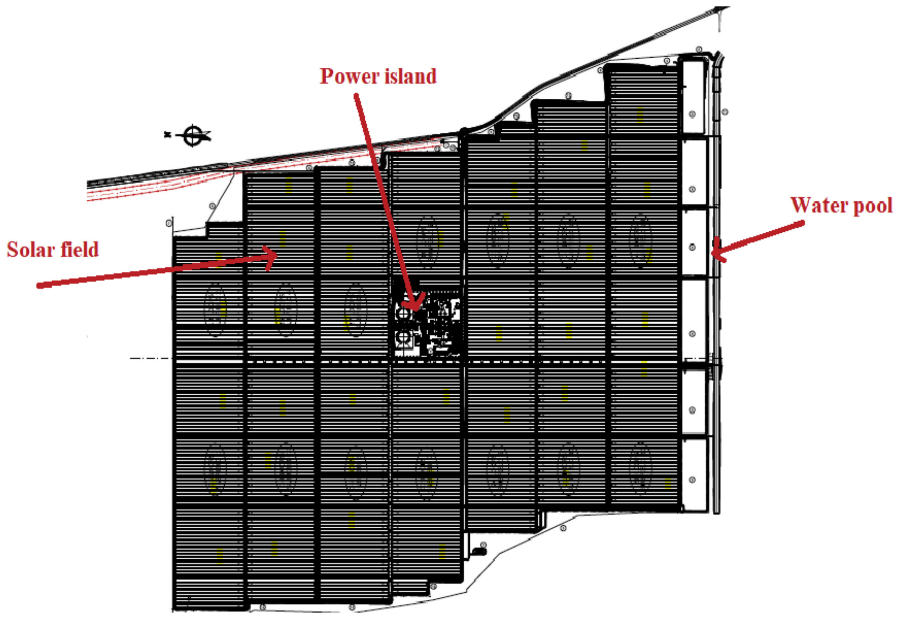

FIG. 1.4: The global architecture of the power plant Noor I [16].

at a rate of 16.2 cents per kilowatt-hour, making strides towards sustainable energy generation at competitive pricing [16].

The architectural layout of NOOR I is meticulously crafted to optimize solar field operations during daylight and seamlessly transition to thermal storage utilization during less optimal periods. The power island, constituting a mere 2% of the plant's total surface, hosts an intricate network of components. This includes two molten salt tanks, a water cooling tower, a circuit for heat transfer fluid (HTF), steam generation units, turbines, and facilities for water treatment and weather monitoring [16].

The power island's heart lies in the process of converting solar energy into electricity. The HTF pumps propel the fluid through the solar field, where it undergoes heating via interaction with the sun's rays, achieving temperatures up to 393°C. The heated HTF, stored in molten salt tanks, facilitates electricity generation through heat exchange during low-solar periods [16].

The solar field itself boasts an impressive infrastructure, consisting of 400 loops, each managed by hydraulic drives for precise HTF flow management. With 336 parabolic mirrors per field and more than 500,000 mirrors in total, the system

incorporates trackers and temperature sensors for each collector to optimize solar energy absorption while ensuring HTF temperature remains below 400°C [16].

Maintenance is integral to sustaining optimal performance. The mirrors undergo regular cleaning using a fleet of specialized trucks equipped with brushes and high-pressure cleaners. These tools effectively cleanse the mirrors, with high-pressure cleaners utilized to minimize degradation and ensure mirror quality [8].

HTF

The heart of Noor I's efficient energy transfer lies in its use of a specialized Heat Transfer Fluid (HTF), synthetic oil, meticulously chosen for its exceptional properties that optimize the solar power plant's functionality [16].

This synthetic oil stands out for its unique characteristics, enabling operations at pressures lower than those required for steam-based systems. Notably, it outperforms mineral oil counterparts by efficiently transferring heat while exhibiting remarkable thermal stability. Its superior performance extends to a longer lifespan, a crucial factor in sustaining the plant's operations over time .

Operating within specific temperature and pressure ranges, this HTF is designed to evaporate at a substantial 420°C and 10.5 bar while maintaining a freeze point of 12°C. These attributes ensure operational reliability within the demanding thermal conditions of the solar field [63].

Once heated to a remarkable temperature of 393°C within the solar field, the HTF embarks on a pivotal journey. Guided by elementary pumps, it traverses through a divided third pipe, bifurcating its path toward two essential systems within the plant.

The first part of this journey directs the HTF toward the storage system, a critical element allowing the plant to preserve excess heat for subsequent power generation. Simultaneously, the other path leads the HTF to the steam generation system, initiating a fundamental heat exchange process between the HTF and water, a catalyst for electricity production [16]. The HTF is then circulated back into the solar loop, it recommences its journey, seeking reheating within the solar field to perpetuate the cycle of energy conversion.

In summary, the selection of synthetic oil as the HTF in Noor I exemplifies a deliberate choice, driven by its exceptional thermal characteristics and longevity. Its role in facilitating efficient heat transfer and enabling the cyclic energy

conversion process underscores its significance within the solar power plant's operational framework.

Heat Storage

The cornerstone of energy sustainability at the NOOR I solar power plant lies in its innovative heat storage system, harnessing the prowess of molten salt to store and regulate thermal energy derived from the sun-drenched solar field [16].

The primary function of this ingenious heat storage mechanism is to efficiently capture and retain thermal energy garnered from the expansive solar field. The chosen medium for this task is molten salt, a carefully formulated composition predominantly comprised of sodium and potassium nitrates. These molten salt compositions exhibit exceptional thermal properties, making them ideal candidates for energy storage [16].

Within the NOOR I solar power plant, this thermal energy storage is facilitated through two substantial tanks dedicated to the containment of molten salt. During the charging phase, the cold tank brims with molten salt while its counterpart, the hot tank, remains devoid of the energy-storing liquid [16].

To orchestrate the energy transfer process, a sophisticated system of pumps comes into play, orchestrating the circulation of molten salt from the brimming cold tank towards the empty hot tank. This circulation journey involves traversing through a series of three exchangers strategically positioned along the route. These exchangers serve a crucial role in facilitating the transfer of heat between the molten salt and the hot Heat Transfer Fluid (HTF) emanating from the solar field [16].

As the sun sets or clouds shroud the solar panels, the dynamics of energy utilization shift. Cold HTF, now devoid of direct solar heat, is channeled through the same three exchangers. Here, a transformative exchange occurs, as the cold HTF interacts with the stored molten salt, facilitating the transfer of stored thermal energy back to the HTF. Once the HTF is suitably heated through this exchange, it proceeds onward to the Steam Generation System (SGS), where it fuels the generation of electricity, thus maintaining a consistent and reliable energy output even during periods of reduced sunlight [8, 16].

The integration of this sophisticated heat storage system within NOOR I not only ensures a continuous supply of electricity but also enables the plant to adapt and thrive during adverse weather conditions or reduced solar exposure. By

effectively harnessing and redistributing solar-derived thermal energy through the molten salt storage system, NOOR I stands as a beacon of technological innovation and sustainable energy utilization within Morocco's renewable energy landscape [8, 16].

Comparison with other power plants

The NOOR Solar Power Complex, particularly its first phase, NOOR I, stands as a remarkable feat within the global landscape of Concentrating Solar Power (CSP) technology. This comparison aims to shed light on NOOR I's unique characteristics in comparison to other similar power plants worldwide.

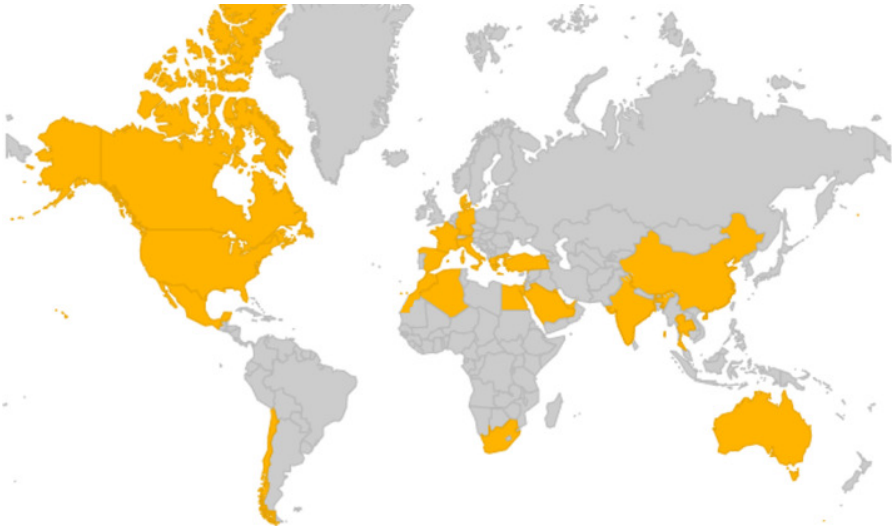

FIG. 1.5: The map of concentrating solar power projects in the world [16].

Within the realm of Parabolic Trough Solar Thermal Power Plants (PTSTPPs), around 98 installations operate across various nations globally. Predominantly situated in the United States and Spain, these plants contribute significantly to the global renewable energy matrix. Among these, Spain hosts approximately 42.85% of PTSTPPs, followed by the USA with 17.34%, showcasing their significant investments in this technology. However, Morocco emerges as a player, hosting 4.08% of these installations, notably represented by the NOOR Solar Power Complex [16].

The NOOR I power plant distinguishes itself notably from other global installations. With a capacity of 160 MW, it stands three times larger than the average capacity of PTSTPPs globally, which hovers around 55.21 MW. Moreover, NOOR I's storage capacity of 3 hours, while lower than the global average of 6.9 hours, represents a notable aspect considering its contribution to Morocco's renewable energy goals [16].

A striking feature of NOOR I is its high specific annual generation, reaching 3250 MWh/MW. This metric surpasses the global average of 2564.85 MWh/MW by approximately 21.08%. Remarkably, 61.5% of PTSTPPs globally exhibit a lower specific annual generation compared to NOOR I, showcasing its efficiency and productivity in electricity generation [16].

In terms of the plant's surface area, NOOR I spans 4800000 m2, significantly surpassing the average surface area of PTSTPPs worldwide, which stands at 1618285.5 m2. This colossal surface area reinforces NOOR I's status as one of the largest PTSTPPs globally, trailing behind only two plants situated in the USA [16].

While NOOR I exhibits impressive capacities and efficiency metrics, it's also essential to consider the cost variations associated with PTSTPPs worldwide. Costs fluctuate between 1542.85 €/MWh-year and 5278.2 €/MWh-year, showcasing the diverse economic landscapes shaping these power plants' implementation and operational dynamics [16].

In summary, NOOR I's distinguishing features, including its exceptional capacity, high specific annual generation, and substantial surface area, position it as a leading player within the global PTSTPP landscape. Despite variations in storage capacity and size compared to some international installations, NOOR I's remarkable performance underscores its pivotal role in Morocco's renewable energy journey.

Geometric and Thermal Parameters

Detailed information about the geometric and thermal parameters from NOOR I solar PTPP are listed in Table 1.2. For the simulation and optimization of PTPPs, the presented data will be used in the models introduced in the next chapter of this thesis.

Parameter	Unit	Value
Inner diameter $\tilde{D_i}$	m	0.066
Outer diameter $\tilde{D_o}$	m	0.07
Collector width W_a	m	5.76
Intercept factor γ	–	0.867
Absorbance of glass cover α_g	–	0.94
Specular reflectance r_m	–	0.94
Incident angle modifier k_θ	–	1
Emittance of the cover ϵ	–	0.15
Stefan-Boltzmann constant $\tilde{\sigma}$	$W \cdot m^{-2} \cdot K^{-4}$	$5.67 \cdot 10^{-8}$
Absorber roughness e	–	10^{-6}
Efficiency of the pump η_p	–	0.9
Wind velocity u_a	$m \cdot s^{-1}$	3.7
Air density ρ_a	$kg \cdot m^{-3}$	1.293
Air thermal conductivity k_a	$W \cdot m^{-1} \cdot K^{-1}$	0.024
Air viscosity μ_a	$kg \cdot m^{-1} \cdot s^{-1}$	$1.81 \cdot 10^{-5}$

TABLE 1.2: Geometric and thermal parameters from NOOR I [1, 3].

1.4.3 Climatic Conditions in Ouarzazate, Morocco

The climatic conditions in Ouarzazate, Morocco, unveil a landscape abundant in solar resources and characterized by favorable environmental parameters conducive to solar energy harnessing and sustainable development.

Derived from the METEONORM weather database, a typical sunny day in Ouarzazate unveils key meteorological facets pivotal for solar energy generation. The hourly variation of solar radiation and ambient temperature, graphically depicted in Figure 1.6, unveils a compelling narrative of this region's climatic attributes.

Throughout the day, from sunrise to sunset, the plotted data illustrates a pronounced peak in solar radiation, soaring to approximately 1000 W/m^2. This robust solar irradiance signifies the ample sunshine Ouarzazate receives, marking it as an ideal locale for solar energy harnessing. This abundance of sunlight presents an unparalleled opportunity for efficient solar power generation and reinforces the region's prominence as a hub for solar energy projects.

Simultaneously, the ambient temperature depicts a notable peak, reaching

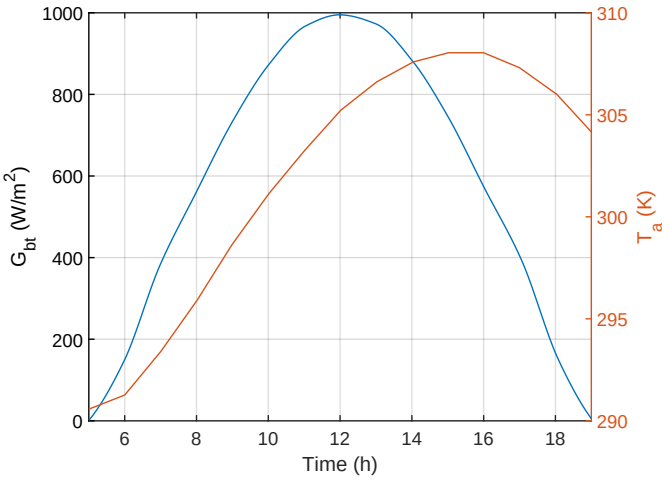

FIG. 1.6: Hourly variation of solar radiation (left axis) and ambient temperature (right axis) in the region of Ouarzazate [1, 38].

around 308 K. This temperature profile, showcasing a favorable climatic range, signifies the region's suitability for solar energy infrastructure. The temperate climate, characterized by warm daytime temperatures, ensures optimal conditions for the efficient operation of solar technologies.

This combination of high solar radiation levels and moderate ambient temperatures positions Ouarzazate as an ideal location for solar energy ventures. The climatic data underscores the region's potential to facilitate sustainable energy initiatives and reinforces Morocco's strategic pursuit of renewable energy dominance.

In essence, Ouarzazate's climatic conditions, typified by ample sunlight and favorable ambient temperatures, offer a compelling canvas for the proliferation of solar energy projects. This region's unique meteorological characteristics serve as a cornerstone in the realization of Morocco's ambitious renewable energy goals, fostering a landscape ripe for sustainable and clean energy development.

1.5 Modeling, Simulation and Optimization

Modeling and simulating parabolic trough systems are foundational in advancing solar thermal technology. These processes, rooted in engineering and computational analysis, offer critical insights into system performance, aiding design enhancements and operational efficiency [75].

Modeling involves crafting mathematical representations of the physical and operational facets of parabolic trough systems. Understanding components like reflective troughs, receiver tubes, heat transfer fluids, and control mechanisms is essential. Optical modeling simulates solar radiation reflection, concentration, and absorption, crucial for heat generation. Accurately predicting sunlight angles on troughs helps optimize energy capture. Thermal modeling assesses heat transfer within receiver tubes and fluids, considering flow rates, temperature differentials, and material properties. It also accounts for thermal storage systems' efficacy in heat storage and release for continuous power generation. Simulation replicates real-world system behavior under varying conditions. Dynamic simulations gauge system responses under changing environments, providing insights into transient behaviors and operational traits. Predicting energy output based on sunlight availability and system efficiency aids in performance assessment. Optimization efforts identify key parameters affecting system performance, guiding design and operational improvements. Algorithms exploring control mechanisms maximize energy capture by optimizing sun-tracking and fluid flow rates.

In addition, optimization can be involved to boost system performance and cost-effectiveness through iterative enhancements based on modeling and simulation outcomes. Refining trough geometry and material selection improves light concentration and heat absorption. Optimizing receiver tube design enhances heat transfer efficiency and reduces losses. Advanced control algorithms informed by simulations optimize sun-tracking and fluid flow rates. Proactive maintenance schedules, informed by simulation analyses, minimize downtime and enhance long-term performance [75].

For a deeper and profound understanding of the possibilities and limitations of parabolic trough systems, accurate models must be made available. In this thesis, the complete power plant is described by including the main components, such as the thermo-fluid dynamics in the tube network and the pumps serving as driving forces for the fluid. This is achieved through a set of PDEs that describe the thermo-fluid dynamics in a network of tubes. However, to render such an approach

feasible, a series of simplifications are necessary. Firstly, the equations are reduced to a one-dimensional (spatial and longitudinal) system on the tube network by appropriately accounting for the relevant effects from the omitted cross-sectional dimensions. Subsequently, an asymptotic analysis is applied with respect to certain small parameters to further diminish the system. Ultimately, a set of nonlinear coupled first-order PDEs is obtained on each tube, supplemented with a set of physically meaningful conditions at the nodes of the network. This model enables fast and robust simulations, facilitating optimization approaches. Optimization can be conducted on various input data, such as applied pressures or inflow temperature, as well as on various system parameters, including network structure, tube dimensions, and properties of the thermo-fluid in use. Consequently, this model finds application in both the planning and operational phases of a parabolic trough power station. Additionally, it serves as a strong foundation for modeling increasingly important, more complex hybrid power plants.

In conclusion, modeling, simulating, and optimizing parabolic trough systems are instrumental in driving solar thermal technology forward. By offering insights into system behavior, performance, and potential improvements, these methodologies play a crucial role in advancing efficient, reliable, and sustainable solar energy generation.

Chapter 2

Mathematical Modeling and Numerical Simulation of Solar Field

2.1 Introduction

This chapter delves into the critical aspects of modeling and simulating a solar field, with a focus on parabolic trough power plants. A comprehensive mathematical model that simulates the heat transfer flow within a network of parabolic trough collectors (PTCs) is covered, employing heat transfer fluids (HTFs) such as thermal oil and molten salt. The discussion begins with the thermal properties of the HTFs and a one-dimensional mathematical model is presented, characterizing the fluid dynamics within the tubes network. Key parameters such as fluid velocity, pressure, temperature, heat capacity, density and others are accounted for by this model. Additionally, the utilization of nanofluids as potential enhancements to the heat transfer process is explored. Real-world data from the NOOR I solar power plant, situated in Ouarzazate, Morocco, is integrated into the model to accurately replicate the behavior of heat transfer in a PTC network system under realistic conditions.

Furthermore, numerical simulation techniques are examined in the chapter, and simulations are presented using the developed mathematical model, showcasing practical applications and insights into the optimization of various system parameters. The significance of this model for both the planning and operational phases of a parabolic trough power station is emphasized, offering a powerful tool for optimizing the power output and providing a starting point for modeling more complex hybrid power plants. The chapter aims to provide a profound

understanding of parabolic trough systems and their potential for efficient, sustainable energy production.

2.2 Heat Transfer Fluid: Thermal Properties

For a complete and more accurate mathematical modeling of PTPP systems, in this section, temperature dependent thermal properties of the different heat transfer fluids are required. Hence, the thermal properties of Therminol VP-1 and molten salt varying with the temperature were extracted from the manufacturer datasheet. Furthermore, in the case of nanofluids, integrating nanoparticles in the base fluid (Therminol VP-1) will induce an enhancement in its thermal properties. These properties are influenced by the volume fraction of the nanoparticles and their typology.

2.2.1 Synthetic Oil : Therminol VP-1

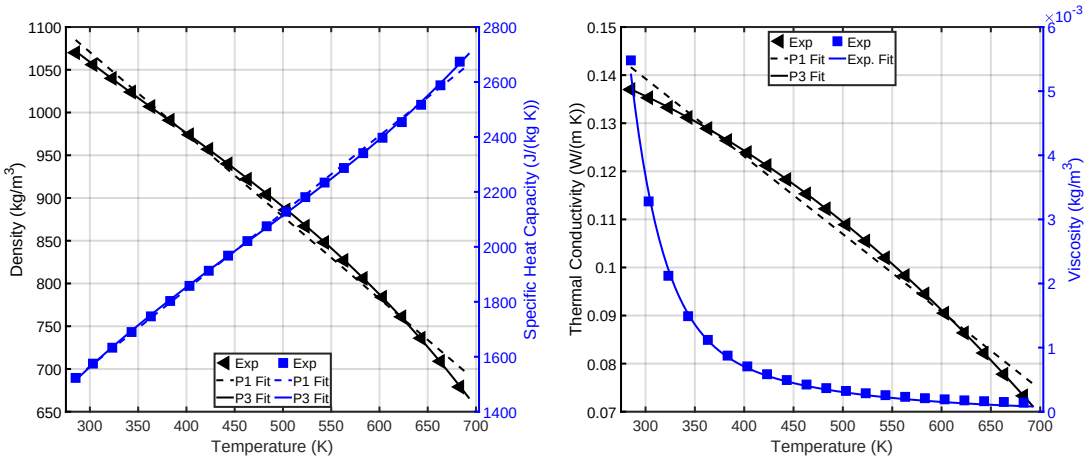

FIG. 2.1: Thermal properties of TerminolVP-1 with their fittings [1].

The constitutive relations for the special oil Terminol VP-1, are only known by measured data (given in [72]). Figure 2.1 displays the thermal properties of Terminol VP-1 and the corresponding fittings within the appropriate temperature range of 285.15 K to 693.15 K. The temperature dependence of the data can be

approximated by polynomials or exponential functions (as in [38]). In Figure 2.1, the dependence of the density, specific heat capacity and thermal conductivity on the temperature is seen to be almost linear, while the dynamic viscosity is fitted in accordance with temperature using exponential equations. The resulting approximate relations of thermal properties reads as follow:

- Density ($\mathrm{kg/m^3}$):

$$\rho \simeq \begin{cases} -0.96T + 1359.18 & (P^1 \text{ Fitting}) \\ -2.20 \cdot 10^{-6}T^3 + 2.48 \cdot 10^{-3}T^2 - 1.75T + 1421.23 & (P^3 \text{ Fitting}) \end{cases} \tag{2.1}$$

- Thermal Conductivity ($\mathrm{W/(m \cdot K)}$):

$$k \simeq \begin{cases} -1.62 \cdot 10^{-4}T + 0.19 & (P^1 \text{ Fitting}) \\ 2.69 \cdot 10^{-12}T^3 - 1.77 \cdot 10^{-7}T^2 + 9.57 \cdot 10^{-6}T + 0.15 & (P^3 \text{ Fitting}) \end{cases} \tag{2.2}$$

- Specific heat capacity ($\mathrm{J/(kg \cdot K)}$):

$$c_p \simeq \begin{cases} 2.80T + 724.65 & (P^1 \text{ Fitting}) \\ 7.70 \cdot 10^{-6}T^3 - 1.07 \cdot 10^{-2}T^2 + 7.56T + 51.27 & (P^3 \text{ Fitting}) \end{cases} \tag{2.3}$$

- Dynamic viscosity ($\mathrm{Pa \cdot s}$):

$$\mu \simeq 29.26e^{-3.12 \cdot 10^{-2}T} + 9.06 \cdot 10^{-3}e^{-6.81 \cdot 10^{-3}T} \text{ (Exponential Fitting)} \tag{2.4}$$

As can be observed, the density and thermal conductivity of Therminol VP-1 demonstrates a linear decline as temperature increases, while the specific heat capacity displays a linear increase with increasing temperature. The dynamic viscosity, on the other hand, presents an exponential trend, whereby it decreases as temperature increases.

2.2.2 Nanofluids

Regarding nanofluids, the suspensions of nanoparticles with a volume fraction (φ) in a base fluid, namely, in our case, Therminol VP-1, is recognized for its ability to

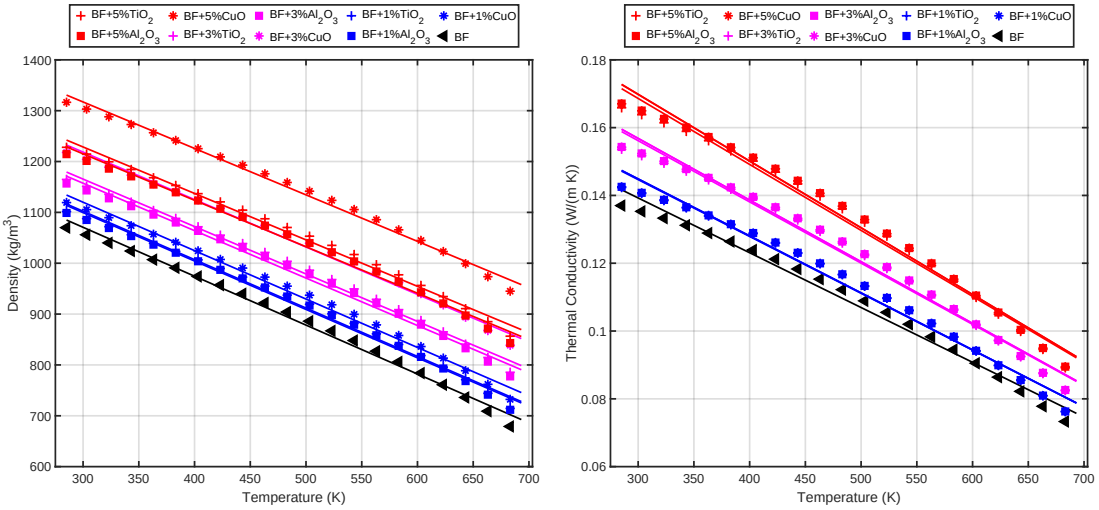

FIG. 2.2: Density and Thermal conductivity of nanofluids with their fittings [2, 3].

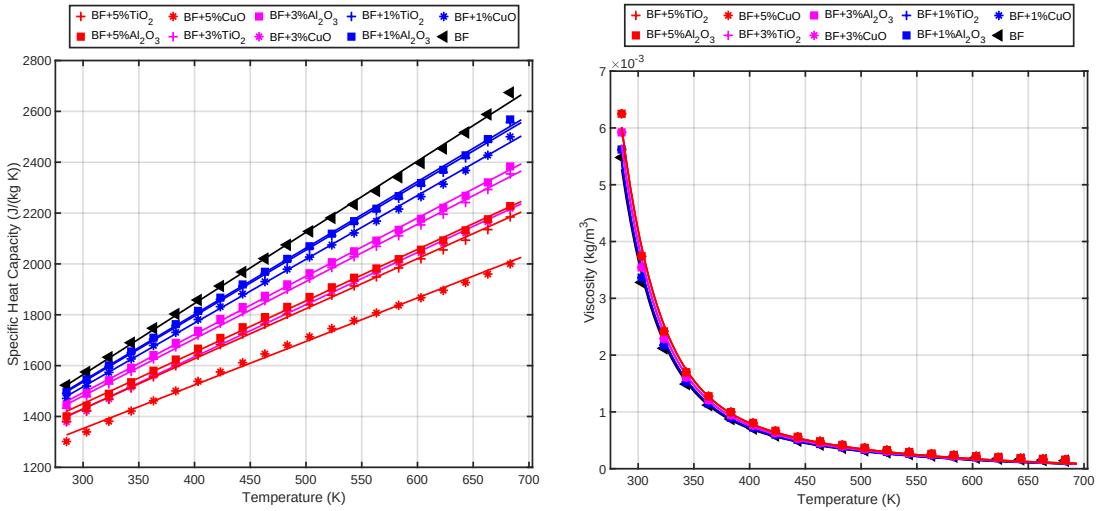

FIG. 2.3: Specific heat capacity and viscosity of nanofluids with their fittings [2, 3].

enhance the thermal properties of the HTF, including dynamic viscosity, specific heat capacity and density [76–78].

The subsequent equations, represented by Eqs. 2.5-2.8, express the thermal characteristics of the nanofluid in terms of φ with the fitting function. Density ρ_{nf}, thermal conductivity k_{nf}, specific heat capacity $c_{p,nf}$ can be fitted using polynomial functions with respect to temperature, whereas the dynamic viscosity μ is fitted exponentially with respect to temperature. The nanofluid is denoted by the subscript (nf), the basefluid by (bf), and the solid nanoparticles by (s). The thermal properties of the solid nanoparticles are given in the previous chapter, see Table 1.1.

- Density ($\mathrm{kg/m^3}$):

$$\rho_{nf} = (1-\varphi)\rho_{bf} + \varphi\rho_s \simeq a_1(\varphi)T + a_2(\varphi) \tag{2.5}$$

- Thermal Conductivity ($\mathrm{W/(m \cdot K)}$):

$$k_{nf} = k_{bf}\frac{k_s + 2k_{bf} - 2\varphi\left(k_{bf} - k_s\right)}{k_s + 2k_{bf} + 2\varphi\left(k_{bf} - k_s\right)} \simeq b_1(\varphi)T + b_2(\varphi) \tag{2.6}$$

- Specific heat capacity ($\mathrm{J/(kg \cdot K)}$):

$$c_{p,nf} = \frac{(1-\varphi)\left(\rho c_p\right)_{bf} + \varphi\left(\rho c_p\right)_s}{\rho_{nf}} \simeq P^n_{c_p}(T,\varphi) \tag{2.7}$$

- Dynamic viscosity ($\mathrm{Pa \cdot s}$):

$$\mu_{nf} = \mu_{bf}\left(1 + 2.5\varphi + 6.25\varphi^2\right) \simeq c_1(\varphi)e^{d_1(\varphi)T} + c_2(\varphi)e^{d_2(\varphi)T} \tag{2.8}$$

Figs. 2.2-2.3 illustrates the properties of various nanofluids and the base fluid within the temperature range of 285.15 K to 693.15 K, alongside the corresponding fittings. The figure clearly demonstrates that nanofluids exhibit greater density and thermal conductivity compared to the base fluid, with values increasing proportionally to the volume fraction. CuO nanoparticles show the highest densities, and almost no difference is observed in the thermal conductivity of nanofluids. In contrast, the specific heat capacity decreases with increasing volume fraction; again, the strongest effect is seen for CuO nanoparticles. The dynamic viscosity shows almost no dependence on the volume fraction of added nanoparticles. Finally, the thermal properties exhibit similar behavior with respect to temperature changes such as that of the base fluid.

2.2.3 molten salt: Dynalene MS-1

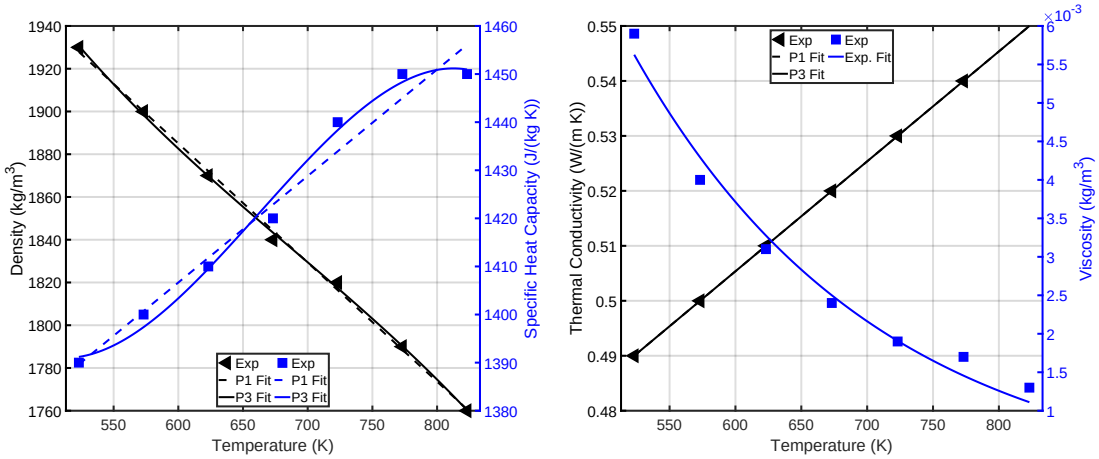

FIG. 2.4: Thermal properties of molten salt with their fittings [4].

In the case of using molten salt (Dynalene MS-1) as HTF, the thermal characteristics, which vary in accordance with temperature, are provided from the fluid data sheet [79]. Subsequently, the thermal attributes of molten salt are represented in Eqs. 2.9-2.12 as functions of temperature, whereby the density, thermal conductivity and the specific heat capacity are fitted using polynomial functions, while the dynamic viscosity is fitted in accordance with temperature using exponential functions.

- Density ($\mathrm{kg/m^3}$):

$$\rho \simeq \begin{cases} -0.56T + 2219.33 & (P^1 \text{ Fitting}) \\ -2.22 \cdot 10^{-6}T^3 + 4.58 \cdot 10^{-3}T^2 - 3.67T + 2913.18 & (P^3 \text{ Fitting}) \end{cases} \tag{2.9}$$

- Thermal Conductivity ($\mathrm{W/(m \cdot K)}$):

$$k \simeq \begin{cases} 2.00 \cdot 10^{-4}T + 0.38 & (P^1 \text{ Fitting}) \\ -4.58 \cdot 10^{-23}T^3 + 9.25 \cdot 10^{-20}T^2 + 2.00 \cdot 10^{-4}T + 0.38 & (P^3 \text{ Fitting}) \end{cases} \tag{2.10}$$

- Specific heat capacity ($\mathrm{J/(kg \cdot K)}$):

$$c_p \simeq \begin{cases} 0.22T + 1273.80 & (P^1 \text{ Fitting}) \\ -4.44 \cdot 10^{-6}T^3 + 8.83 \cdot 10^{-3}T^2 - 5.55T + 2513.80 & (P^3 \text{ Fitting}) \end{cases} \tag{2.11}$$

- Dynamic viscosity ($\mathrm{Pa \cdot s}$):

$$\mu \simeq 9.52 \cdot 10^{-2} e^{-5.41 \cdot 10^{-3} T} \text{ (Exponential Fitting)} \tag{2.12}$$

Figure 2.4 displays the thermal attributes of molten salt and their corresponding fittings within the appropriate temperature range of 523.15 K to 823.15 K. As shown in the figure, the density of molten salt demonstrates a consistent linear decline as temperature increases, while the specific heat capacity displays a linear increase with rising temperature. The dynamic viscosity, on the other hand, presents an exponential trend, whereby it decreases as temperature rises. In contrast to Therminol VP-1, thermal conductivity of molten salt tends to increase when temperature increases.

2.3 Heat Transfer Flow Model

2.3.1 Single Pipe Model

A system of balance laws for the relevant quantities under consideration is introduced in this section, which will be used to model, simulate, and optimize a parabolic trough power plant. Since the power plant is composed of a network of tubes conducting the heated flow, the description of a single pipe in such a network is needed. The functioning of a PTC is illustrated in the schematic diagram shown in Figure 2.5.

Models such as the type used here are widely employed in similar applications where heat transport is deemed crucial. Applications in gas pipelines [80], exhaust pipes [57, 58], tunnel ventilation [55], solar updraft towers [56, 81], and energy towers [82] are referred to in this section. In particular, the application for tubes in solar parabolic troughs is studied in [53, 54].

In the following, a mathematical model for the heat-transfer flow of different types of HTFs in a collector is being introduced. Various fluid quantities, including

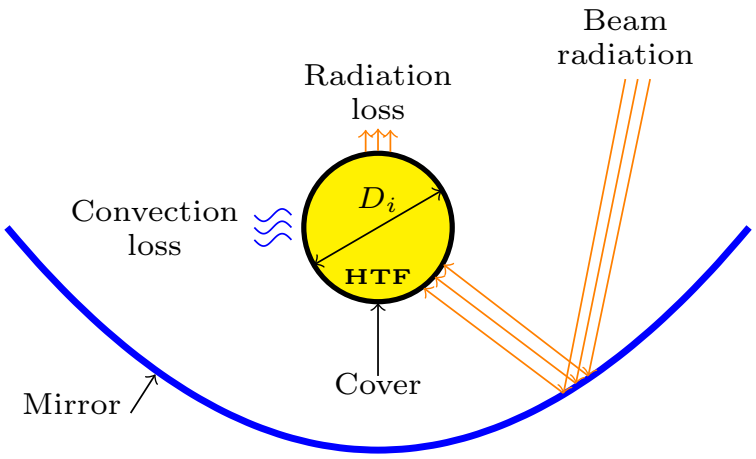

FIG. 2.5: Schematic diagram of parabolic solar collector operation [1].

fluid density, thermal conductivity, specific heat capacity, velocity, temperature, viscosity and pressure, are being described as functions of time and space, while other quantities are obtained such as Reynolds number, friction factor, energetic and exergetic efficiencies.

Unidirectional Flow System

A unidirectional flow model in the $\tilde{x}$-direction within a single solar PTC is derived using conservation laws. For the analysis to be simplified, the model variables and parameters are averaged over the dimensions $\tilde{y}$ and $\tilde{z}$. This averaging approximation is justified by the significant difference in length between the PTC tube and its cross-sectional diameter. Namely, for a given quantity $\tilde{F}$, it is found that:

$$\tilde{A}\tilde{f}(\tilde{x},\tilde{t}) = \iint \tilde{F}(\tilde{x},\tilde{y},\tilde{z},\tilde{t})dydz \tag{2.13}$$

where the $\tilde{\cdot}$ indicates unscaled variables (with physical dimensions). $\tilde{f}$ denotes the cross-sectional averaged quantity. Here, $\tilde{x}$, $\tilde{t}$, and $\tilde{A}$ are the longitudinal space variable (along the tube), the time, and the cross-sectional area of the tube, respectively.

The governing equations are derived from the conservation and balance laws for the mass, momentum and energy, where the unknown variables are the density $\tilde{\rho} = \tilde{\rho}(\tilde{x}, \tilde{t})$, thermal conductivity $\tilde{k} = \tilde{k}(\tilde{x}, \tilde{t})$, specific heat capacity $\tilde{c}_p = \tilde{c}_p(\tilde{x}, \tilde{t})$, the velocity $\tilde{u} = \tilde{u}(\tilde{x}, \tilde{t})$, the temperature $\tilde{T} = \tilde{T}(\tilde{x}, \tilde{t})$, viscosity $\tilde{\mu} = \tilde{\mu}(\tilde{x}, \tilde{t})$ and the pressure $\tilde{p} = \tilde{p}(\tilde{x}, \tilde{t})$, all intended as cross-sectional mean values. Thus, the governing equations are given by, [1, 54]:

i) *Conservation of Mass*

$$(\tilde{A}\tilde{\rho})_{\tilde{t}} + (\tilde{A}\tilde{\rho}\tilde{u})_{\tilde{x}} = 0 \tag{2.14}$$

ii) *Momentum balance*

$$\left(\tilde{A}\tilde{\rho}\tilde{u}\right)_{\tilde{t}} + \left(\tilde{A}(\tilde{\rho}\tilde{u}^2 + \tilde{p})\right)_{\tilde{x}} = -\tilde{U}_i\tilde{\tau}_w + \tilde{A}\,(\tilde{\tau}_{11})_{\tilde{x}} \tag{2.15}$$

iii) *Energy balance*

$$\begin{aligned} &\left\{\tilde{A}\tilde{\rho}(\tilde{h} + \frac{1}{2}\tilde{u}^2)\right\}_{\tilde{t}} + \left\{\tilde{A}\tilde{\rho}\tilde{u}\left(\tilde{h} + \frac{1}{2}\tilde{u}^2\right) + \tilde{A}\tilde{u}\tilde{p}\right\}_{\tilde{x}} \\ &\quad = \tilde{U}_i\tilde{u}\tilde{\tau}_w + \tilde{A}\,(\tilde{u}\tilde{\tau}_{11})_{\tilde{x}} + \tilde{A}\left(\tilde{k}\tilde{T}_{\tilde{x}}\right)_{\tilde{x}} + \tilde{\dot{q}}_s - \tilde{U}_o\tilde{\dot{q}}_{\text{rad}} - \tilde{U}_o\tilde{\dot{q}}_{\text{conv}} \end{aligned} \tag{2.16}$$

where $d\tilde{h} = \tilde{c}_p d\tilde{T}$ is the enthalpy, $\tilde{\tau}_{11} = \tilde{\tau}_{11}(\tilde{x}, \tilde{t})$ is the internal shear stress, $\tilde{\tau}_w = \tilde{\tau}_w(\tilde{x}, \tilde{t})$ the wall friction, $\tilde{\dot{q}}_s = \tilde{\dot{q}}_s(t)$ the beam solar radiation, $\tilde{\dot{q}}_{\text{conv}} = \tilde{\dot{q}}_{\text{conv}}(\tilde{x}, \tilde{t})$ the convective heat loss and $\tilde{\dot{q}}_{\text{rad}} = \tilde{\dot{q}}_{\text{rad}}(\tilde{x}, \tilde{t})$ the radiation heat exchange between the absorber and the atmosphere, $\tilde{U}_i = \tilde{U}_i(\tilde{x}) = \pi\tilde{D}_i(\tilde{x})$ is the inner circumference (diameter) of the tube and $\tilde{U}_o = \tilde{U}_a(\tilde{x}) = \pi\tilde{D}_a(\tilde{x})$ is the absorber circumference (diameter).

The shear stress of the turbulent fluid on the wall is described classically as follows:

$$\tilde{\tau}_w = \frac{\xi}{8}\tilde{\rho}\tilde{u}|\tilde{u}| \tag{2.17}$$

where ξ denotes the coefficient of friction calculated according to the Colebrook equation [83] as follows:

$$\frac{1}{\sqrt{\xi}} = -0.86\ln\left(\frac{e}{3.7\tilde{D}_i} + \frac{2.51}{Re\sqrt{\xi}}\right) \tag{2.18}$$

with e is the absorber roughness and the fluid Reynolds number Re is expressed as:

$$Re = \frac{\tilde{\rho}\tilde{u}\tilde{D}_{in}}{\tilde{\mu}}. \tag{2.19}$$

For the unidirectional flow of a Newtonian fluid the shear stress $\tilde{\tau}_{11}$ is given as follows [54]:

$$\tilde{\tau}_{11} = \frac{4}{3}\tilde{\mu}\tilde{u}_{\tilde{x}} \tag{2.20}$$

where $\tilde{\mu}$ is the viscosity of the fluid.

The solar radiation received is considered as a heat flux/rate and can be expressed as [38]:

$$\tilde{\dot{q}}_s(\tilde{t}) = \gamma\alpha_g r_m \tilde{W}_a k_\theta \tilde{G}_{bt}(\tilde{t}) \tag{2.21}$$

where $\tilde{G}_{bt}$ is the beam solar radiation, W_a is the collector width, γ is the intercept factor, α_g is the absorbance of glass cover, r_m is the specular reflectance of the mirror and k_θ is the incident angle modifier.

The heat loss by convection is given by [38]:

$$\tilde{\dot{q}}_{conv} = \tilde{h}_w \left(\tilde{T} - \tilde{T}_a\right) \tag{2.22}$$

where $\tilde{T}_a$ is the ambient temperature and $\tilde{h}_w$ is the convective heat transfer coefficient given by [83]:

$$\tilde{h}_w = \frac{Nu_a k_a}{D_o}$$

with Nu_a denotes Nusselt number of air expressed by:

$$Nu_a = \begin{cases} 0.54Re_a^{0.52} + 0.4 \text{ if } 0.1 < Re_a < 1000 \\ 0.3Re_a^{0.6} \text{ if } 1000 < Re_a < 50000 \end{cases}$$

where Re_a is the air Reynolds number and k_a is the air thermal conductivity.

The radiation heat loss is described by [38]:

$$\dot{q}_{rad} = \epsilon_{rad}\tilde{\sigma}\left(\tilde{T}^4 - \tilde{T}_{sky}^4\right) \tag{2.23}$$

where $\tilde{T}_{sky}$ is the sky temperature assumed to be [38]:

$$\tilde{T}_{sky} = 0.0552\,\tilde{T}_a \tag{2.24}$$

with $\tilde{\sigma}$ as Stefan-Boltzmann constant and ϵ_{rad} as the emittance.

Eqs. (2.14)-(2.16) form a set of 3 equations for the 6 unknowns $\tilde{\rho}$, $\tilde{u}$, $\tilde{T}$, $\tilde{p}$, $\tilde{c_p}$ and $\tilde{k}$. As shown in Section 2.2, the constitutive relations of the used HTF, where the temperature dependence of the thermal properties can be approximated by polynomials (as in [38, 54]). In what follows, the subsequent equations that express the thermal characteristics of the HTF to complete the set of equations (2.14)-(2.16) are given by:

$$\tilde{\rho} = \tilde{a}_1\tilde{T} + \tilde{a}_2 \tag{2.25}$$

$$\tilde{k} = \tilde{b}_1\tilde{T} + \tilde{b}_2 \tag{2.26}$$

$$\tilde{c_p} = \tilde{c}_1\tilde{T} + \tilde{c}_2 \tag{2.27}$$

$$\tilde{\mu} = \tilde{d}_1 e^{\tilde{d}_2\tilde{T}} + \tilde{d}_3 e^{\tilde{d}_4\tilde{T}} \tag{2.28}$$

In the following section, the scaling of full set of equations will take place in order to simplify the heat transfer model for a single PTC.

Scaling

The governing equations, (2.14)-(2.16), and the fluid constitutive laws, (2.25)-(2.28), are scaled in order to obtain a dimensionless mathematical model, thus reducing the number of (dimensionless composed) parameters and to identify order of magnitudes in the various terms. The reference values are denoted by an index r, the dimensionless quantities have no index and no tildes, i.e. for a general quantity f:

$$f(x,t) = \frac{\tilde{f}(\tilde{x},\tilde{t})}{f_r} = \frac{\tilde{f}(xx_r, tt_r)}{f_r}. \tag{2.29}$$

The typical reference values used for scaling are associated with the real-world data of the considered power plant, namely, in the present case, the Ouarzazate Noor I [38]. Table 2.1 shows the typical reference values that are used for scaling based on the Noor I model parameters given in Table 1.2.

Henceforward, the cross-sectional area $\tilde{A} = \pi\left(\frac{\tilde{D}_i}{2}\right)^2$ is assumed to be constant in a single tube. The equations can now be scaled, and the typical reference values are inserted, resulting in the following system:

Ref.	Unit	Value	Ref.	Unit	Value
x_r	m	600.00	D_r	m	$6.60 \cdot 10^{-2}$
T_r	K	673.15	ρ_r	$kg \cdot m^{-3}$	$1.05 \cdot 10^{3}$
u_r	$m \cdot s^{-1}$	0.21	p_r	Pa	$3.30 \cdot 10^{6}$
$c_{p,r}$	$J \cdot kg^{-1} \cdot K^{-1}$	$1.26 \cdot 10^{3}$	k_r	$W \cdot m^{-1} \cdot K^{-1}$	0.47
μ_r	$W \cdot m^{-1} \cdot K^{-1}$	$1.24 \cdot 10^{-2}$	ξ_r	$-$	$2.99 \cdot 10^{-2}$
$G_{bt,r}$	$W \cdot m^{-1}$	10^{3}	$h_{w,r}$	$W \cdot m^{-2} \cdot K^{-1}$	37.37
σ_r	$W \cdot m^{-2} \cdot K^{-4}$	$5.67 \cdot 10^{-8}$			

TABLE 2.1: Reference values used for the scaling

$$\rho_t + (\rho u)_x = 0 \tag{2.30}$$

$$(\rho u)_t + \left(\rho u^2\right)_x = -\underbrace{\frac{p_r}{\rho_r u_r^2}}_{10^5} p_x - \underbrace{\frac{x_r U_r}{A_r}}_{10^4} \frac{U_i}{A} \frac{\xi}{8} \rho u|u| + \underbrace{\frac{4}{3} \frac{\mu_r}{\rho_r u_r x_r}}_{10^{-6}} (\mu u_x)_x \tag{2.31}$$

$$\begin{aligned} \rho c_p T_t + \rho c_p u T_x + \underbrace{\frac{u_r^2}{c_{p,r} T_r}}_{10^{-8}} \left\{ \rho \left(\frac{u^2}{2}\right)_t + \rho u \left(\frac{u^2}{2}\right)_x \right\} + \underbrace{\frac{p_r}{\rho_r c_{p,r} T_r}}_{10^{-3}} (up)_x = \underbrace{\frac{k_r}{\rho_r c_{p,r} u_r x_r}}_{10^{-8}} (k T_x)_x \\ + \underbrace{\frac{u_r^2 x_r U_r}{c_{p,r} T_r A_r} \frac{\xi}{8}}_{10^{-4}} \frac{U_i}{A} \rho u^2 |u| + \underbrace{\frac{u_r \mu_r}{\rho_r c_{p,r} T_r x_r} \frac{4}{3}}_{10^{-14}} (\mu u u_x)_x + \underbrace{\frac{W_r G_{bt,r} x_r}{\rho_r c_{p,r} u_r T_r A_r}}_{10^{1}} \gamma \alpha_g r_m \tilde{W}_a k_\theta G_{bt} \\ - \underbrace{\frac{x_r U_r h_{w,r}}{\rho_r c_{p,r} u_r A_r}}_{10^{1}} \frac{U_o}{A} h_w (T - T_a) - \underbrace{\frac{T_r^3 x_r U_r \sigma_r}{\rho_r c_{p,r} u_r A_r}}_{10^{1}} \frac{U_o}{A} \epsilon \sigma \left(T^4 - T_{sky}^4\right) \end{aligned} \tag{2.32}$$

where the order of magnitude is shown under each dimensionless coefficients. A series of small and very small parameters is observed, which will be utilized to simplify the model in the following section.

On the other hand, the scaling of thermal properties of HTF results in the following:

$$\rho = \frac{T_r}{\rho_r}\tilde{a}_1 T + \frac{\tilde{a}_2}{\rho_r} \tag{2.33}$$

$$k = \frac{T_r}{k_r}\tilde{b}_1 T + \frac{\tilde{b}_2}{k_r} \tag{2.34}$$

$$c_p = \frac{T_r}{c_{p,r}}\tilde{c}_1 T + \frac{\tilde{c}_2}{c_{p,r}} \tag{2.35}$$

$$\mu = \frac{\tilde{d}_1}{\mu_r} e^{T_r \tilde{d}_2 T} + \frac{\tilde{d}_3}{\mu_r} e^{T_r \tilde{d}_4 T} \tag{2.36}$$

To simplify the expression of the constitutive laws, the nondimenstional parameters are introduced:

$$\begin{aligned} &a_1 = \frac{T_r}{\rho_r}\tilde{a}_1,\ a_2 = \frac{\tilde{a}_2}{\rho_r}\ b_1 = \frac{T_r}{k_r}\tilde{b}_1\ b_2 = \frac{\tilde{b}_2}{k_r},\ c_1 = \frac{T_r}{c_{p,r}}\tilde{c}_1,\ c_2 = \frac{\tilde{c}_2}{c_{p,r}}, \\ &d_1 = \frac{\tilde{d}_1}{\mu_r},\ d_2 = T_r\tilde{d}_2,\ d_3 = \frac{\tilde{d}_3}{\mu_r},\ d_4 = T_r\tilde{d}_4 \end{aligned} \tag{2.37}$$

Asymptotic analysis

In this section, the order of magnitudes are examined (see also [1, 54]). Therefore, the terms with a very low order of magnitude are neglected. This leaves us with:

$$\rho_t + (\rho u)_x = 0 \tag{2.38}$$

$$(\rho u)_t + \left(\rho u^2\right)_x = -\frac{p_r}{\rho_r u_r^2} p_x - \frac{x_r U_r}{A_r}\frac{U_i}{A}\frac{\xi}{8}\rho u|u| \tag{2.39}$$

$$\begin{aligned} \rho c_p T_t + \rho c_p u T_x + \frac{p_r}{\rho_r c_{p,r} T_r}(up)_x &= \frac{u_r^2 x_r U_r}{c_{p,r} T_r A_r}\frac{\xi}{8}\frac{U_i}{A}\rho u^2|u| + \frac{W_r G_{bt,r} x_r}{\rho_r c_{p,r} u_r T_r A_r}\gamma\alpha_g r_m \tilde{W}_a k_\theta G_{bt} \\ &- \frac{x_r U_r h_{w,r}}{\rho_r c_{p,r} u_r A_r}\frac{U_o}{A} h_w (T - T_a) - \frac{T_r^3 x_r U_r \sigma_r}{\rho_r c_{p,r} u_r A_r}\frac{U_o}{A}\epsilon\sigma\left(T^4 - T_{sky}^4\right) \end{aligned} \tag{2.40}$$

In the following, it is noted that $\epsilon = \frac{\rho_r u_r^2}{p_r}$. An asymptotic approximation is made in terms of the parameter ϵ. Eqs. 2.38-2.40 can be written as follow:

$$\rho_t + (\rho u)_x = 0 \tag{2.41}$$

$$(\rho u)_t + \left(\rho u^2\right)_x = -\frac{1}{\epsilon} p_x - \eta \frac{U_i}{A} \frac{\xi}{8} \rho u |u| \tag{2.42}$$

$$\begin{aligned} \rho c_p T_t + \rho c_p u T_x + \delta \left(up\right)_x = \epsilon \delta \eta \frac{U_i}{A} \frac{\xi}{8} \rho u^2 |u| + \kappa \gamma \alpha_g r_m \tilde{W}_a k_\theta G_{bt} \\ - \varrho \frac{U_o}{A} h_w \left(T - T_a\right) - \varsigma \frac{U_o}{A} \epsilon \sigma \left(T^4 - T_{sky}^4\right) \end{aligned} \tag{2.43}$$

where $\eta = \frac{\xi x_r}{2 D_r} \sim \frac{1}{\epsilon}$, $\delta = \frac{p_r}{\tilde{c}_v \rho_r T_r} \sim \epsilon \cdot 10^{-1}$, $\kappa = \frac{W_r G_{bt,r} x_r}{\rho_r c_{p,r} u_r T_r A_r} \sim \epsilon \cdot 10^2$, $\varrho = \frac{x_r U_r h_{w,r}}{\rho_r c_{p,r} u_r A_r} \sim \epsilon \cdot 10^2$ and $\varsigma = \frac{T_r^3 x_r U_r \sigma_r}{\rho_r c_{p,r} u_r A_r} \sim \epsilon \cdot 10^2$.

The system quantities are developed asymptotically with respect to ϵ, i.e., for a quantity f:

$$f(x,t) = f_0(x,t) + \epsilon f_1(x,t) + \mathcal{O}(\epsilon^2) \tag{2.44}$$

By inserting these quantities into the system of equations 2.41-2.43, the individual equations are arranged according to the leading order of magnitude of ϵ, yielding:

$$(\rho_0)_t + (\rho_0 u_0)_x = 0 \tag{2.45}$$

$$(p_0)_x = -\epsilon \delta \frac{U_i}{A} \frac{\xi}{8} \rho_0 u_0 |u_0| \tag{2.46}$$

$$\rho_0 c_{p,0} \left(T_0\right)_t + \rho_0 c_{p,0} u_0 \left(T_0\right)_x = \kappa \gamma \alpha_g r_m \tilde{W}_a k_\theta G_{bt} - \varrho \frac{U_o}{A} h_w \left(T_0 - T_a\right) - \varsigma \frac{U_o}{A} \epsilon \sigma \left(T_0^4 - T_{sky}^4\right) \tag{2.47}$$

In the following model, only the most relevant phenomena are included,, namely, friction losses in the momentum balance, the solar input, and the radiative and convective heat losses in the energy balance. The model can be rewritten and simplified using Eq. 2.45 in Eq. 2.47. The following complete system of equations is obtained through this process (with the index $()_0$ being

omitted):

$$\rho_t + (\rho u)_x = 0 \tag{2.48}$$

$$p_x = -\epsilon\delta \frac{U_i}{A}\frac{\xi}{8}\rho u|u| \tag{2.49}$$

$$u_x = -\frac{a_1}{\rho^2 c_p}\left\{\kappa\gamma\alpha_g r_m \tilde{W}_a k_\theta G_{bt} - \varrho\frac{U_o}{A}h_w\left(T - T_a\right) - \varsigma\frac{U_o}{A}\epsilon\sigma\left(T^4 - T_{sky}^4\right)\right\} \tag{2.50}$$

$$T = \frac{\rho - a_2}{a_1} \tag{2.51}$$

$$c_p = c_1 T + c_2 \tag{2.52}$$

This is a coupled system of 3 first order nonlinear PDEs and 4 linear algebraic relation. Consequently, the system is complemented with the initial data for the temperature:

$$T(x, 0) = T_0 \tag{2.53}$$

where the initial condition for the density ρ can be obtained using Eq. 2.63.

Now, 3 physically meaningful boundary conditions are needed. This is achieved by prescribing the pressures, the velocity and temperature at the inlet or outlet pressure instead of inlet velocity, Eq. 2.54, and consequently, the other quantities are determined via Eqs. 2.63-2.64.

$$p(0, t) = p_l,\ T(0, t) = T_l,\ u(0, t) = u_l \text{ or } p(1, t) = p_r \tag{2.54}$$

2.3.2 Space-Independent Model

In this section, a space-independent model is introduced in order to reduce the computation costs of large network problems. Eqs. 2.48-2.50 are integrated over

the length of the pipe, as follow:

$$\int_0^L \rho_t dx + \rho_{\text{out}} u_{\text{out}} - \rho_{\text{in}} u_{\text{in}} = 0 \tag{2.55}$$

$$p_{\text{out}} - p_{\text{in}} = -\epsilon\delta \frac{U_i}{A} \int_0^L \frac{\xi}{8} \rho u|u| dx \tag{2.56}$$

$$u_{\text{out}} - u_{\text{in}} = -\int_0^L \frac{a_1}{\rho^2 c_p} \left\{ \kappa\gamma\alpha_g r_m \tilde{W}_a k_\theta G_{bt} - \varrho \frac{U_o}{A} h_w \left(T - T_a\right) - \varsigma \frac{U_o}{A} \epsilon\sigma \left(T^4 - T_{sky}^4\right) \right\} dx \tag{2.57}$$

$$T = \frac{\rho - a_2}{a_1} \tag{2.58}$$

$$c_p = c_1 T + c_2 \tag{2.59}$$

where the indices $(\cdot)_{\text{in}}$ and $(\cdot)_{\text{out}}$ refer to the values of a quantity at the inlet and outlet, respectively.

Simple trapezoidal rule is then applied by approximating the remaining integrals at the inlet and outlet points, resulting in the following set of equations:

$$\frac{L}{2}\rho_{\text{out},t} + \rho_{\text{out}} u_{\text{out}} = \rho_{\text{in}} u_{\text{in}} - \frac{L}{2}\rho_{\text{in},t} \tag{2.60}$$

$$p_{\text{out}} = p_{\text{in}} - \frac{L}{2}\epsilon\delta \frac{U_i}{A} \left(\frac{\xi_{\text{out}}}{8} \rho_{\text{out}} u_{\text{out}} |u_{\text{out}}| + \frac{\xi_{\text{in}}}{8} \rho_{\text{in}} u_{\text{in}} |u_{\text{in}}| \right) \tag{2.61}$$

$$\begin{aligned} u_{\text{out}} = u_{\text{in}} - \frac{L}{2} \Bigg[& \frac{a_1}{\rho_{\text{out}}^2 c_{p,\text{out}}} \left\{ \kappa\gamma\alpha_g r_m \tilde{W}_a k_\theta G_{bt} - \varrho \frac{U_o}{A} h_w \left(T_{\text{out}} - T_a\right) - \varsigma \frac{U_o}{A} \epsilon\sigma \left(T_{\text{out}}^4 - T_{sky}^4\right) \right\} \\ & + \frac{a_1}{\rho_{\text{in}}^2 c_{p,\text{in}}} \left\{ \kappa\gamma\alpha_g r_m \tilde{W}_a k_\theta G_{bt} - \varrho \frac{U_o}{A} h_w \left(T_{\text{in}} - T_a\right) - \varsigma \frac{U_o}{A} \epsilon\sigma \left(T_{\text{in}}^4 - T_{sky}^4\right) \right\} \Bigg] \end{aligned} \tag{2.62}$$

$$T_{\text{out}} = \frac{\rho_{\text{out}} - a_2}{a_1} \tag{2.63}$$

$$c_{p,\text{out}} = c_1 T_{\text{out}} + c_2 \tag{2.64}$$

This simplification of the previous model remove the dependency on the space variable x to only a time-dependent model, where classical numerical time-scheme can be used.

2.3.3 Network Model

PTPPs typically comprise multiple parallel rows of solar collectors, where every row contains a number of collectors connected in series, as demonstrated by the schematic representation of a solar field in Fig. 2.6. A network model is introduced that integrates multiple tubes by building upon the single tube model discussed previously. This network model considers the presence of n_p separate tubes interconnected at n_v node with the possibility for multiple tubes to be interconnected at a single node. Various properties are incorporated in each tube, denoted by the index i. These properties include temperature (T^i), velocity (u^i), specific heat capacity (c_p^i), density (ρ^i) and pressure (p^i). The single-tube model described in the previous section is employed within each individual tube. Various parameters of the tubes may differ from one to another, e.g. the length (L^i), the cross-sectional area (A^i) and the diameter (D^i).

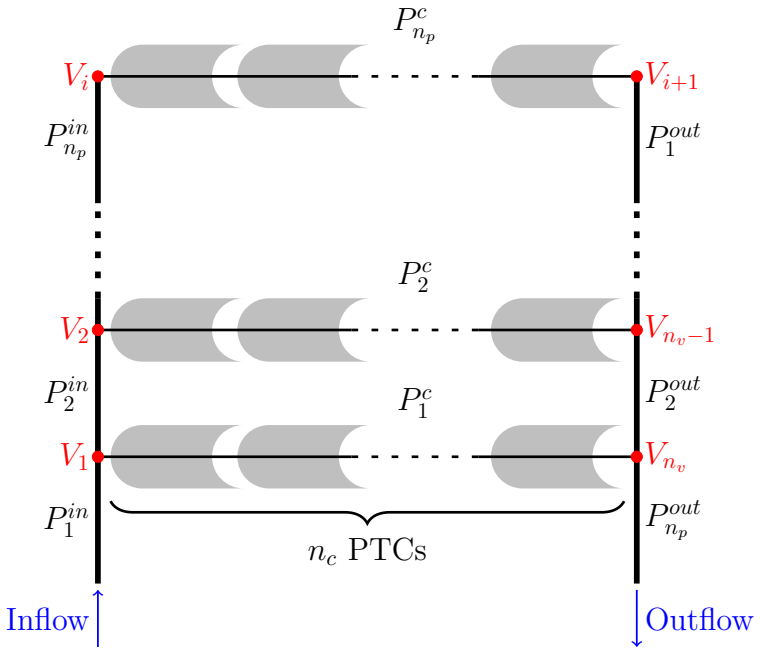

FIG. 2.6: Illustration depicting a network of pipes within a solar field in PTPP [3].

The fluid in each tube is described as follows:

$$\rho_t^i + \left(\rho^i u^i\right)_x = 0 \tag{2.65}$$

$$p_x^i = -\epsilon\delta \frac{U_i^i}{A^i}\frac{\xi^i}{8}\rho^i u^i |u^i| \tag{2.66}$$

$$u_x^i = -\frac{a_1}{\left(\rho^i\right)^2 c_p^i}\left\{\kappa\gamma\alpha_g r_m \tilde{W}_a k_\theta G_{bt}^i - \varrho\frac{U_o^i}{A^i}h_w^i\left(T^i - T_a^i\right) - \varsigma\frac{U_o^i}{A^i}\epsilon\sigma\left(\left(T^i\right)^4 - \left(T_{sky}^i\right)^4\right)\right\} \tag{2.67}$$

$$\rho^i = a_1 T^i + a_2 \tag{2.68}$$

$$c_p^i = c_1 T^i + c_2 \tag{2.69}$$

The boundary conditions are added, as in 2.54, with the pressure p_l and temperature T_l being assigned at the inlet tube and the pressure p_r at the outlet tube. The initial condition, as in 2.53, is provided in the entire network of pipes.

$$T^i(x,0) = T_0, \text{ for } i = 1,\ldots,n_p \tag{2.70}$$

$$p_{\text{in}}(0,t) = p_l,\ T_{\text{in}}(0,t) = T_l,\ p_{\text{out}}(1,t) = p_r \tag{2.71}$$

In the network, node conditions need to be defined, which will act as boundary conditions for the internal (or non-external) ends of the tubes. 3 boundary conditions per tube are required, for example, inlet and outlet pressures and the inlet density condition. This results in a total of $3 \cdot n_p$ boundary conditions for the entire network.

The assumptions for the node dynamics are made that the fluid is homogeneously mixed, resulting in: 1) a single pressure value at each node, 2) a single density value for each inlet node of a pipe. This reduces the unknowns to a single pressure value and a single density value at each node. Physical reasonable and necessary node conditions are formulated as follow ([55, 80]):

i) Mass is conserved in the nodes, i.e. the in and outgoing mass fluxes are balanced

$$\sum_{\text{sign}(i,j)\neq 0} \text{sign}(i,j)\rho^i u^i A^i = 0 \tag{2.72}$$

ii) Inner energy is conserved in the nodes, i.e. the in and outgoing fluxes for the inner energy are balanced

$$\sum_{\text{sign}(i,j)\neq 0} \text{sign}(i,j)\rho^i u^i T^i A^i = 0 \tag{2.73}$$

where the function sign(tube i, node j) indicates the end of the tube at which i the node j is located

$$\text{sign(tube } i\text{, node } j) = \begin{cases} 1 & \text{left end of the tube } i \text{ ends in node } j \\ -1 & \text{right end of the tube } i \text{ ends in node } j \\ 0 & \text{no connection of tube } i \text{ with node } j \end{cases}$$

Using Eq. 2.68 in the inner energy balance at the nodes, Eq. 2.73, then using Eq. 2.72 and the fact all outflowing tubes have the same (well mixed) density, the following relation is obtained at every node $j = 1, ..., n_v$:

$$\sum_{sign(i,j)u^i<0} sign(i,j)(\rho^i)^2 u^i A^i \tag{2.74}$$

$$= -\sum_{sign(i,j)u^i>0} sign(i,j)(\rho^i)^2 u^i A^i \tag{2.75}$$

$$= -\rho_{\text{in},j} \sum_{sign(i,j)u^i>0} sign(i,j)\rho^i u^i A^i \tag{2.76}$$

By applying Eq. 2.72, coupling conditions for the outflow density in node j are obtained:

$$\rho_{\text{in},j} = \frac{\sum\limits_{sign(i,j)u^i<0} \left((\rho^i)^2 u^i A^i\right)\Big|_{x=L^i}}{\sum\limits_{sign(i,j)u^i<0} (\rho^i u^i A^i)|_{x=L^i}}, \quad j = 1, ..., n_v \tag{2.77}$$

which only depends on inflow data at the related node.

It is noted that the conservation of mass in every node is ensured by the construction of (2.77). On the other hand, the conservation of inner energy, Eq. 2.73 yields to the following, for $j = 1, ..., n_v$:

$$\sum_{sign(j,i)>0} \left(\rho^i u^i A^i\right)_{x=0} = \sum_{sign(j,i)<0} \left(\rho^i u^i A^i\right)_{x=L_i} \tag{2.78}$$

However, the following equations describe the calculation of ΔP^i – the pressure difference in the tube i between the right and left node – in function of the velocity u^i, for $i = 1, ..., n_p$:

$$\Delta P^i = -\int_0^1 \frac{C_{in}^i}{A^i} \frac{f}{8} \rho^i u^i |u^i| dx \tag{2.79}$$

Within the solar field of a PTPP, the above network model is introduced to study the flow of HTF, where, for $i = 1, ..., n_p$, the unknown variables are T^i, u^i, μ^i, c_p^i, ρ^i, p^i. In addition, for $j = 1, ..., n_v$, the unknown obtained from the connecting conditions is $\rho_{\text{in},j}$, P_j. These variables can be effectively solved using numerical methods. Based on this, the solution to the network problem is prepared.

2.4 Simplified Temperature Model

2.4.1 Single Pipe Model

In the following, a more simplified mathematical model for the heat-transfer flow in a collector is being introduced which focuses on the temperature variation of HTF in a single pipe. Based on the numerical tests of the previous model, the velocity is noted to be almost constant with respect to space and time. With the assumption of a constant velocity and disregard of the pressure, the following model is presented as obtained by the asymptotic analysis in Eqs. 2.45-2.47:

$$\rho c_p (T)_t + \rho c_p u (T)_x = \kappa \gamma \alpha_g r_m \tilde{W}_a k_\theta G_{bt} - \varrho \frac{U_o}{A} h_w (T - T_a) - \varsigma \frac{U_o}{A} \epsilon \sigma \left((T)^4 - (T_{sky})^4 \right) \tag{2.80}$$

$$\rho = a_1 T + a_2 \tag{2.81}$$

$$c_p = c_1 T + c_2 \tag{2.82}$$

This is a coupled system of 1 first order nonlinear PDEs and 2 linear algebraic relation. Consequently, the system is complemented with the initial and inlet data for the temperature, as in Eqs. 2.53-2.54.

2.4.2 Space-Independent Model

Likewise the previous section, the model is further simplified. Space-independent model is then introduced in order to reduce the computation costs of large network

problems. Eq. 2.80 is integrated over the length of the pipe, as follow:

$$\int_0^L \rho c_p \left(T\right)_t dx + \rho_{\text{out}} c_{p,\text{out}} u_{\text{out}} T_{\text{out}} - \rho_{\text{out}} c_{p,\text{out}} u_{\text{out}} T_{\text{in}} = L\kappa\gamma\alpha_g r_m \tilde{W}_a k_\theta G_{bt} \\ - \int_0^L \varrho \frac{U_o}{A} h_w \left(T - T_a\right) dx - \int_0^L \varsigma \frac{U_o}{A} \epsilon\sigma \left((T)^4 - (T_{sky})^4\right) dx \tag{2.83}$$

$$\rho = a_1 T + a_2 \tag{2.84}$$

$$c_p = c_1 T + c_2 \tag{2.85}$$

Similarly, the trapezoidal rule is then applied by approximating the remaining integrals at the inlet and outlet points, resulting in the following set of equations:

$$\frac{L}{2}\rho_{\text{out}} c_{p,\text{out}} \left(T_{\text{out}}\right)_t + \rho_{\text{out}} c_{p,\text{out}} u_{\text{out}} T_{\text{out}} = \rho_{\text{out}} c_{p,\text{out}} u_{\text{out}} T_{\text{in}} - \frac{L}{2}\rho_{\text{in}} c_{p,\text{in}} \left(T_{\text{in}}\right)_t \\ + L\kappa\gamma\alpha_g r_m \tilde{W}_a k_\theta G_{bt} - \frac{L}{2}\left(\varrho \frac{U_o}{A} h_w \left(T_{\text{out}} - T_a\right) + \varsigma \frac{U_o}{A} \epsilon\sigma \left((T_{\text{out}})^4 - (T_{sky})^4\right)\right. \\ \left. + \varrho \frac{U_o}{A} h_w \left(T_{\text{in}} - T_a\right) + \varsigma \frac{U_o}{A} \epsilon\sigma \left((T_{\text{in}})^4 - (T_{sky})^4\right)\right) \tag{2.86}$$

$$\rho = a_1 T + a_2 \tag{2.87}$$

$$c_p = c_1 T + c_2 \tag{2.88}$$

This simplification of the initial model remove the dependency on the velocity and the space variable x to only a time-dependent temperature model, where classical numerical time-scheme can be used. The assumptions for the node dynamics are made that the fluid is homogeneously mixed, resulting in: 1) a single pressure value at each node, 2) a single density value for each inlet node of a pipe. This reduces the unknowns to a single pressure value and a single density value at each node.

2.4.3 Network Model

As stated earlier in the chapter, a network model is introduced that integrates multiple tubes by building upon the single tube model. This network model takes into account the presence of n_p separate tubes interconnected at n_v node with the possibility for multiple tubes to be interconnected at a single node. Various properties are incorporated in each tube, denoted by the index i. These properties

include temperature (T^i), velocity (u^i), specific heat capacity (c_p^i), density (ρ^i). The single-tube model described in the previous section is employed within each signle tube. Various parameters of the tubes may differ from one to another, e.g. the length (L^i), the cross-sectional area (A^i) and the diameter (D^i).

The fluid in each tube is described as follows:

$$\begin{aligned}&\rho^i c_p^i \left(T^i\right)_t + \rho^i c_p^i u^i \left(T^i\right)_x = \kappa\gamma\alpha_g r_m \tilde{W}_a k_\theta G_{bt}^i - \varrho\frac{U_o^i}{A^i} h_w^i \left(T^i - T_a^i\right) \\ &- \varsigma\frac{U_o^i}{A^i}\epsilon\sigma\left((T^i)^4 - (T_{sky}^i)^4\right)\end{aligned} \tag{2.89}$$

$$\rho^i = a_1 T^i + a_2 \tag{2.90}$$

$$c_p^i = c_1 T^i + c_2 \tag{2.91}$$

For the network model, the constant velocity can differ from one pipe to another due to the change of geometrical properties of the pipe. To calculate the velocity for each pipe, simplified form of the conservation of inner energy, Eq. 2.73, for $j = 1, ..., n_v$ is obtained as follows:

$$\sum_{sign(j,i)>0} \left(\rho^i u^i A^i\right)_{x=0} = \sum_{sign(j,i)<0} \left(\rho^i u^i A^i\right)_{x=L_i} \tag{2.92}$$

The boundary and initial conditions are added, where the temperature T_l being assigned at the inlet tube and the initial temperature is provided in the entire network of pipes. The connecting conditions are nonexistent for this model, where the assumption for the node dynamics is only that the fluid is homogeneously mixed, resulting in a single temperature value at each node. These conditions affect the computation time as the coupling conditions usually results in solving a nonlinear problem for each pipe and each time iteration.

The details of the numerical realization of the solution to the network problem are presented in the following section.

2.5 energetic and exergetic efficiencies

The instantaneous energetic efficiency refers to the ratio between the useful thermal energy gained by the working fluid to the available solar beam energy falling onto

the PTC reflector [38]. It is expressed as:

$$\eta = \frac{A\rho u \int_{T_l}^{T_r} c_p(T)dT}{W_a L G_{bt}} \tag{2.93}$$

where W_a is the width of the collector, L the length of the collector and G_{bt} is the beam incident radiation.

The exergetic efficiency can be defined as the ratio of gain exergy to available solar radiation exergy, [38], and can be expressed as:

$$\eta_{ex} = \frac{A\rho u \left(\int_{T_l}^{T_r} c_p(T)dT - T_a \int_{T_l}^{T_r} \frac{c_p(T)}{T} dT \right)}{W_a L G_{bt} \left[1 - \frac{4}{3} + \left(\frac{T_a}{T_{sun}} \right) + \frac{1}{3} \left(\frac{T_a}{T_{sun}} \right)^4 \right]} \tag{2.94}$$

where T_{sun} is the sun's apparent temperature taken to be 6000 K.

2.6 Numerical Simulation

2.6.1 Single Pipe Model

In this section, the algorithm for a single pipe is first introduced, followed by the initial and boundary values. The coupling conditions are then used for the calculation of missing boundary values of all pipes.

In order to solve the system of equations 2.48-2.52, a temporal and spatial discretization is required. The discrete grid points for space and time are denoted, respectively, by $x_1, \ldots, x_{n_x}$ and $t_1, \ldots, t_{n_t}$. The discrete variables are accordingly provided with the indexing (n, j), where the first index is related to the time coordinate, the second to the spatial coordinate.

In the following, the index for the pipe number is dropped as the algorithm is introduced for a single pipe. The explicit upwind method is used to solve the mass conservation, Eq. 2.48, where CFL-condition is preserved [53]. Calculation of the discrete temperature values result from the linear relationship between T and ρ, Eq. 2.51. On the other hand, the velocity solution can be obtained by integrating Eq. (2.50), as follows:

$$u(t,x) = v(t) - \int_0^x \frac{a_1}{\rho^2 c_p} \left\{ \kappa\gamma\alpha_g r_m \tilde{W}_a k_\theta G_{bt} - \varrho \frac{U_o}{A} h_w \left(T - T_a\right) - \varsigma \frac{U_o}{A} \epsilon\sigma \left(T^4 - T_{sky}^4\right) \right\} ds \tag{2.95}$$

where $v = v(t)$ (space independent) represents the value of the velocity at the pipe inlet. To calculate $v = v(t)$, the pressure equation 2.49 is integrated over the whole pipe (from $x = 0$ to $x = L$) and by inserting (2.95) alongside the two pressure boundary values, the following equation for $v = v(t)$ is obtained:

$$\begin{aligned} p(1,t) - p(0,t) = &- \epsilon\delta\frac{U_i}{A}\int_0^1 \frac{\xi}{8}\rho\left(v(t) - \int_0^x \frac{a_1}{\rho^2 c_p}\left\{\kappa\gamma\alpha_g r_m \tilde{W}_a k_\theta G_{bt} - \varrho\frac{U_o}{A}h_w\left(T - T_a\right)\right.\right. \\ &\left.\left. -\varsigma\frac{U_o}{A}\epsilon\sigma\left(T^4 - T_{sky}^4\right)\right\} ds\right) \times \left| v(t) + \int_0^x -\frac{a_1}{\rho^2 c_p}\left\{\kappa\gamma\alpha_g r_m \tilde{W}_a k_\theta G_{bt}\right.\right. \\ &\left.\left. -\varrho\frac{U_o}{A}h_w\left(T - T_a\right) - \varsigma\frac{U_o}{A}\epsilon\sigma\left(T^4 - T_{sky}^4\right)\right\} ds\right| \end{aligned} \tag{2.96}$$

After the density, temperature and velocity are solved for the respective time step, the pressure can also be calculated. In order to take into account the two given pressure boundary values, Eq. 2.49 is differentiated with respect to x as follows:

$$p_{xx} = -\frac{\epsilon\eta}{D_i}\left(\rho u|u|\right)_x \tag{2.97}$$

Finally, the pressure values are obtained by solving the above equation using second-order central finite different scheme.

2.6.2 Network Model

The previous algorithm is limited to a single pipe. The network approach still requires the numerical implementation of the coupling conditions in order to derive the required boundary values for the individual pipes. As previously discussed, a boundary value for the density is required for the explicit upwind method. For internal pipes, the boundary value for the density is determined via the equation 2.68 at every node $j = 1, ..., n_v$. With the input density determined in this way for each pipe, the continuity equation can be solved using the explicit upwind methods.

Furthermore, the n_v pressure values at the nodes are required to calculate the speed and the pressure in the individual pipes. Therefore, the following n_v equations at the nodes and the n_p equations for the pipes form a non-linear system

of equations for $i = 1, \ldots, n_p$, and $j = 1, \ldots, n_v$.

$$\Delta p^i = -\epsilon\delta\frac{U_i^i}{A^i}\int_0^1 \frac{\xi^i}{8}\rho^i \left(v^i - \int_0^s \frac{a_1}{(\rho^i)^2 c_p^i}\left\{\kappa\gamma\alpha_g r_m \tilde{W}_a k_\theta G_{bt}^i - \varrho\frac{U_o^i}{A^i}h_w^i\left(T^i - T_a\right)\right.\right.$$
$$\left.\left. -\varsigma\frac{U_o^i}{A^i}\epsilon\sigma\left((T^i)^4 - T_{sky}^4\right)\right\} ds\right) \times \left|v^i + \int_0^s -\frac{a_1}{(\rho^i)^2 c_p^i}\left\{\kappa\gamma\alpha_g r_m \tilde{W}_a k_\theta G_{bt}^i\right.\right.$$
$$\left.\left. -\varrho\frac{U_o^i}{A^i}h_w^i\left(T^i - T_a\right) - \varsigma\frac{U_o^i}{A^i}\epsilon\sigma\left((T^i)^4 - T_{sky}^4\right)\right\} ds\right| \tag{2.98}$$

$$\sum_{sign(i,j)u^i>0} \rho^i v^i A^i = \sum_{sign(i,j)u^i<0} \rho^i \left(v^i + \int_0^1 -\frac{a_1}{(\rho^i)^2 c_p^i}\left\{\kappa\gamma\alpha_g r_m \tilde{W}_a k_\theta G_{bt}^i\right.\right.$$
$$\left.\left. -\varrho\frac{U_o^i}{A^i}h_w^i\left(T^i - T_a\right) - \varsigma\frac{U_o^i}{A^i}\epsilon\sigma\left((T^i)^4 - T_{sky}^4\right)\right\} ds\right) A^i \tag{2.99}$$

Finally, $n_v + n_p$ equations are solved to obtain the n_v pressure values at the nodes P_j and the n_p input velocities v^i of the pipes. The required boundary values for each individual pipe within the entire network are now made available and the quantities velocity, pressure and temperature can be determined according to the procedure explained above.

2.6.3 Simplified Model

In this section, the algorithm for the simplified temperature model is discussed. In order to solve the temperature equation 2.89, a temporal and spatial discretization is introduced similar to previous section. The discrete grid points for space and time are denoted, respectively, by x_1, ..., x_{n_x} and t_1, ..., t_{n_t}. The discrete variables are accordingly provided with the indexing (n, j), where the first index is relating to the time coordinate, the second to the spatial coordinate.

The explicit upwind method is used to solve the temperature equation. Calculation of the discrete temperature values requires updating the density and specific heat capacity values in each time iteration using the linear relations with respect to temperature, Eqs. 2.90-2.91. On the other hand, the constant velocity is calculated for all pipes using Eq. 2.92.

Chapter 3

Optimization of Thermal Performance

3.1 Introduction

The matter of concern in this chapter shifts toward optimizing the thermal performance of PTPPs. These power plants have become one of the pillars of renewable energy generation, and to enhance their efficiency, a simulation model is employed that allows for design and optimization of such systems. Our model enables us to optimize input data, such as system parameters, like network structure and thermofluid properties. While single PTCs have been extensively studied, little to no research has been done on modeling and optimizing PTPP within larger network systems. The chapter's core revolves around the mathematical optimization problem of maximizing output energy, considering various HTFs and system parameters.

The chapter comprises three sections. The first section is dedicated to introducing the power functional and its role in optimizing PTPPs. In the second section, the optimization problem is formulated, where the objectives and constraints are defined. In the third and final section, details on the algorithmic approaches used to optimize PTPP for maximum efficiency are presented.

3.2 Power Functional

The network model and numerical simulation of PTPPs for a given set of parameters and initial and boundary data were presented in the previous chapter.

As previously mentioned, it is preferable to move a step further and, as deemed necessary by the application, optimize the output. The power output is a natural quantity to be optimized. During an operational phase, an important control variable is the pressure drop between the outlet and inlet to the solar field, denoted as Δp.

The power P is the energy converted per unit of time, and it can be defined as $P = \frac{\Delta E}{\Delta t}$, where E represents the energy. The thermal (gross) output of a power plant is the quantity of heat generated per unit of time. In addition, the fluid is pushed through the network by employing pumping power. Eventually, the most interesting quantity is the net power, which is the difference between the gross power and the power required to run the system.

The thermal output is initiated with the calculation of the amount of heat, $\tilde{P}_{thermal}$, which is generated by a temperature difference, as follows:

$$\tilde{P}_{\text{thermal}} = \tilde{A}\tilde{\rho}\tilde{u}\left(\tilde{c}_p(\tilde{T}_{\text{out}})\tilde{T}_{\text{out}} - \tilde{c}_p(\tilde{T}_{\text{in}})\tilde{T}_{\text{in}}\right) \tag{3.1}$$

where $\tilde{T}_{in}, \tilde{T}_{out}$ are the in and outlet temperatures, $\tilde{c}_p$ the (temperature-dependent) specific heat capacity and $\tilde{A}\tilde{\rho}\tilde{u}$ the fluid mass push through the tubes per time.

Here, incompressibility is assumed, therefore the inflowing mass is equal to the outflowing mass. When applied to our network, the relevant outgoing tube or tubes (if more than one outgoing tube) yield the following results:

$$\tilde{P}_{\text{thermal}} = \left(\tilde{A}_{\text{out}}\tilde{\rho}_{\text{out}}\tilde{u}_{\text{out}}\left(\tilde{c}_p(\tilde{T}_{\text{out}})\tilde{T}_{\text{out}} - \tilde{c}_p(\tilde{T}_{\text{in}})\tilde{T}_{in}\right)\right)\Big|_{\tilde{x}=\tilde{L}_{out}} \tag{3.2}$$

The integration of $\tilde{P}_{\text{thermal}}$ over time is carried out to account for the performance over the entire simulation period. Furthermore, the fact that there can be several output pipes is also taken into account, and the sum over the corresponding pipes is formed, as follows:

$$\tilde{J}_{\text{thermal}} = \int_0^{\tilde{t}_f} \sum_{\text{i=out}} \left(\tilde{A}^i_{\text{out}}\tilde{\rho}^i_{\text{out}}\tilde{u}^i_{\text{out}} \cdot \left(\tilde{c}_p(\tilde{T}^i_{\text{out}})\tilde{T}^i_{\text{out}} - \tilde{c}_p(\tilde{T}_{\text{in}})\tilde{T}_{\text{in}}\right)\right)\Big|_{\tilde{x}=\tilde{L}_i} dt \tag{3.3}$$

where $\tilde{J}_{\text{thermal}}$ represents the gross power generated in the solar field by solar thermal heating. The power functional is still subject to dimensions.

In our functional, the required pumping power to generate the pressure is taken into account. This is calculated according to Sterner and Stadler [84], as follows:

$$P_{\text{pump}} = \tilde{A}_{\text{in}}\tilde{u}_{\text{in}}\Big|_{\tilde{x}=\tilde{0}} \frac{\Delta\tilde{p}}{\eta_{\text{pump}}} \tag{3.4}$$

where $0 < \eta_{\text{pump}} < 1$ designates the efficiency of the pump and $\Delta p = p_{\text{in}} - p_{\text{out}}$ the produced overpressure between inlet and outlet pipes.

Since pumps are always active at the inlet(s), the following is obtained by integrating over the simulation period:

$$\tilde{J}_{\text{pump}} = \int_0^{\tilde{t}_f} \sum_{\text{i=in}} \tilde{A}^i_{\text{in}}\tilde{u}^i_{\text{in}}\Big|_{\tilde{x}=\tilde{0}} \frac{\tilde{p}^i_{\text{in}} - \tilde{p}_{\text{out}}}{\eta_{\text{pump}}} dt \tag{3.5}$$

In our model, it is assumed that the pump is installed at the entrance of the first pipe (only one inlet pipe). Overall, the following net power functional $\tilde{J}$ can now be set up:

$$\tilde{J} = \int_0^{\tilde{t}_f} \sum_{\text{i=out}} \left(\tilde{A}^i_{\text{out}}\tilde{\rho}^i_{\text{out}}\tilde{u}^i_{\text{out}} \cdot \left(\tilde{c}_p(\tilde{T}^i_{\text{out}})\tilde{T}^i_{\text{out}} - \tilde{c}_p(\tilde{T}_{\text{in}})\tilde{T}_{\text{in}}\right)\right)\Big|_{\tilde{x}=\tilde{L}_i} - \tilde{A}_{\text{in}}\tilde{u}_{\text{in}}\Big|_{\tilde{x}=\tilde{0}} \frac{\tilde{p}_{\text{in}} - \tilde{p}_{\text{out}}}{\eta_{\text{pump}}} dt \tag{3.6}$$

The given net power functional represents the amount of net energy produced by the power station over the time interval $[0, \tilde{t}_f]$. What remains to do next is to scale the functional using the reference values from the subsection 2.3.1 (the reference value for $\tilde{J}$ is given by $T_r\rho_r u_r A_r$), the scaled power functional is then given as follows:

$$J = \int_0^{t_f} \sum_{\text{i=out}} \left(A^i_{\text{out}}\rho^i_{\text{out}}u^i_{\text{out}} \cdot \left(c_p(T^i_{\text{out}})T^i_{\text{out}} - c_p(T_{\text{in}})T_{\text{in}}\right)\right)\Big|_{x=L_i} - A_{\text{in}}u_{\text{in}}|_{x=0} \frac{p_{\text{in}} - p_{\text{out}}}{\eta_{\text{pump}}} dt \tag{3.7}$$

In the next section, the optimization problem with the appropriate constraints will be shown.

3.3 Optimization Problem

In the previous sections, the model of a solar field and the associated net energy performance functional were presented. Thus, the aim is to maximize the

net energy performance functional, Eq. 3.7 with respect to single or multiple parameters.

3.3.1 Single Variable Constrained Optimization

For the case of a single parameter optimization problem, the maximization of the presented net power functional is done by looking for the optimal value of the pressure drop in the network system under the additional constraint $\max T^{out} < T_c$ since the HTF should not go above the critical temperature (in the case of Therminol VP-1 $T_c = \frac{663.15\ K}{T_r}$ $(390\ ^{\circ}C)$).

Therefore, the optimization problem is summarized as:

$$\begin{cases} \underset{(\Delta P)}{\text{maximize}} & J_p\left(\Delta P\right) \\ \text{subject to} & \text{Eqs. 2.65-2.69} \\ & \max T^{out} < T_c \end{cases} \tag{3.8}$$

3.3.2 Multivariable Constrained Optimization

In the case of multivariable problem, the following parameters can be considered: inlet velocity u_l, nanoparticle volume fraction φ (in the case of nanofluids), inlet temperature, T_l, and ratio of inlet/outlet pipe diameter to the collector pipe diameter r_D.

The optimization problem is coupled with the following constraints:

- The system of equations, Eqs. 2.65-2.69, for the network of the solar field are fulfilled,
- The maximum outlet temperature is less than T_c, which is the critical temperature of HTF,
- To generate steam, the outlet temperature needs to be higher than the boiling point of water,
- The inlet velocity is bounded between 0.01 m/s and 5 m/s,
- The base fluid should not contain a volume fraction of nanoparticles exceeding 5%,

- The inlet temperature is bounded between 300 K and 600 K,
- The ratio r_D is bounded between 1 and 15.

Therefore, the optimization problem is summarized as:

$$\begin{cases} \underset{(u_l,\ \varphi,\ T_l,\ r_D)}{\text{maximize}} & J_p\left(u_l,\ \varphi,\ T_l,\ r_D\right) \\ \text{subject to} & \text{Eqs. 2.65-2.69} \\ & \max\left(T_{out}\right) \leq T_c \\ & \text{avg}\left(T_{out}\right) \geq 375 \text{ K} \\ & 0.01 \text{ m/s} \leq u_l \leq 5 \text{ m/s} \\ & 0\% \leq \varphi \leq 5\% \\ & 300 \text{ K} \leq T_l \leq 600 \text{ K} \\ & 1 \leq r_D \leq 15 \end{cases} \tag{3.9}$$

In the next section, the numerical realizations of this optimization are demonstrated (in MATLAB, based on the optimization toolbox).

3.4 Optimization Algorithm

In order to optimize the nonlinear energy performance functional subject to the aforementioned constraints, a sequence of approximate minimization problems is solved using the interior-point approach. [85–87]. At each iteration, the algorithm proceeds by following two distinct types of steps to solve the approximate problem: A direct step in (x, s) (x is the optimization variable vector and s is the slack variables vector), where an attempt is made to solve the Karush-Kuhn-Tucker (KKT) conditions, [88, 89], for the approximate problem using a linear approximation (Newton step). Using a trust region, a subsequent step of conjugate gradient (CG) is executed.

The presented algorithm, as shown in Fig. 3.1 for the multivariable constrained optimization problem, is implemented in MATLAB, where numerical experiments and optimization procedures using the above explained setting of NOOR I in Morocco with different HTFs and different model parameters are going to be compared.

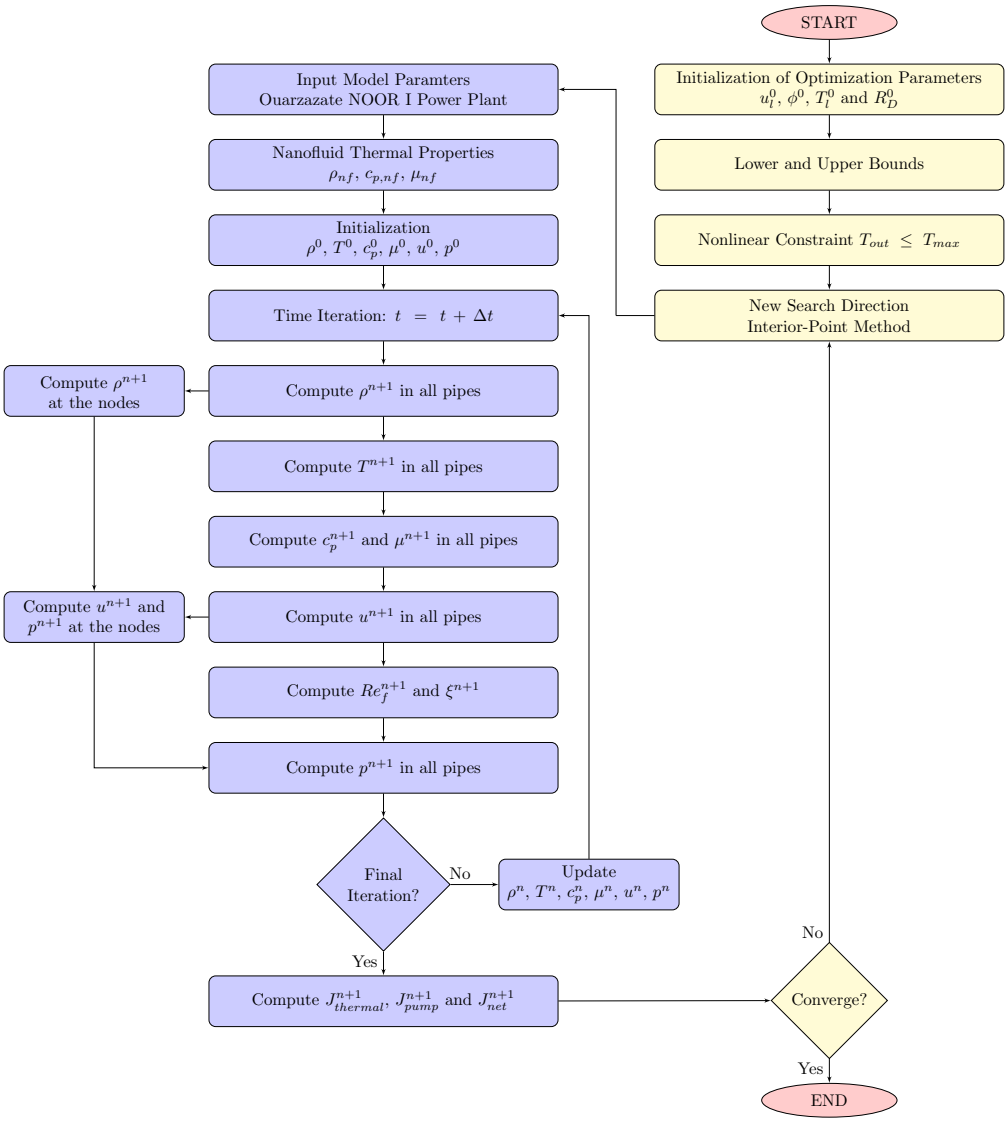

FIG. 3.1: Simulation and optimization algorithm [3].

In the following chapter, the simulation and optimization algorithms are tested, where direct simulation problems on the network system are solved alongside the constrained optimization problems.

Chapter 4

Results and Discussion

In the following chapter, the presented models are simulated for a set of different examples. A number of MATLAB codes are implemented in order to study the different numerical cases.

4.1 PTPP Model Validation: Case of Therminol VP-1

At first, a simple case is considered where the presented model is numerically solved for one single pipe and validated with existing results in literature. Data of the solar radiations and ambient temperature for a typical sunny day in the region of Ouarzazate (Morocco) are considered [38]. The hourly variation of the considered data are plotted in Fig. 1.6 between the sunrise and the sunset, where the observed peak solar radiation is around 1000 W/m^2 and the peak ambient temperature is around 308 K. Some of the coefficients involved in the governing equations are determined using the temperature-dependent properties of the Therminol VP-1 in order to obtain accurate numerical results at each time step. The thermal properties of the HTF for a range of temperatures from 285 K to 693 K are depicted in Fig. 2.1 alongside the linear interpolation expressed in Eqs. 2.1-2.4.

4.1.1 Validation of the single pipe model

To begin with, the plausibility of both models should be examined. As in [1], the first simulation aims to represent a situation as simple as possible, where the analyzed case represents a simple fluid transported through a single pipe from left

to right, then the obtained results obtained are compared with existing results from Allouhi et al. [38]. The same data will always be selected in the subsequent simulation series, including model parameters, calculation parameters, initial, and boundary conditions for the two systems, enabling a comparative analysis. The associated data has been listed in the previous sections.

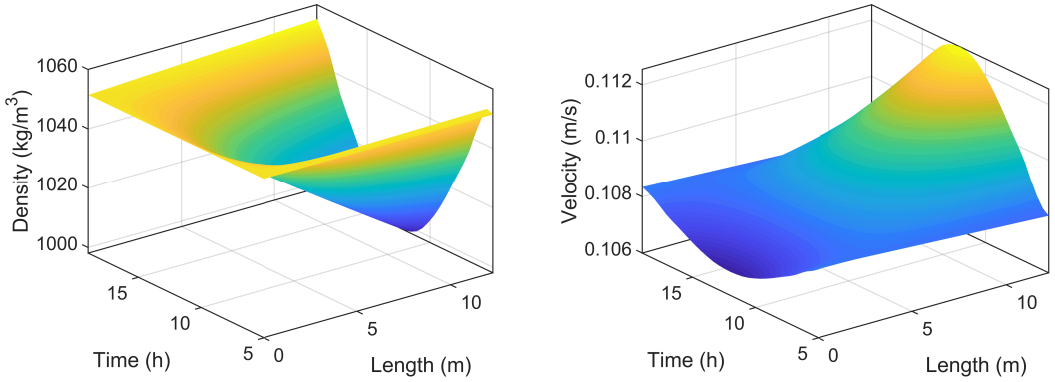

FIG. 4.1: Evolution of the density and velocity in the single pipe model [1].

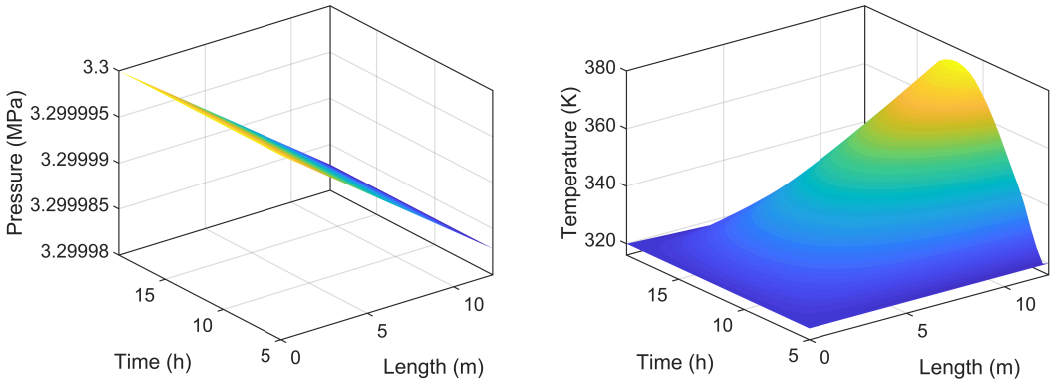

FIG. 4.2: Evolution of the pressure and temperature in the single pipe model [1].

For the case of a single collector pipe, the obtained results are presented to validate the derived model by comparing the predicted temperature variations with

existing values in the literature. The inlet temperature is set at 320 K ($46,85\ ^{\circ}C$). Figs. 4.1-4.2, shows the variation of the obtained results for the fluid properties, namely, the density, velocity, pressure and temperature as function of space (along the pipe) and time (hours of the day).

Based on observations of the different plotted results, when the solar radiation peaks during the day, the minimum value of the density and the maximum values of the velocity and temperature are recorded. Moreover, the collector generates a maximum temperature value ($375\ K$) at the outlet of the pipe when the solar radiation is at the peak value during the day, similar values are obtained in [38] for the same NOOR I model parameters. Compared to other models in the literature and the work of Allouhi *et. Al.* [38], the presented model provides new insight to the spacial and time variation of other fluid properties besides temperatures, such as velocity and density. The additional information can only be generated by a thermo fluid dynamics model, such as the one used in this thesis.

4.1.2 Validation of the network model

In this case, a simple network model constituted of 8 collectors connected in series is assumed, while considering the same model parameters and properties [1]. In order to check the coupling conditions of the system, Eqs. 2.78-2.79, the numerical results for this model can be compared with the results of a one pipe model with the length of 8 collectors ($8 \times 12.27\ m$).

As observed from the results, both systems achieve the same results, see Fig. 4.3. The network model clearly keeps the continuity of the temperature variation from one pipe to another. Similar to the single tube model, the maximum temperature value is at the outlet of the last pipe when the solar radiation reaches the peak value. This can be seen as a basic test for the network approach.

4.1.3 Simulation of Single Pipe Operating with Nanofluids

Adaptive numerical schemes are implemented in the software MATLAB to solve the system of equations 2.48-2.52, [2]. The climatic data of the region of Ouarzazate (Morocco) are considered [38], where the hourly variation of the solar radiation and ambient temperature are shown in Fig. 1.6. Between sunrise and sunset, the observed peak solar radiation is around 1000 W/m^2 and the peak ambient temperature is around 308 K.

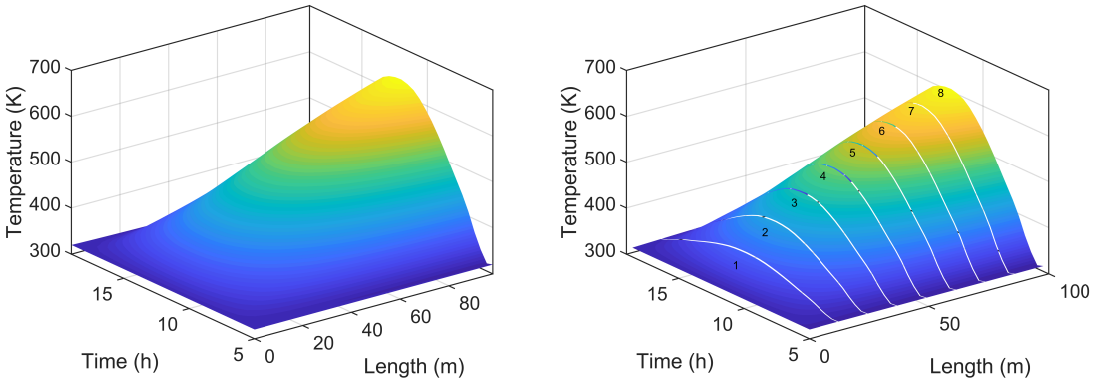

FIG. 4.3: Temperature variation of collectors row using one pipe model (Top) and network model (Bottom) [1].

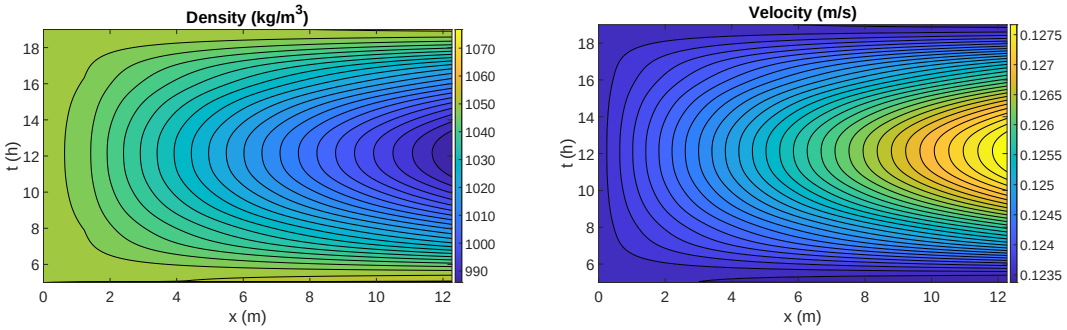

FIG. 4.4: Evolution of the density and velocity for the base fluid Therminol VP-1 [2].

The obtained results are presented to validate the derived model by comparing the predicted temperature variations with existing values in the literature. The inlet temperature is set at 320 K ($46,85\ ^{\circ}C$). Figs. 4.4-4.6, shows the time variation of the obtained results for the fluid properties, namely the density, velocity, pressure, temperature, specific heat capacity and viscosity as function of space (along the pipe) and time (hours of the day). It is noted from the different plotted results that the minimum or maximum values of the different parameters are obtained at the peak value of the solar radiation during the day. Furthermore, the collector generates a maximum temperature of around 380 K at the outlet of

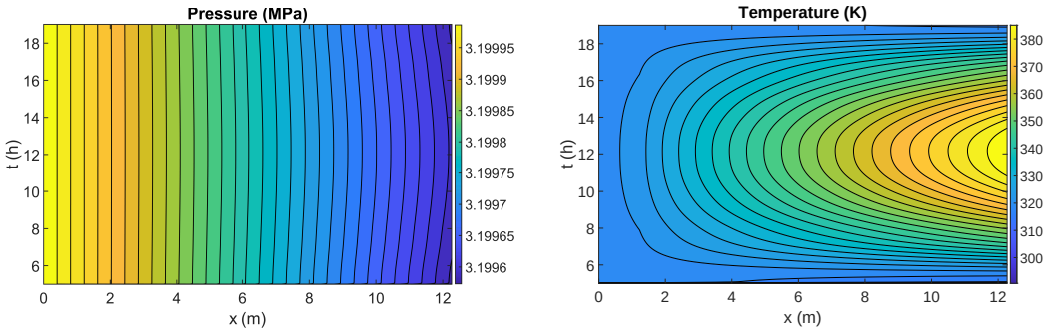

FIG. 4.5: Evolution of pressure and temperature for the base fluid Therminol VP-1 [2].

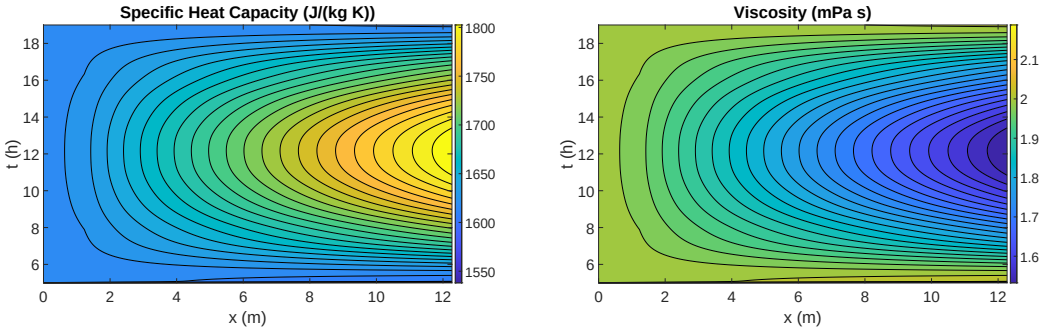

FIG. 4.6: Evolution of specific heat capacity and viscosity for the base fluid Therminol VP-1 [2].

the pipe when the solar radiation is at the peak value during the day. Similar results are shown in Fig. 8 from the work of Allouhi et al. [38], as the maximum temperature of around 375 K is reached at midday. The author used heat equations only to predict the output temperature for the same NOOR I model parameters.

Moreover, the spatial and temporal variations of the Reynolds number and friction factors are obtained and plotted in Fig. 4.7. At the outlet of the collector, it is observed that the Reynolds number reaches the peak value when the solar radiation is at the peak value during the day, while the friction factor is at the lowest value at the same period of time. Thus, the fluid temperatures correlate with the variations of the fluid Reynolds number and friction factor.

The next set of results illustrates the effect of using nanofluids as working

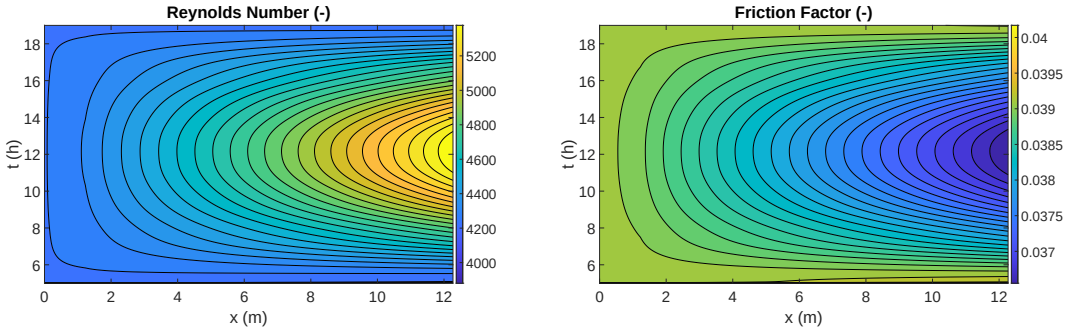

FIG. 4.7: Evolution of Reynolds number and friction factor for the base fluid Therminol VP-1 [2].

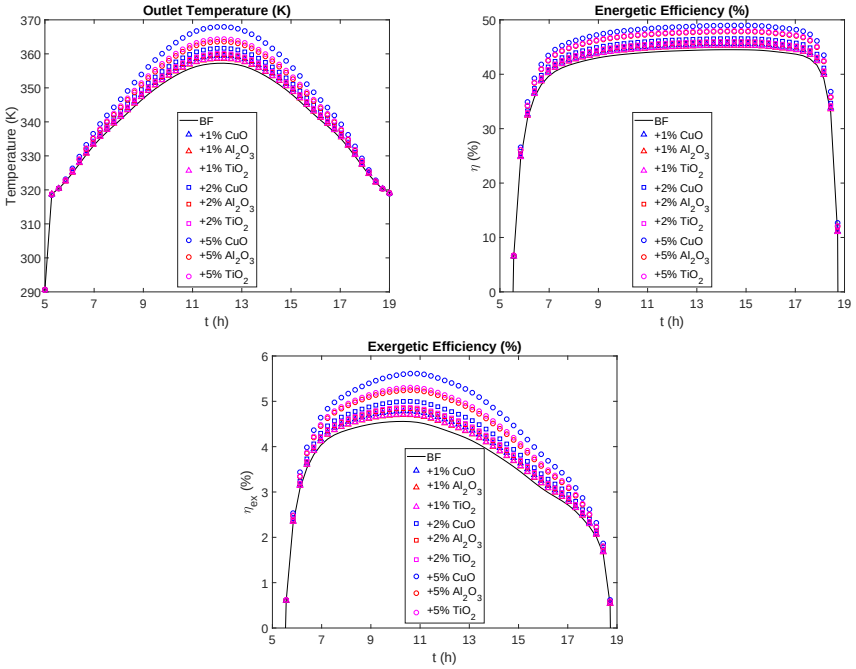

FIG. 4.8: Temporary evolution of outlet temperature, thermal efficiency and exergy efficiency [2].

fluids in the PTC. The same previous operating conditions were considered. The temporary evolution of the outlet temperature, thermal efficiency and exergy

efficiency are depicted in Fig. 4.8. The nanoparticle concentration was set to vary between $\phi \in \{1\%, 2\%, 5\%\}$. It becomes evident that the nanofluids reach higher temperatures than the base fluid, especially at high radiation levels inducing greater heat propagation in the working fluid. The maximal energy efficiency reaches 43% for the base fluid and increases with up to 5% when nanofluids are employed. Due to its high density values, CuO based nanofluid leads to the most significant increase in thermal efficiency, where the maximal exergy efficiency reaches up to 5.5%.

TABLE 4.1: Friction factor with respect to nanoparticles volume fraction [2].

Volume Fraction	1%	2%	5%
Copper Oxide (CuO)	0.036628	0.036710	0.036985
Alumina (Al_2O_3)	0.036704	0.036863	0.037377
Titanium Oxide (TiO_2)	0.036692	0.036838	0.037311

Finally, Table 4.1 presents the variations of the friction factor with respect to the volume fraction of the nanoparticles in the basefluid for three different materials. In contrast to the thermal gain, the presented table demonstrates that with the presence of nanparticles in the base fluid, the friction factor increases with respect to the volume fraction, thus leading to an increase in the friction loss inside the parabolic collector.

4.2 Network-Based Design and Optimization of PTPPs

4.2.1 PTPP Operating with Therminol VP-1

In Series Design of the Collector

NOOR I power plant (Ouarzazate, Morocco) is considered as an application of the presented network model. The network case of 8 pipes connected in series is a realistic case in NOOR I plant, the model can therefore be used for further optimization of the power functional with respect to different model parameters. In this section, the (optimal) pressure drop is the main output of the optimization approach [1].

Iteration	$\Delta P\ (Pa)$	$\max T_{out}\ (K)$	$\tilde{J}_{thermal}\ (MW \cdot h)$	$\tilde{J}_{pump}\ (W \cdot h)$	$\tilde{J}_{net}\ (MW \cdot h)$
1	210.6	693.58	2.62	1.72	2.62
2	280.2	716.17	2.76	2.61	2.76
3	167.7	676.59	2.49	1.23	2.49
4	141.1	664.64	2.38	0.96	2.38
5	124.7	669.65	2.30	0.80	2.30
6	141.6	664.87	2.39	0.96	2.39
7	136.2	663.99	2.36	0.91	2.36
8	131.8	666.12	2.34	0.86	2.34
9	137.6	663.32	2.37	0.92	2.37
10	138.3	663.3	2.37	0.93	2.37
11	138	663.18	2.37	0.93	2.37
12	138	663.15	2.37	0.92	2.37

TABLE 4.2: Iterations to reach the optimal of the net power output satisfying also the upper limit for the temperature; iterations $1-11$ do not satisfy the upper limit. The numbers in red shows the outlet temperatures that exceed the critical value of 663.15 K [1].

For the usual design of each collector row, the pressure drop is optimized to maximize the net power output. Table 4.2 shows the optimization iterations and the associated values of the pressure drop (Δp) and power output (J). It is observed that the maximum output temperature exceeds the critical value of $663.15/K$ $(390/°C)$ in the first 11 iterations, but then finally at iteration 12 it stays below the critical value and subsequently maximizes the generated power under the additional constraint.

Using the optimal value of the pressure drop $\Delta P = 8.53$, the different fluid variables are plotted again with respect to time and space, see Figs. 4.9-4.10. The results show a decrease in the minimum value of density and an increase in both maximum values of the velocity and temperature, especially at the output.

Complex Design of Collector Rows

Usually, collector rows are designed in a series form (Design 1). More complicated designs can be studied with respect to possible better net power output. Thus, three different additional designs are considered as shown in Fig. 4.11 [1]. The

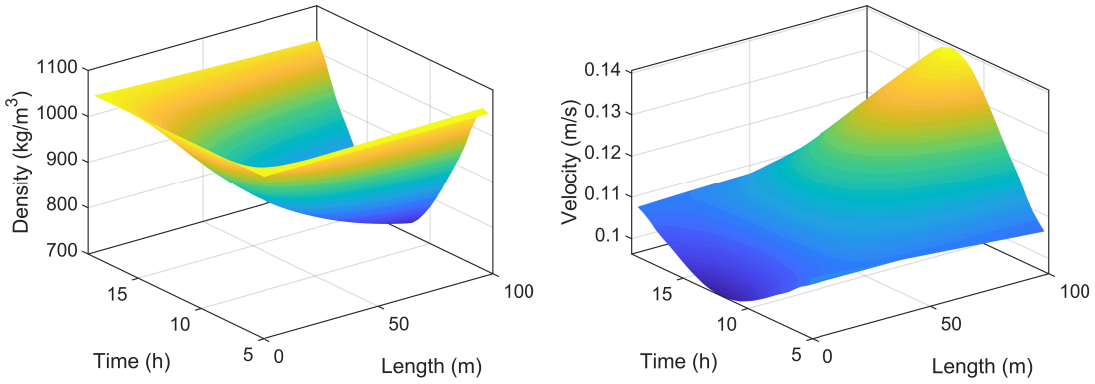

FIG. 4.9: Evolution of the density and velocity for the obtained optimal pressure drop [1].

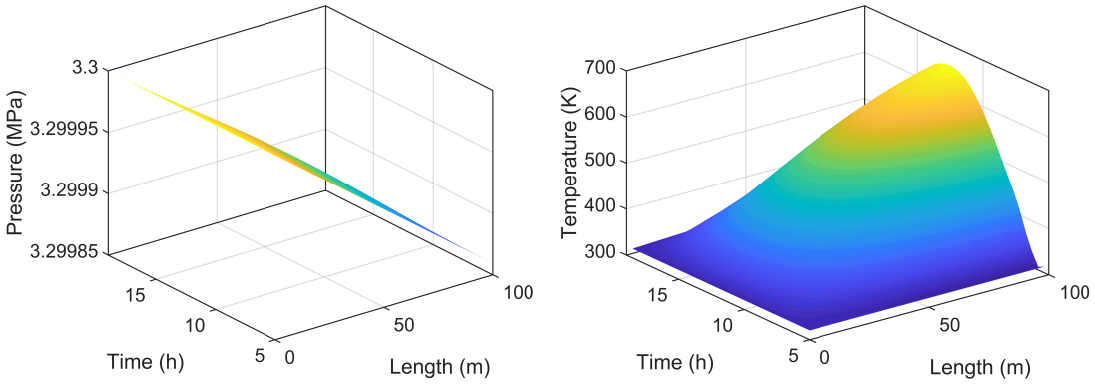

FIG. 4.10: Evolution of the pressure and temperature for the obtained optimal pressure drop [1].

first design (Design 2) consists of two parallel collector pipes at the beginning of the row and the rest are connected in series. The second design (Design 3) consists of two parallel collector pipes at the beginning of the row and another two parallel collector pipes in the middle of the row, while the other pipes are connected in series. The third design (Design 4) consists of six pipes in parallel.

For the four designs, the same optimization approach is used in order to obtain the optimal pressure drop with a maximum net power output. As shown in Table

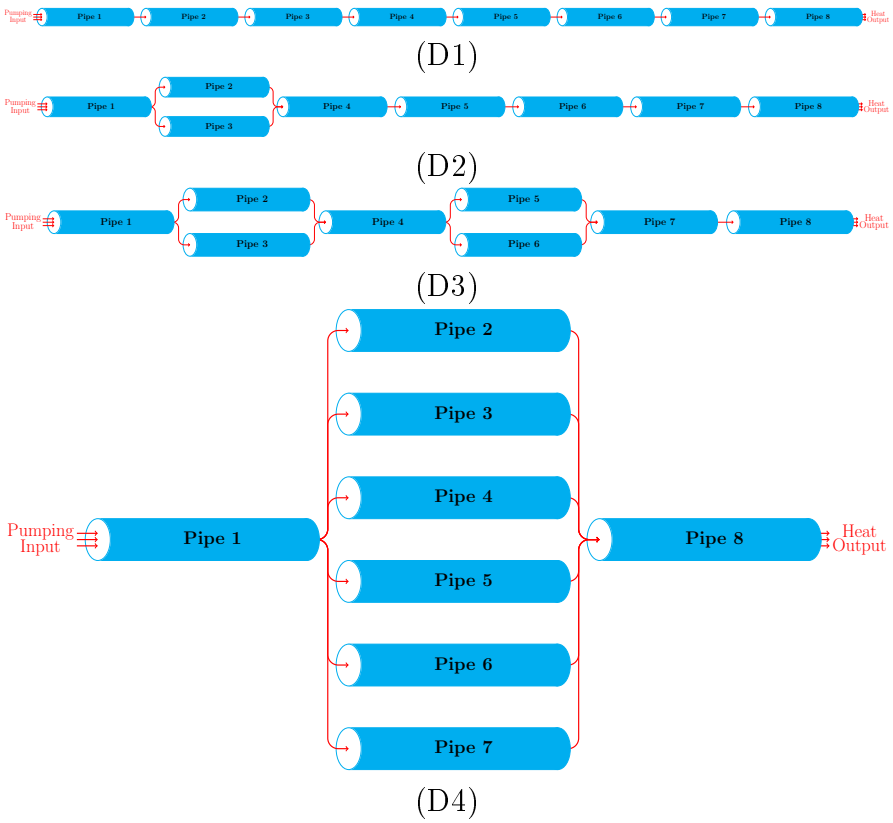

FIG. 4.11: Skitches of the four studied network designs [1].

TABLE 4.3: Optimal pressure drops, thermal, pumping and net power outputs for the different designs [1].

Design	$\Delta P\ (Pa)$	$\max T_{out}\ (K)$	$\tilde{J}_{thermal}\ (MW \cdot h)$	$\tilde{J}_{pump}\ (W \cdot h)$	$\tilde{J}_{net}\ (MW \cdot h)$
1	138	663.15	2.37	0.92	2.37
2	110.3	663.15	2.37	0.74	2.37
3	78.3	663.15	2.37	0.53	2.37
4	33.4	663.15	2.34	0.22	2.34

4.3, the value of the pressure drop varies from one design to another with the minimum value observed for the D4 and the maximum value observed for the classical one d1.

The concluding observation from the obtained results is that a more complex designs of the power plant parabolic trough collectors can result in better output values under better conditions (e.g. lower temperatures). Therefore, further research and studies can be conducted in terms of network design and optimization using simplified models similar to the one introduced in this thesis.

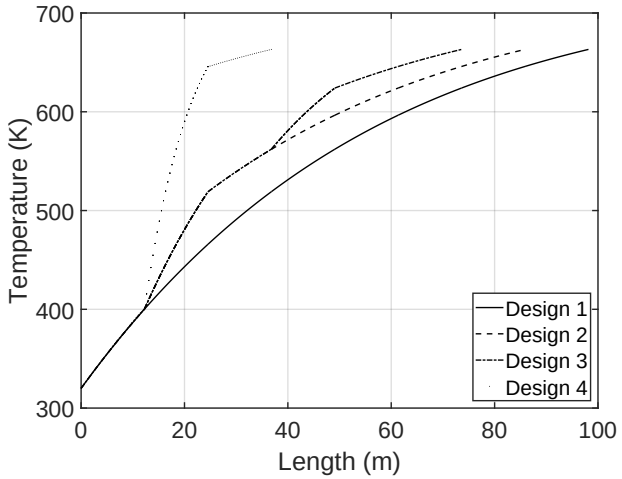

FIG. 4.12: Temperature variation through the collectors row for the different designs [1].

In Fig. 4.12, the fluid temperature variations for the different designs are presented. It is observed that for the parallel pipes, the temperature increases more than for a single pipe, while the output temperature is similar to design 1 with lower pressure drop.

4.2.2 PTPP Operating with Nanofluids

The presented algorithm is implemented in MATLAB. In the following numerical experiments and optimization procedures – in the above explained setting of NOOR I in Morocco – different nanoparticles and with different volume fractions are going to be compared [3].

At first, a direct simulation of a specific case is initiated. The peak of the incident beam radiation at midday is considered with the inlet values of temperature at 300 K, velocity at 1.0 m/s, pressure at 8 MPa (80 bar) and

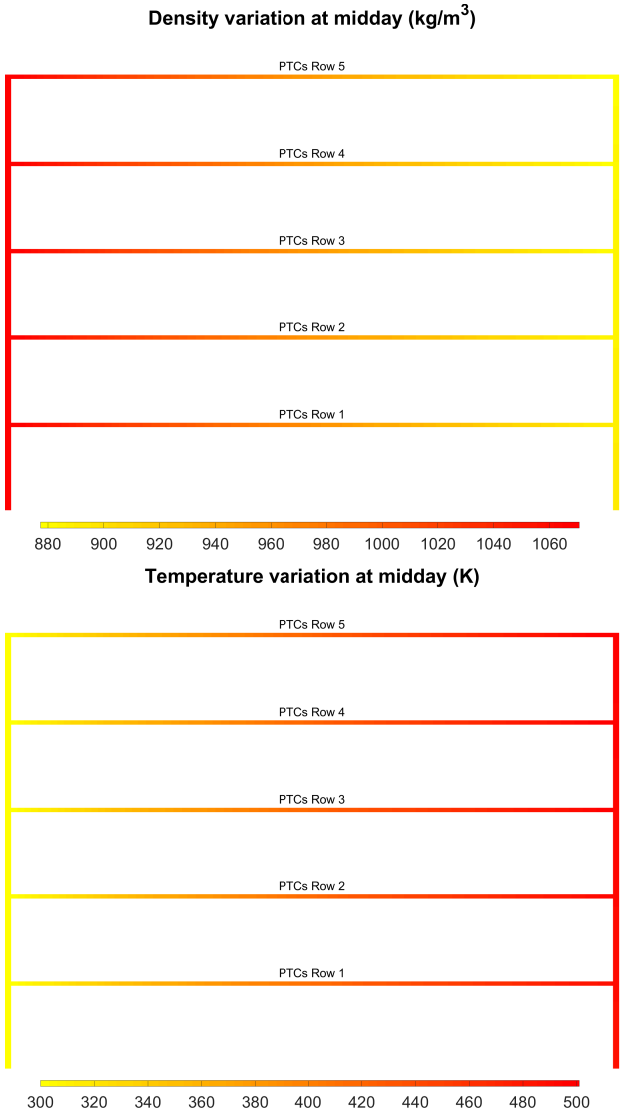

FIG. 4.13: Variations of the density and temperature in the network system [3].

Therminol VP-1 as the HTF. At midday, when the solar radiation reaches its peak, Figs. 4.13-4.15 illustrates the simulation results displaying the distribution of model variables within the network system. The inlet to outlet variation of

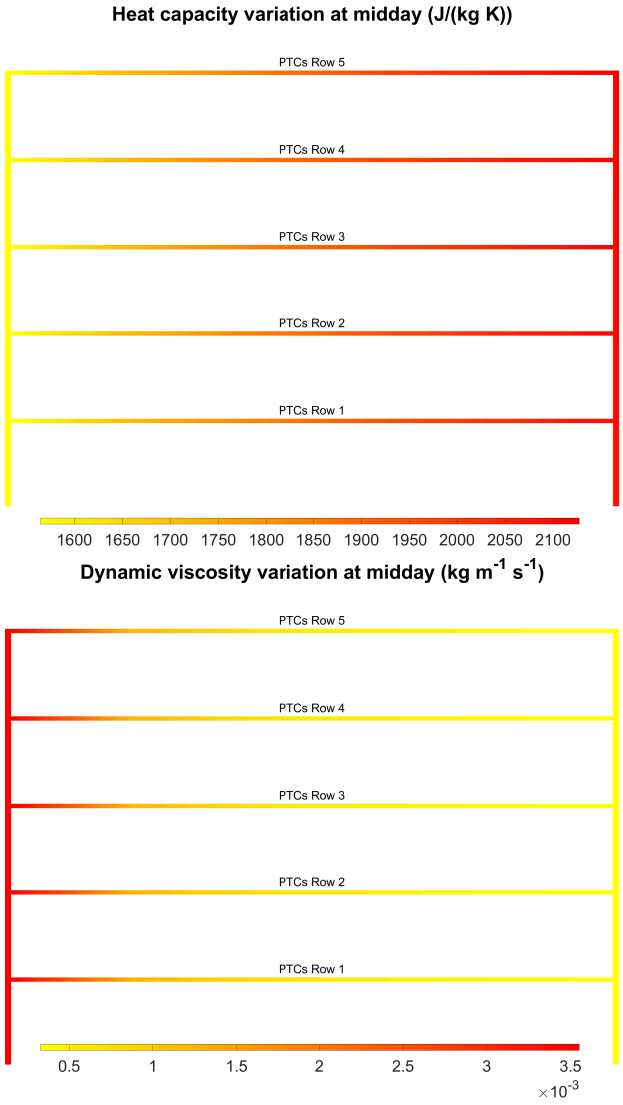

FIG. 4.14: Variations of the specific heat capacity and viscosity in the network system [3].

the dynamic viscosity, density and pressure values shows a decreasing trend. The minimum and peak values observed are as follows: dynamic viscosity ranges from 0.32×10^{-3} to 3.55×10^{-3} $kg/(m\ s)$, density ranges from 877 to 1070 kg/m^3,

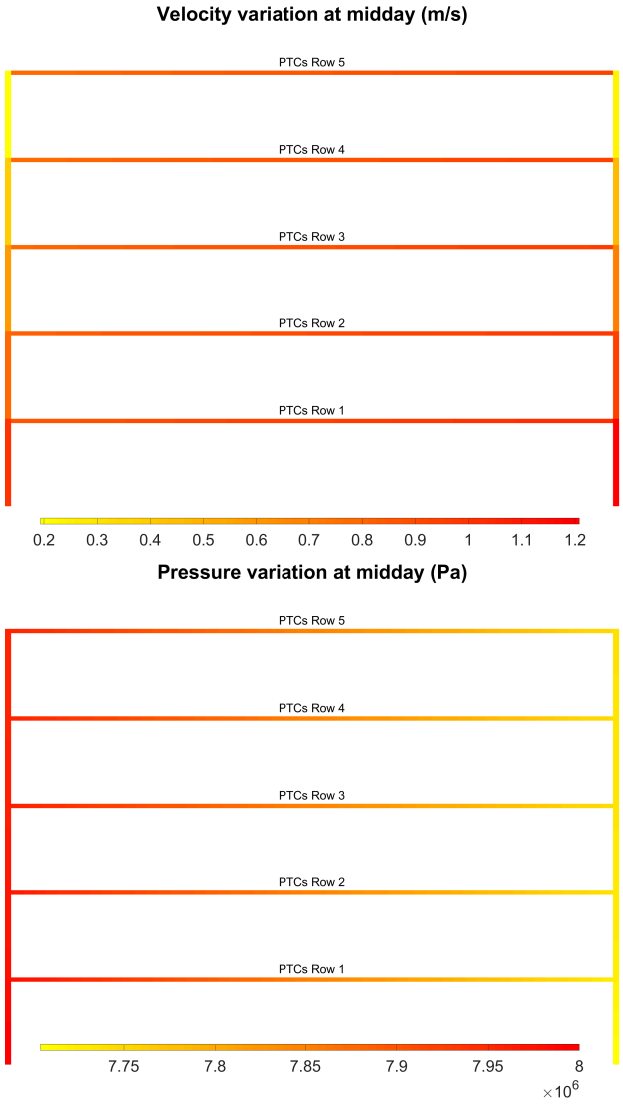

FIG. 4.15: Variations of the velocity and pressure in the network system [3].

and pressure ranges from 7.7 to 8.0 MPa. In contrast, the temperature increases with values between $300 - 501$ K and the specific heat capacity increases with minimum and peak values of $1564 - 2127$ $J/(kg\ K)$. Additionally, the velocity distributions shows a reasonable behavior, being highest close to in- and outlet

and being low before entering and after exiting the last PTC row in the network, with minimum and peak values of $0.19 - 1.20\ m/s$.

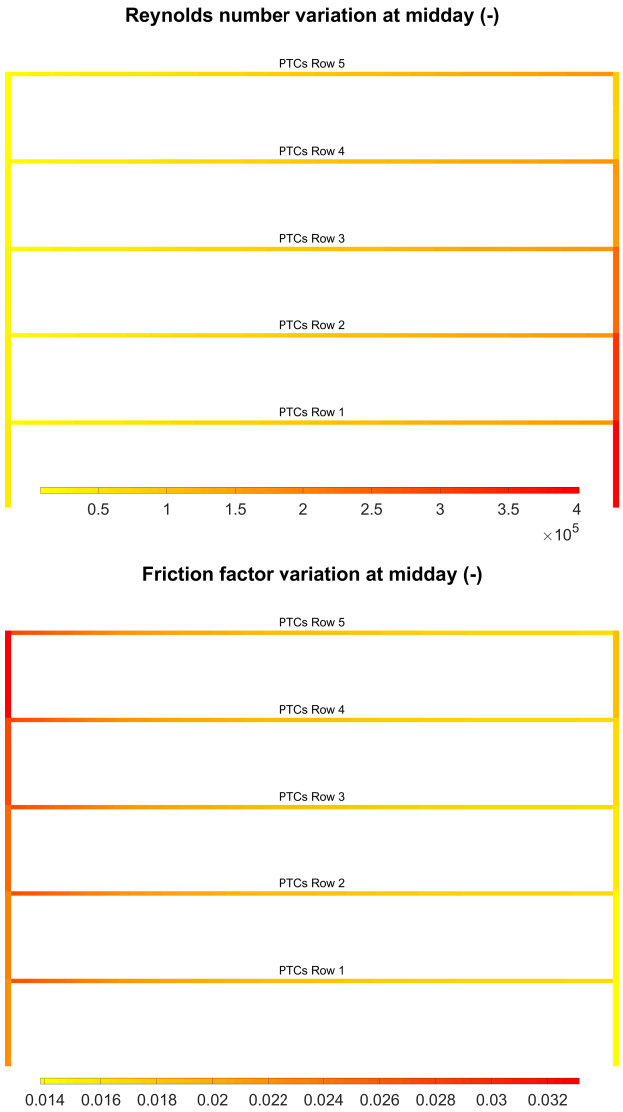

FIG. 4.16: Variations of friction factor and Reynolds number in the network system [3].

Furthermore, the distribution of the friction factor and the Reynolds number

for the same simulation are depicted in Fig.4.16. The Reynolds number is observed to increases in the network system when approaching the outlet of the network, with minimum and peak values of $7.709 \times 10^3 - 4.016 \times 10^5$. On the other hand, friction exhibits an initial increase at the inlet of the PTCs rows, followed by a decrease as the outlet of the network is approached. The minimum and peak values range between 0.013 and 0.033.

In order to narrow the range where the energy output is maximized, experimental parametric studies are performed. To do this, both the generated heat output and the consumed pump energy are considered. The following set of results in the Tables 4.4-4.7 show the effect on the thermal and the pumping energies using nanofluids with variations of nanoparticles types and concentrations by varying one of the following relevant parameters:
in Table 4.4 the inlet velocity is varied, in Table 4.5 the inlet temperature is varied, in Table 4.6 the ratio between the PTC diameter to the inlet/outlet pipe diameter is varied, and finally in Table 4.7 the number of collectors in every row is varied.

In Table 4.4, 48 collectors in every row are considered, the inlet temperature is fixed at $300K$ and the ratio between the PTC diameter to the inlet/outlet pipe diameter is taken as 2. With increasing inlet velocity values the thermal energy output and the pumping energy increase. A small effect of the nanoparticles is seen on the overall energy outputs with some advantage of CuO nanoparticles.

In Table 4.5, 48 PTCs in each collector row are assumed, inlet velocity is fixed at 1 m/s and a ratio between the PTC diameter to the inlet/outlet pipe diameter is taken as 2. The main observation is that increasing the inlet temperature gives a decreasing thermal and pumping energies output. This is due to the lower thermal gain starting by higher temperatures at the inlet of the network system. Again, a small effect of the nanoparticles on the overall energy outputs is observed with some advantage of CuO nanoparticles.

In Table 4.6, the analysis takes into account 48 PTCs in every collector row, with inlet temperature and velocity of $300K$ and 1 m/s, respectively. The diameter ratio strongly affects the output thermal and pumping energies. Increasing the diameter ratio results in increasing energy output. For very high values of the diameter ratios, the consumed pumping energy is higher than the produced thermal energy. This is due to the high friction losses for pipes with smaller diameter. Small effects of the nanoparticles on the overall energy outputs are observed.

TABLE 4.4: Relationship between volume fraction of nanoparticles, inlet velocity, and thermal/pumping energies [3].

HTF	Inlet Velocity (m/s) 0.1		1.0		5.0	
	J_t (MWh)	J_p (kWh)	J_t (MWh)	J_p (kWh)	J_t (MWh)	J_p (MWh)
Therminol VP-1	9.695	0.124	48.034	74.011	61.630	7.157
Basefluid + 1% TiO_2	9.647	0.126	48.735	75.898	62.782	7.355
Basefluid + 2% TiO_2	9.605	0.128	49.399	77.806	63.867	7.555
Basefluid + 5% TiO_2	9.512	0.136	51.210	83.658	66.784	8.167
Basefluid + 1% Al_2O_3	9.662	0.126	48.712	75.772	62.723	7.341
Basefluid + 2% Al_2O_3	9.635	0.128	49.359	77.554	63.759	7.528
Basefluid + 5% Al_2O_3	9.580	0.135	51.144	83.029	66.570	8.098
Basefluid + 1% CuO	9.624	0.127	48.994	76.750	63.215	7.447
Basefluid + 2% CuO	9.567	0.130	49.878	79.510	64.661	7.738
Basefluid + 5% CuO	9.461	0.141	52.181	87.925	68.346	8.624

TABLE 4.5: Relationship between volume fraction of nanoparticles, inlet temperature, and thermal/pumping energies [3].

HTF	Inlet Temperature (K)					
	300		350		400	
	J_t (MWh)	J_p (kWh)	J_t (MWh)	J_p (kWh)	J_t (MWh)	J_p (kWh)
Therminol VP-1	61.938	4.387	42.523	3.658	23.199	3.218
Basefluid + 1% TiO_2	63.109	4.509	43.359	3.767	23.744	3.320
Basefluid + 2% TiO_2	64.212	4.632	44.150	3.876	24.261	3.422
Basefluid + 5% TiO_2	67.172	5.009	46.291	4.209	25.661	3.733
Basefluid + 1% Al_2O_3	63.049	4.501	43.308	3.759	23.701	3.313
Basefluid + 2% Al_2O_3	64.100	4.615	44.055	3.861	24.178	3.408
Basefluid + 5% Al_2O_3	66.950	4.967	46.092	4.171	25.480	3.696
Basefluid + 1% CuO	63.550	4.565	43.678	3.817	23.956	3.368
Basefluid + 2% CuO	65.019	4.745	44.737	3.978	24.651	3.518
Basefluid + 5% CuO	68.756	5.291	47.454	4.462	26.430	3.971

TABLE 4.6: Relationship between volume fraction of nanoparticles, diameter ratio D_{con}/D_{col}, and thermal/pumping energies [3].

HTF	D_{con}/D_{col} (-) 1		5		15	
	J_t (MWh)	J_p (kWh)	J_t (MWh)	J_p (kWh)	J_t (MWh)	J_p (MWh)
Therminol VP-1	24.198	10.219	61.938	4386.844	56.322	757.294
Basefluid + 1% TiO_2	24.313	10.459	63.109	4509.021	57.517	779.128
Basefluid + 2% TiO_2	24.424	10.702	64.212	4632.328	58.637	801.100
Basefluid + 5% TiO_2	24.744	11.452	67.172	5009.051	61.615	867.850
Basefluid + 1% Al_2O_3	24.326	10.442	63.049	4500.566	57.440	777.505
Basefluid + 2% Al_2O_3	24.452	10.669	64.100	4615.423	58.494	797.855
Basefluid + 5% Al_2O_3	24.817	11.369	66.950	4966.775	61.319	859.733
Basefluid + 1% CuO	24.349	10.567	63.550	4565.487	57.971	789.781
Basefluid + 2% CuO	24.494	10.918	65.019	4745.169	59.464	822.386
Basefluid + 5% CuO	24.907	11.998	68.756	5290.908	63.206	920.970

TABLE 4.7: Relationship between volume fraction of nanoparticles, number of collectors in each row, and thermal/pumping energies [3].

HTF	n_c (-) 24		36		48	
	J_t (MWh)	J_p (kWh)	J_t (MWh)	J_p (kWh)	J_t (MWh)	J_p (kWh)
Therminol VP-1	27.416	46.039	38.423	60.151	48.034	74.011
Basefluid + 1% TiO_2	27.877	47.264	39.026	61.715	48.735	75.898
Basefluid + 2% TiO_2	28.313	48.502	39.596	63.297	49.399	77.806
Basefluid + 5% TiO_2	29.494	52.302	41.145	68.148	51.210	83.658
Basefluid + 1% Al_2O_3	27.857	47.183	39.003	61.611	48.712	75.772
Basefluid + 2% Al_2O_3	28.277	48.341	39.555	63.089	49.359	77.554
Basefluid + 5% Al_2O_3	29.426	51.897	41.073	67.630	51.144	83.029
Basefluid + 1% CuO	28.049	47.811	39.250	62.418	48.994	76.750
Basefluid + 2% CuO	28.630	49.597	40.009	64.702	49.878	79.510
Basefluid + 5% CuO	30.127	55.039	41.977	71.666	52.181	87.925

TABLE 4.8: Optimal values of various system parameters with respect to the number of collectors in every network row [3].

Parameter	Number of Collectors			
	12	24	36	48
J_{net} (MWh)	8.95	19.35	29.54	39.51
$J_{thermal}$ (MWh)	8.95	19.39	29.69	39.89
J_{pump} (kWh)	2.08	35.43	157.24	380.20
T^{out}_{max} (K)	467.86	471.78	473.66	475.16
T_{avg} (K)	375.00	375.00	375.00	375.00
u_l (m/s)	0.50	1.42	2.39	3.14
φ (%)	5.00	5.00	5.00	5.00
T_l (K)	300.00	300.00	300.00	300.00
D_{con}/D_{col} (-)	1.38	1.21	1.15	1.17

TABLE 4.9: Optimal values of various system parameters with respect to the type of added nanoparticles [3].

Parameter	Nanoparticles			
	None	CuO	Al_2O_3	TiO_2
J_{net} (MWh)	34.87	39.51	38.23	38.40
$J_{thermal}$ (MWh)	35.15	39.89	38.58	38.75
J_{pump} (kWh)	281.31	380.20	346.95	354.13
T^{out}_{max} (K)	475.01	475.16	475.10	475.11
T_{avg} (K)	375.00	375.00	375.00	375.00
u_l (m/s)	3.07	3.14	3.14	3.14
φ (%)	0.00	5.00	5.00	5.00
T_l (K)	300.00	300.00	300.00	300.00
D_{con}/D_{col} (-)	1.13	1.17	1.15	1.16

In Table 4.7 the inlet velocity is fixed at 1 m/s, the inlet temperature at 300 K and the ratio between the PTC diameter to the inlet/outlet pipe diameter at 2. It is clear that increasing the number of collectors in every row directly leads to a higher energy output as the HTF absorbs more heat from solar radiation. An effect of nanoparticles addition is also observed.

From the results of the parameter experiments, the energy output is concluded

to be significantly affected by small variations of inlet temperature and inlet velocity which was also observed for the case of a single PTC tube [38, 50]. Furthermore, the slight improvement by the nanofluid addition is in good agreement with the findings of Allouhi et al. [38]. In addition, in the case of a network system, the difference between the diameter of the PTCs and the diameter of the connecting pipes can greatly affect the thermal efficiency of the PTPP. Moreover, the number of PTCs in every row of the network system also influences the thermal and pumping energies. Therefore, an optimization process using a selected combination of design parameters promises more efficient operation results.

In order to test and document the optimization algorithm as a whole, two optimization problems are considered. In both cases, the 5-collector row model with a certain number of collectors in every row coupled in series is considered (as above). Tables 4.8 and 4.9 show the optimization results for the two different optimization approaches.

The first optimization problem considers different numbers of collectors in each row. Optimization is done simultaneously with respect to 4 parameters, the inlet velocity, u_l, the nanoparticles volume fraction, φ, the inlet temperature, T_l, and the ratio of inlet/outlet pipe diameter to the collector pipe diameter, r_D. The algorithm starts with an inlet temperature 320 K, inlet velocity at 1.0 m/s, volume fraction of nanoparticles at 1% and diameter ratio at 5. The algorithm terminates after a certain number of steps for the different problem settings.

Table 4.8 shows the obtained optimal input parameters to maximize the energy output for different numbers of PTCs in each row of collectors. It is observed that the maximal energy output is obtained when the inlet temperature is at the lowest value at 300 K, as predicted from Table 4.5. Similarly, the optimal value of the volume fraction of nano particles is predicted to take the maximum possible value of 5%. The optimal values of the inlet temperature and the volume fraction stay fixed for different numbers of collectors. On the other hand, the optimal value of the inlet velocity exceeds the extremes of the proposed limits from the examples of the previous section. It tends to increases significantly with respect to increasing number of collectors. In contrast, the optimal value of the diameter ratio slightly decreases when increasing the number of collectors.

For the second optimization problem, different types of nanofluids are considered, once again with respect to the four parameters mentioned above.

Table 4.9 shows the obtained optimal input parameters to maximize the energy output using the different proposed nanofluids and base fluid. Similarly to Table 4.8, the maximal energy output is obtained when the inlet temperature is at the lowest value of 300 K and the maximum possible value of the volume fraction 5% for all types of nanoparticles. On the other hand, the optimal values of the inlet velocity and the diameter ratio slightly change when using different nanofluids. The optimal value of the inlet velocity is slightly higher when using nanofluids than base fluid. Moreover, the maximal value of the diameter ratio is obtained when using CuO nanoparticles.

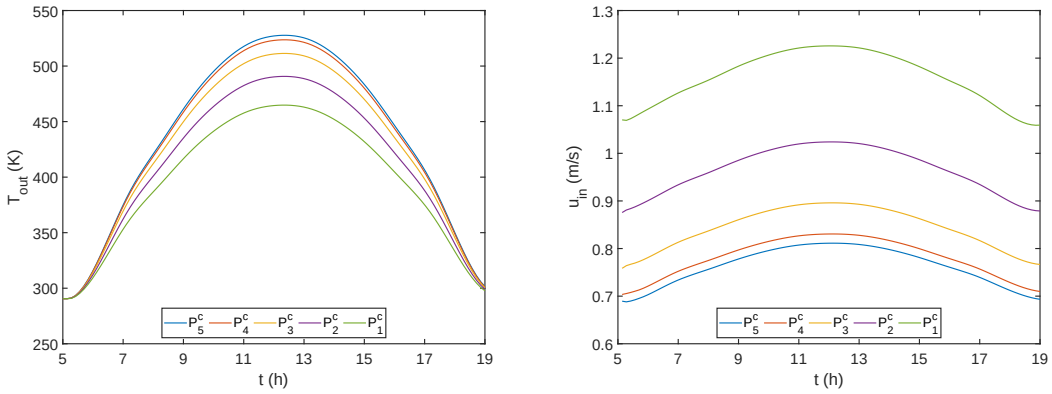

FIG. 4.17: Outlet temperature (left) and inlet velocity (right) variations in parallel collector rows with respect to time [3].

Finally, using the obtained optimal values, the outlet temperature and inlet velocity of each row of PTCs are depicted in Fig.4.17. It is observed that the outlet temperature from the parallel rows increases when moving from collector rows closer to the inlet pipe to the ones farther away. In contrast, the inlet velocity to the parallel rows are shown to be decreasing when moving from the lower collector rows to the upper ones. It is possible to conclude that due to the decrease in the inlet velocity from row to row, the nanofluid has more time to absorb heat from solar radiation. In addition, the decrease in the inlet velocity is due to the pressure drop in the inlet connecting pipes between the rows.

The presented results suggest that the various system parameters and conditions significantly affect the efficiency of the PTC and PTPP in general.

Thus, the coupling between network numerical modeling and optimization guarantees the selection of efficient combinations of design parameters.

4.2.3 PTPP Operating with molten salt

To solve the system of equations 2.65-2.69 for each individual parabolic collector tube, a finite difference method is employed in both space and time. At the beginning time, $t = 0$, the fluid temperature within each tube is assumed to be equal to the ambient temperature. In terms of boundary conditions, the inlet temperature, velocity, and pressure are specified. Moreover, a semi-implicit scheme is adopted to solve the density equation, Eq. 2.65. Using a trapezoidal numerical integration method, the velocity is computed by integrating Eq. 2.67. The nonlinear system of network equations, Eqs. 2.78-2.79, is numerically solved to obtain the values of the velocities and pressures at the network nodes. Subsequently, the pressure values are obtained by utilizing a backward finite difference scheme to solve Eq. 2.66 [4].

Figs. 4.18-4.20 illustrates the simulation outcomes for various quantities at every point in the network during midday when the incident beam radiation reaches its peak, the HTF used is molten salt with an inlet velocity of 1.0 m/s, inlet temperature of 623.15 K, and inlet pressure of 8 MPa (80 bar). The density, dynamic viscosity, and pressure values decrease from the inlet to the outlet, ranging from $1850 - 1880$ kg/m^3, $2.79 \times 10^{-3} - 3.46 \times 10^{-3}$ $kg/(m\ s)$, and $4.98 - 8.00 MPa$, respectively. On the other hand, the temperature and specific heat capacity values increase, ranging from $613.22 - 653.12$ K and $1386.91 - 1355.76$ $J/(kg\ K)$, respectively. Additionally, Fig. 4.21 shows the distribution of Reynolds number and friction factor. The Reynolds number increases towards the outlet of the network, ranging from $3.96 \times 10^4 - 1.52 \times 10^5$, while the friction factor initially increases at the PTCs inlet rows but decreases towards the outlet of the network, with a range of $0.017 - 0.022$.

4.3 PTPP Models Comparison: Case of molten salt

The presented models in the following section are simulated and compared for different situations. In the first subsection, the case of a single pipe is examined,

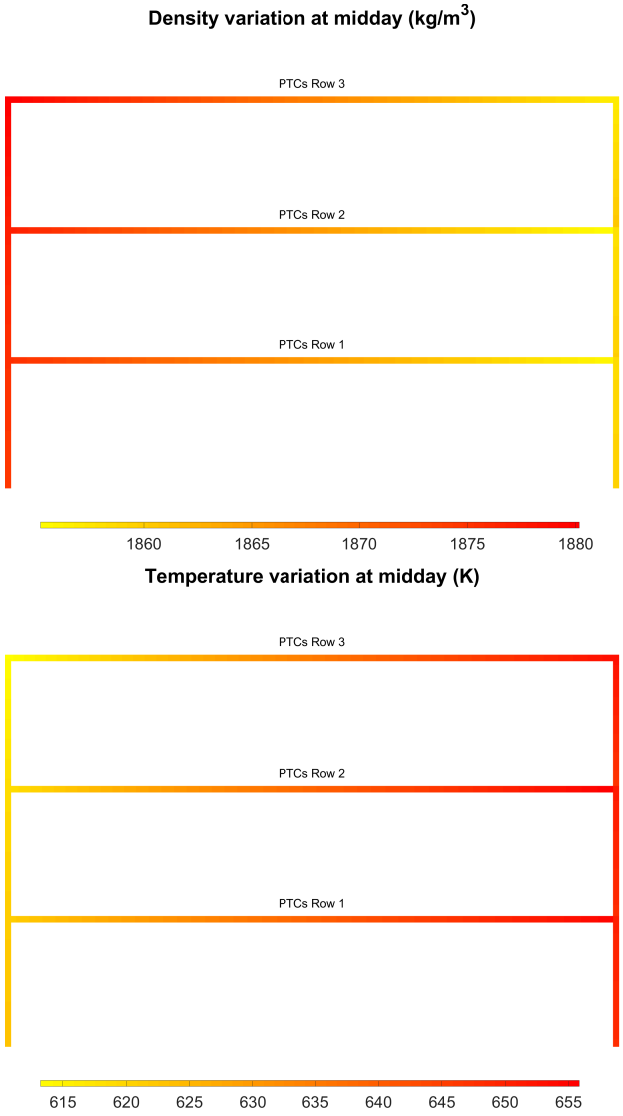

FIG. 4.18: Distribution of the density and temperature in the network pipes model [4].

while in the second subsection, the models are compared for the case of PTCs connected in series and the case of a very large network as an application to the real solar field of NOOR I station in Ouarzazate, Morocco. In each case study,

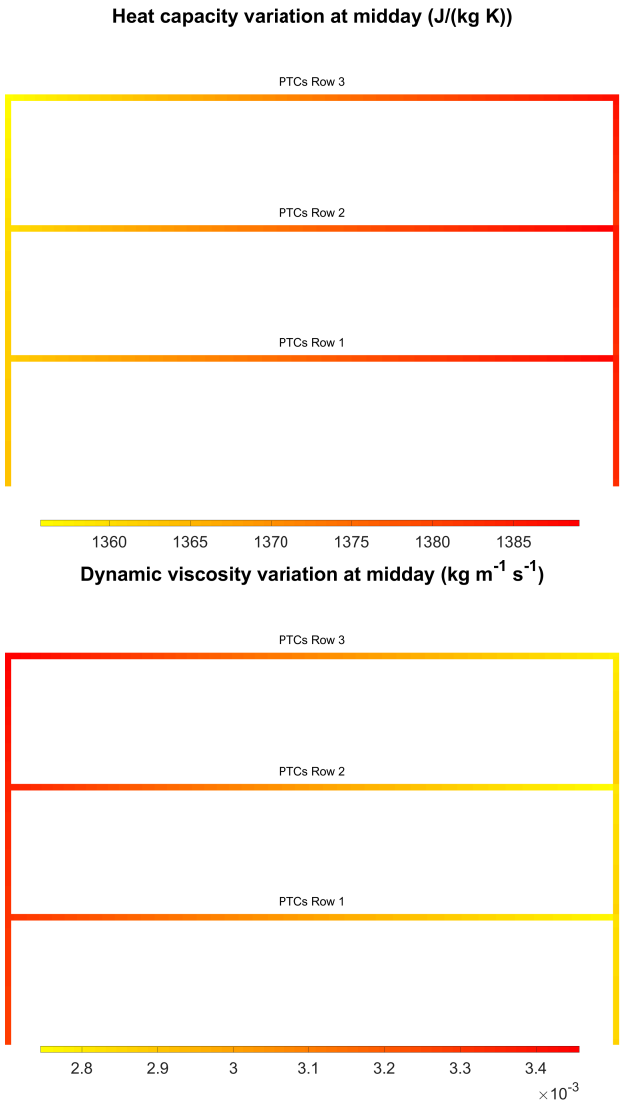

FIG. 4.19: Distribution of the specific heat capacity and viscosity in the network pipes model [4].

the simulation run time is computed for different time and space discritization in order to compare the computation costs for each model.

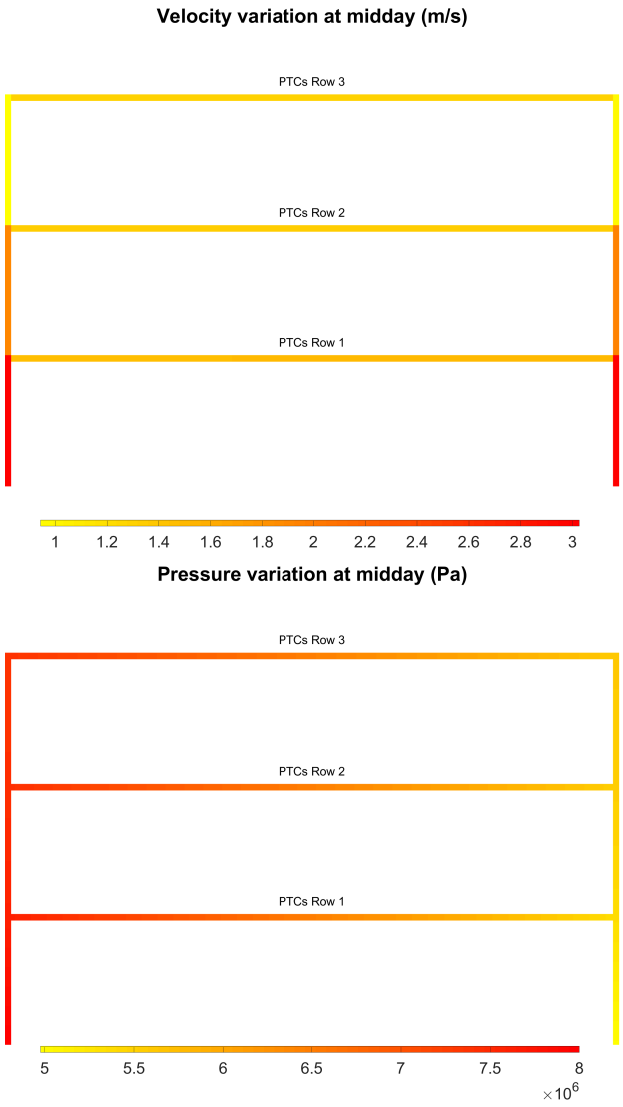

FIG. 4.20: Distribution of the velocity and pressure in the network pipes model [4].

4.3.1 Comparison of Single Pipe Models

In what follows, the case of a single pipe is assumed with the collector length being $L = 147.24$ m. The various models presented in chapter 2 are implemented

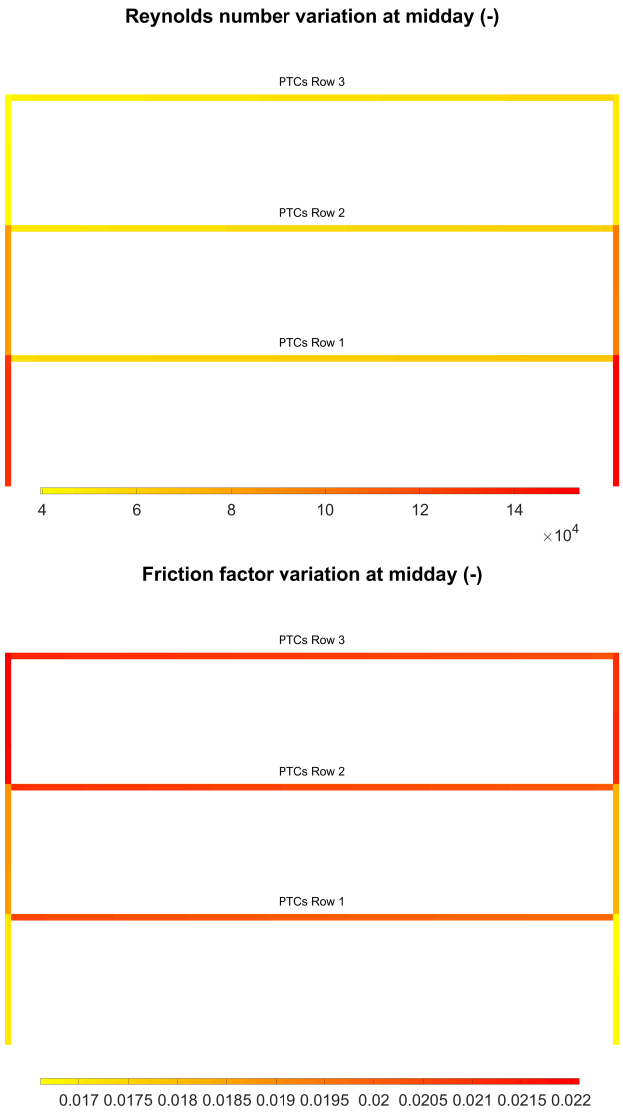

FIG. 4.21: Distribution of the Reynolds number and friction factor in the network pipes model [4].

in MATLAB to simulate the system quantities: temperature, density, specific heat capacity, velocity, viscosity and pressure. The models are referred to using numbers: model 1 refers to the one presented in section 2.3.1, model 2 to that in

section 2.3.2, model 3 to that in section 2.4.1, and model 4 to the one in section 2.4.1.

The time-space discretization involves 50 space subdivisions and 1000 time subdivisions. In order to obtain the inlet velocity, mass flow rate in the system is fixed at 3 kg/s. molten salt is used as the HTF in this case, where the fluid thermal properties are introduced in section 2.2.3 with associated types of fitting used in the numerical implementation. Figs. 4.22-4.31 depict the obtained numerical results, where the time variation of the selected quantities at the outlet of the pipe and space variation during the zenith of the solar radiation are shown for models 1-4.

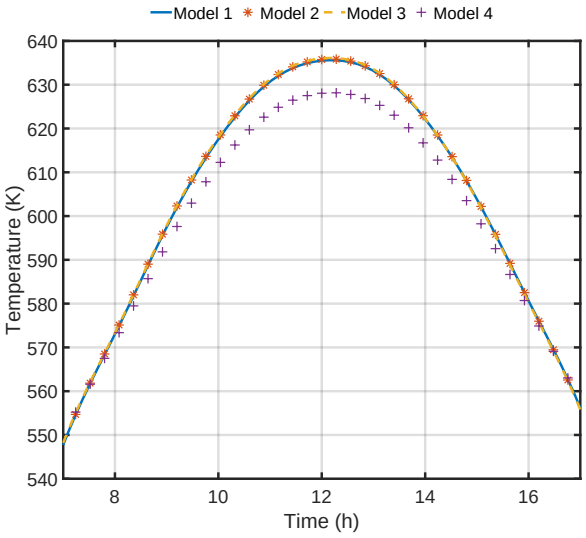

FIG. 4.22: Comparison of hourly variation of the outlet temperature.

According to Fig. 4.22, the outlet temperature for all models appears to increases until it reaches the maximum value at midday when the solar radiation at the peak and then it starts to decrease. While Fig. 4.23 shows that the temperature has a linear profile with respect to the pipe length for space-dependent models 1 and 3. The obtained temperature values using models 1-3 are in great agreement, with a maximum value close to 635 K, while the resulting temperature from model 4 reaches a maximum value of 628 K. This is due to the fact that model 4 is just a two point space-discretization of model 3 which causes this small inaccuracy of the results.

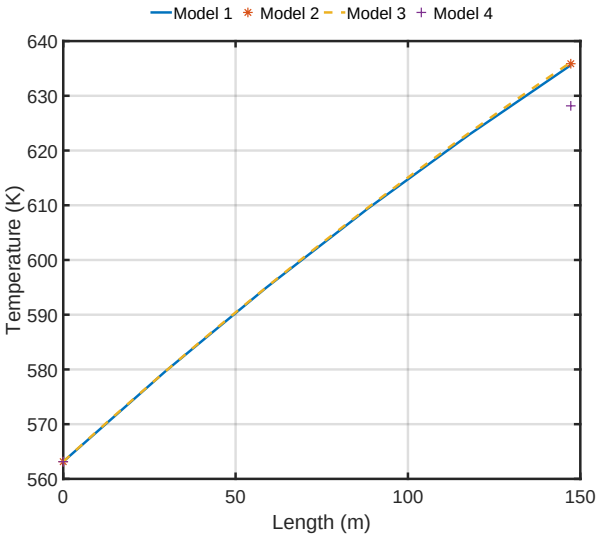

FIG. 4.23: Comparison of the temperature variation with respect to the pipe length.

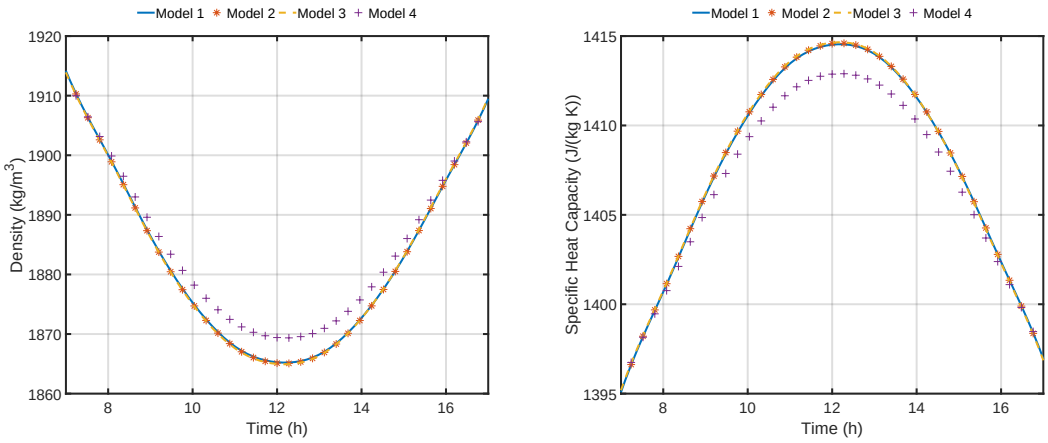

FIG. 4.24: Comparison of hourly variation of the outlet density and specific heat capacity

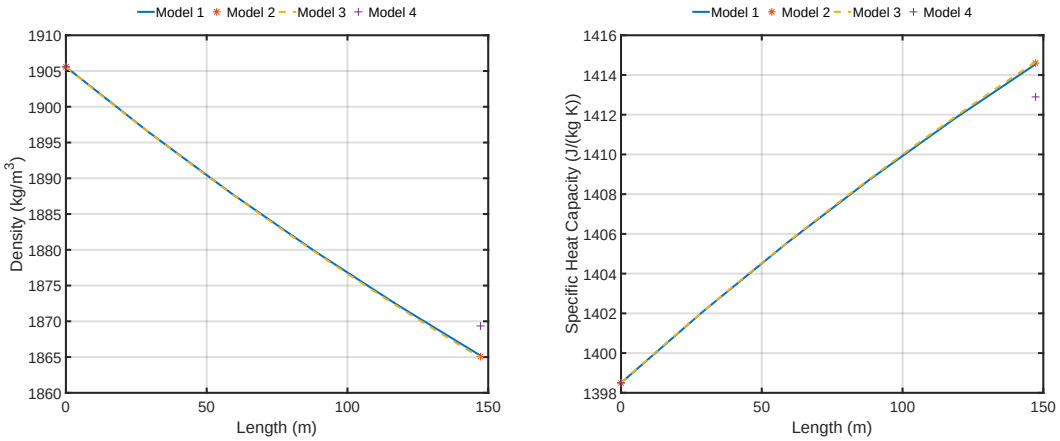

FIG. 4.25: Comparison of the density and specific heat capacity variations with respect to the pipe length

The obtained time variations of the density and specific heat capacity for models 1-4 are shown in Fig. 4.24. As expected from previous numerical results, it is apparent that the outlet density decreases when the temperature increases, and it reaches the minimum value when the solar radiation peaks at midday, then it starts to increase afterwards. On the other hand, the specific heat capacity increases when the temperature increases, and it reaches the maximum value when the solar radiation peaks at midday, then it starts to decreases afterwards. While Fig. 4.25 shows that the density and specific heat capacity also have almost linear profiles with respect to the pipe length for space-dependent models 1 and 3. Similarly to the previous observations, models 1-3 results are in good agreements with a minimum density close to 1942 kg/m^3 and a maximum specific heat capacity close to 1414 J/(kg K), while model 4 produces a little inaccuracy in the results, where the minimum density is close to 1936 kg/m^3 and the maximum specific heat capacity is close to 1413 J/(kg K).

Regarding the velocity, Fig. 4.26 shows the time variations at the outlet for models 1-4. The velocity is assumed to be constant for model 3-4 as displayed in the figure, and it takes the inlet value. While Fig. 4.27 shows that the velocity profile with respect to the pipe length is also linear for space-dependent models 1 and 3. On the other hand, it is clearly evident that the velocity variations obtained

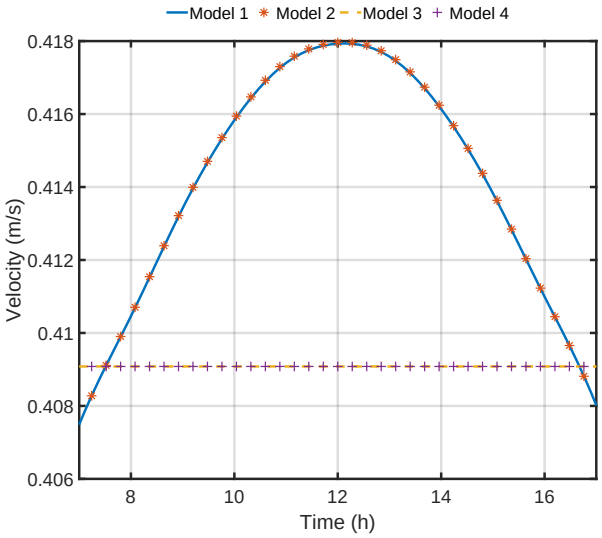

FIG. 4.26: Comparison of hourly variation of the outlet velocity

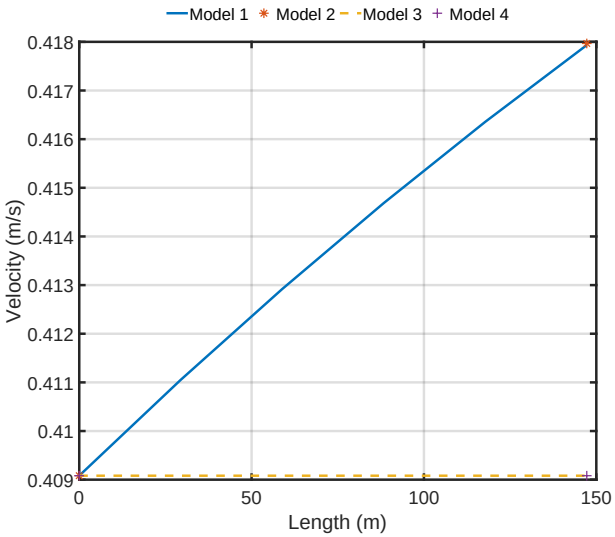

FIG. 4.27: Comparison of the velocity variation with respect to the pipe length

from model 1-2 are very small with an order of difference close to 10^{-2} which does not affect the variation of other quantities, thus explaining the good agreements between the models 1-2 and model 3.

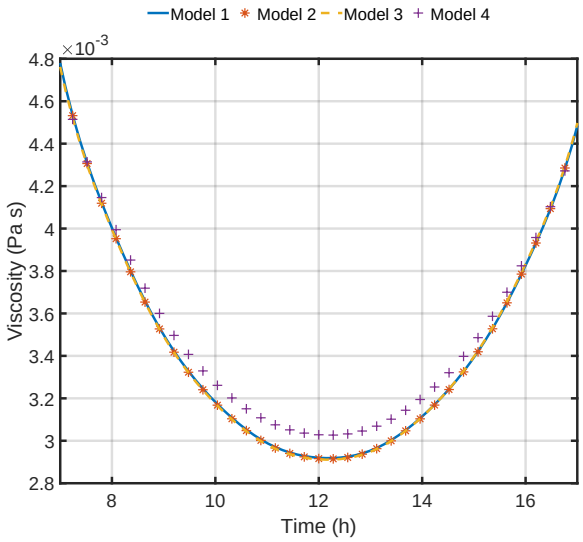

FIG. 4.28: Comparison of hourly variation of the outlet viscosity

Fig. 4.28 shows the viscosity time variations for all models, where similar observation can be made as the outlet viscosity decreases when the temperature increases, reaching the minimum value also at midday. While Fig. 4.29 shows that the viscosity profile with respect to the pipe length has a decreasing exponential form for space-dependent models 1 and 3. The model 1-3 also produce very close results with the minimum viscosity being 7.5×10^{-3} Pa s while model 4 lacks good accuracy in term of the viscosity's minimum value (6.8×10^{-3} Pa s).

The pressure variations for the proposed models are depicted in Fig. 4.30. While Fig. 4.31 shows that the pressure profile with respect to the pipe length has an almost linear form for space-dependent models 1 and 3. The outlet values do not appear to be in a good agreement when comparing the different models. Due to fact that the pressure drop in the pipe is very small in general, the effect of the small differences in velocity on the outlet pressure can be clearly seen between the models 1-4.

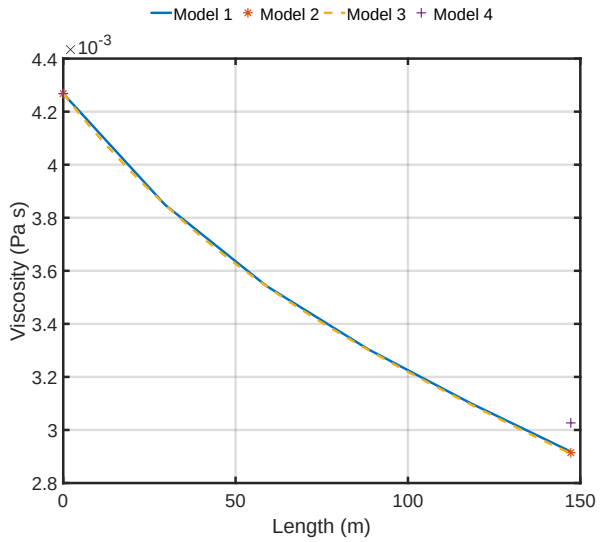

FIG. 4.29: Comparison of the viscosity variation with respect to the pipe length

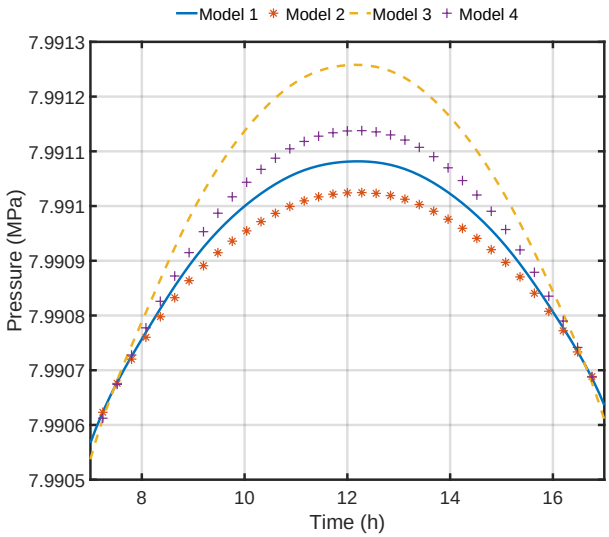

FIG. 4.30: Comparison of hourly variation of the outlet pressure

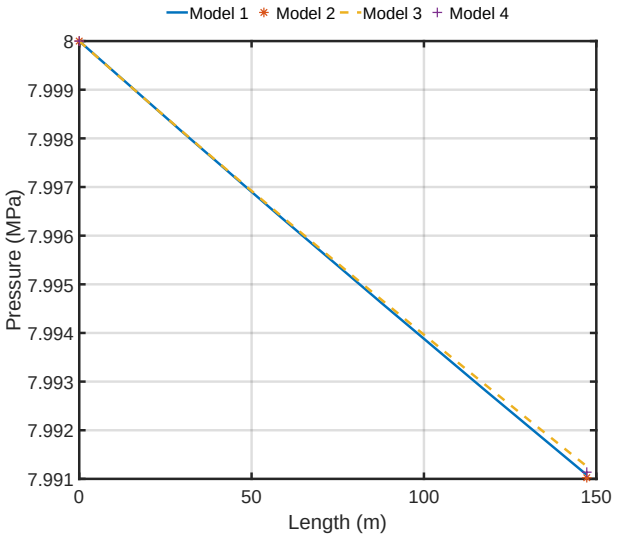

FIG. 4.31: Comparison of the pressure variation with respect to the pipe length

Model	n_x	n_t	Runtime (s)
1	10	1000	4.916922
	20	1000	7.387119
	50	1000	15.184458
2	-	1000	2.622933
3	10	1000	0.417267
	20	1000	0.423145
	50	1000	0.452751
4	-	1000	0.355986

TABLE 4.10: Models comparison with respect to MATLAB runtime.

Finally, the computation run times for each model were compared for different number of space discretization points, as shown in Table 4.10. It is clearly demonstrated that model 3 and it space-independent version (model 4) run much quicker and save great amount of time in the case of single pipe simulation. While the first model takes almost 30 times (30x) more time to produce the results for the case of 50 space grid points, which will have a great effect on the simulation

time of very large network model as will be discussed later.

The proposed simplified models 2-4 are now examined and compared with fully developed model 1, where the obtained results are promising and allow the integration of such models in network modeling of PTPPs. In the following section, the models are compared for different cases of network systems, then the numerical results of the application to the real solar field of NOOR I station are presented.

4.3.2 Comparison of Network Models

The solar field of the NOOR I station has a total of 400 rows; each row has 4 collectors. In what follows, the case of a single row is assumed where 4 PTCs are connected in series, with each collector having a length of $L = 147.24$ m. The various network models presented in chapter 2 are implemented in MATLAB with no interest in the pressure but only the simulation of the following system quantities: temperature, density, specific heat capacity, and velocity. The same reference is kept for the network models, where network models 1-2 refer to the ones presented in section 2.3.3 and models 3-4 to the ones in section 2.4.3.

Single PTCs Row Connected in Series

FIG. 4.32

In the case of a single row of 4 PTCs, as shown in Fig. 4.32, the time-space discretization involves 50 space subdivisions and 1000 time subdivisions, as the molten salt is also retained as the HTF in this case. Figs. 4.33-4.38 depict the obtained numerical results, where the time variation of the selected quantities at the outlet of the pipe and space variation during the peak of the solar radiation are shown for models 1-4.

From Fig. 4.33, the outlet temperature for all models appears to behave in similar way to the single pipe model but the temperature increases way higher until it reaches the maximum value when the solar radiation peaks at midday, and then it starts to decrease. While Fig. 4.34 shows that the temperature over all connected pipes has a parabolic profile rather than a linear one and that the profiles are continuous with respect to the connected pipes, which validate the

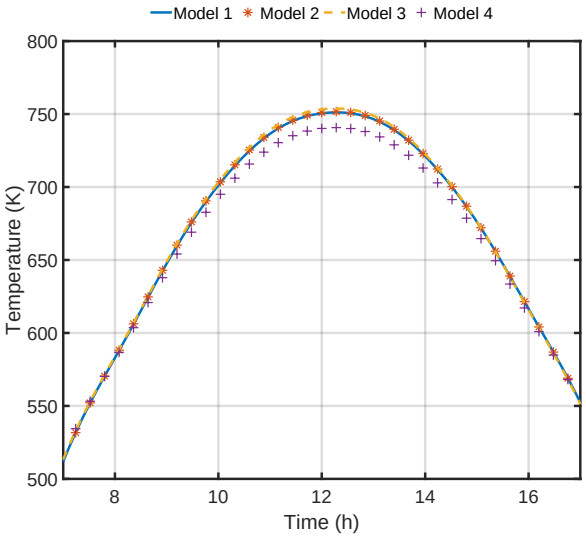

FIG. 4.33: Comparison of hourly variation of the network outlet temperature.

proposed coupling conditions. The obtained temperature values using models 1-3 are in very good agreement, with a maximum value being approximately 751 K, while the resulting temperature from model 4 reaches a maximum value of 740 K. This is also due to the low accuracy of model 4, as explained previously.

The obtained time variations of the density and specific heat capacity for models 1-4 are shown in Fig. 4.35. Similar behavior is observed in comparison to the previous numerical results of single pipe models. While Fig. 4.36 shows that the density and specific heat capacity also have almost parabolic and also continuous profiles with respect to the row length. Similarly to previous observations, models 1-3 results are in good agreements, with a minimum density (maximum specific heat capacity) close to 2001 kg/m^3 (1440 J/(kg K)), while model 4 produces a little inaccurate results, with a minimum density (maximum specific heat capacity) of approximately 1992 kg/m^3 (1438 J/(kg K)).

Regarding the velocity, Fig. 4.37 shows the time variations at the outlet for network models 1-4. The velocity is assumed to be constant for model 3-4 as shown in the figure; it takes the inlet value while maintaining the same value when moving from one pipe to another. While Fig. 4.38 shows the continuous velocity profiles with respect to the row length; they take a parabolic form for space-dependent

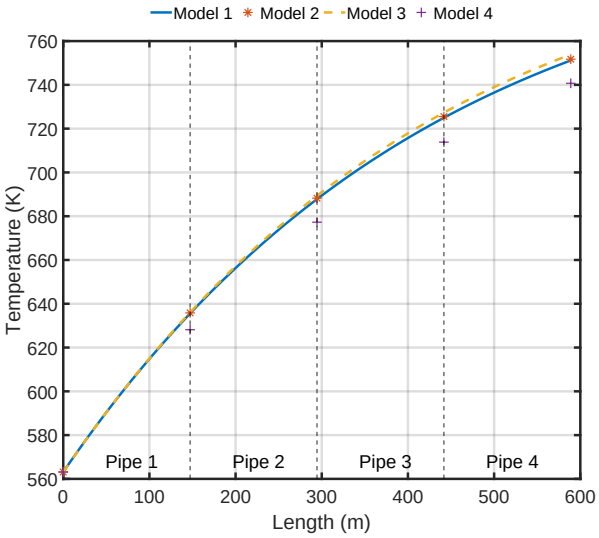

FIG. 4.34: Comparison of the network temperature variation with respect to the pipe length.

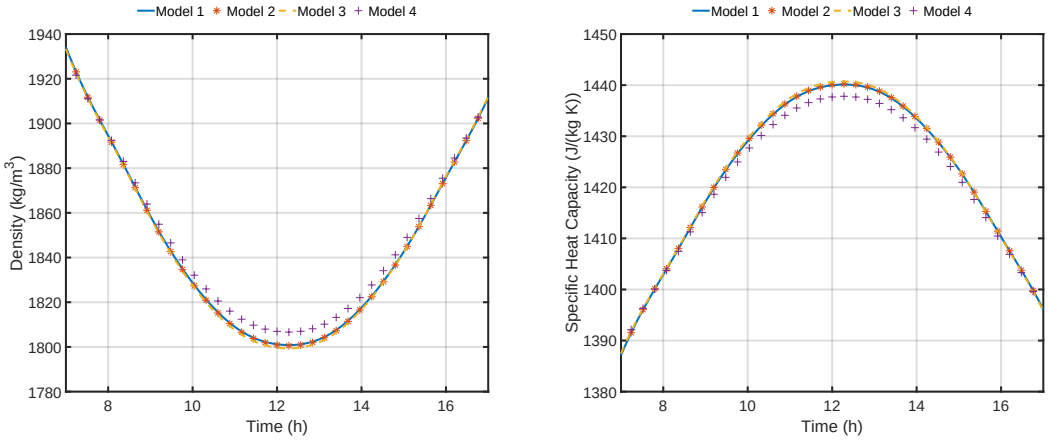

FIG. 4.35: Comparison of hourly variation of the network outlet density and specific heat capacity

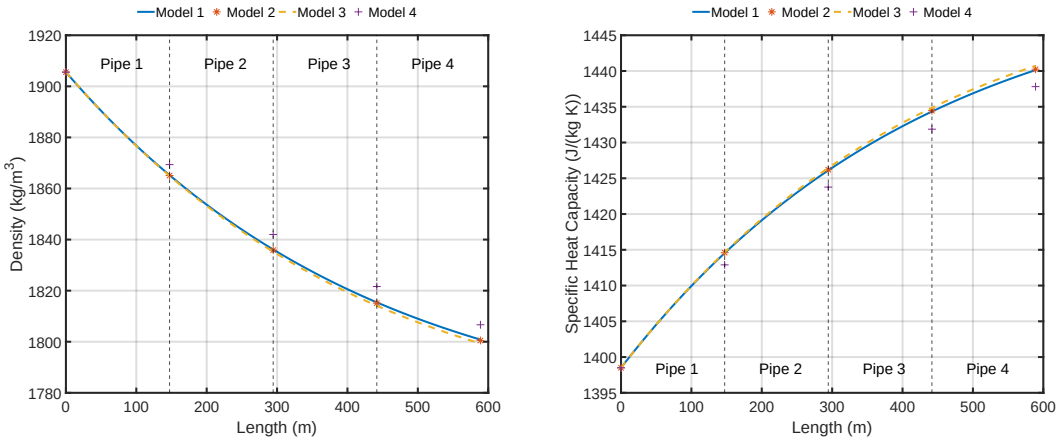

FIG. 4.36: Comparison of the network density and specific heat capacity variations with respect to the pipe length

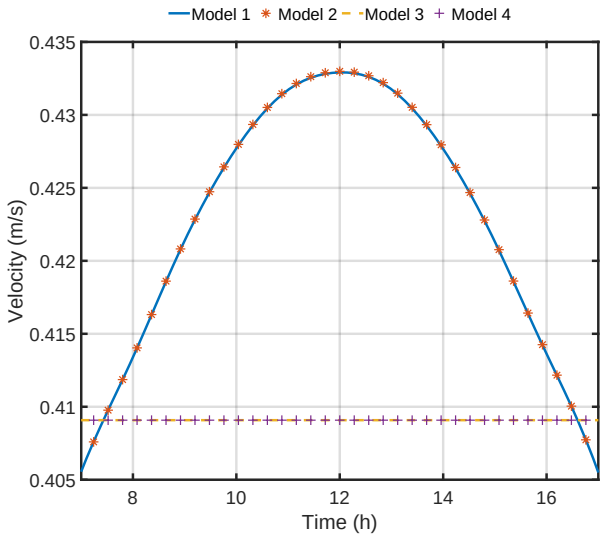

FIG. 4.37: Comparison of hourly variation of the network outlet velocity

models 1 and 3. On the other hand, it is clearly seen that the velocity variations obtained from model 1-2 are also very small, with an order of difference close to

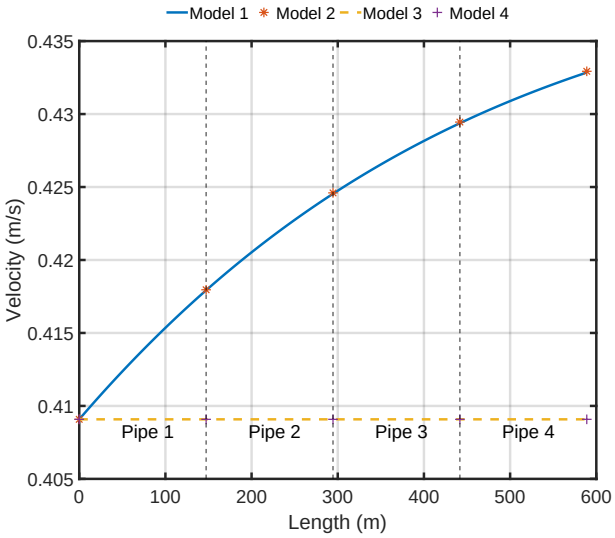

FIG. 4.38: Comparison of the network velocity variation with respect to the pipe length

10^{-2}, which does not affect the variation of other quantities and explains the good agreements between the network models 1-2 and model 3.

Model	n_x	n_t	Runtime (s)
1	10	1000	9.995024
	20	1000	14.893247
	50	1000	33.456786
2	-	1000	5.571756
3	10	1000	1.609925
	20	1000	1.556377
	50	1000	1.723309
4	-	1000	1.080095

TABLE 4.11: Network models comparison with respect to MATLAB runtime.

Finally, in a similar way to the single pipe models, the computation run times for network model 1 and 3 were compared for a number of different space

discretization points, as listed in Table 4.11. It is clearly demonstrated that model 3 runs much quicker and saves great amount of time in the case of single row of PTCs simulation. While the first model takes almost 20 times (20x) more time to produce the results obtained for the case of 50 space grid points.

In what follows, the proposed simplified network models 2-4 are compared with the network model 1 for the case of small network system comprising of 5 PTC rows.

Multiple Rows Network

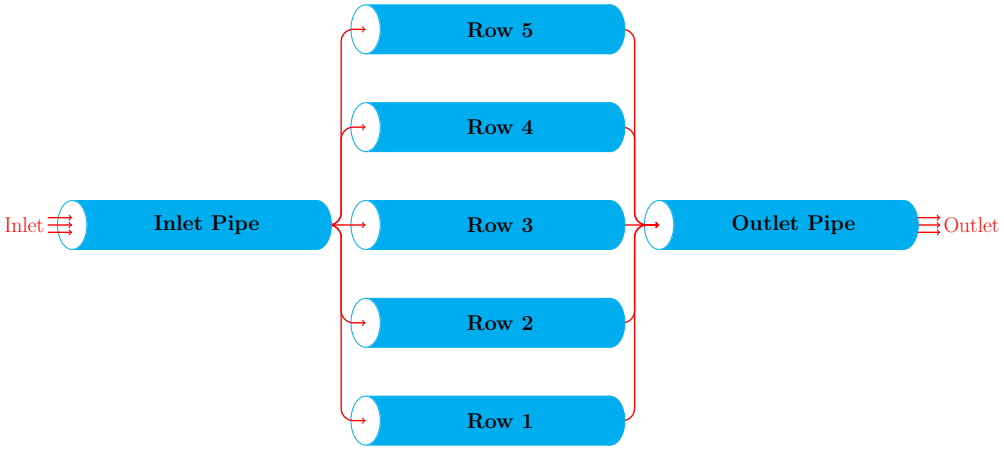

FIG. 4.39

In this case, a network of 5 rows of PTCs with each row has 4 collectors is assumed, as shown in Fig. 4.39. Similar simulation settings are set for this case which involves 50 space subdivisions and 1000 time subdivisions; molten salt is also kept as the HTF. Figs. 4.40-4.45 illustrate the obtained numerical results for the network case, where the distribution of the selected quantities (temperature, density, specific heat capacity and velocity) are shown in the network system; the time variations of the outlet values for all models are plotted.

Fig. 4.40 shows the temperature distribution over the 5-rows network system, where the peak of the incident beam radiation at midday is considered with the inlet values of temperature being at 563.15 K. The inlet to outlet variation of the temperature shows a continuous behavior in the nodes and an increasing trend

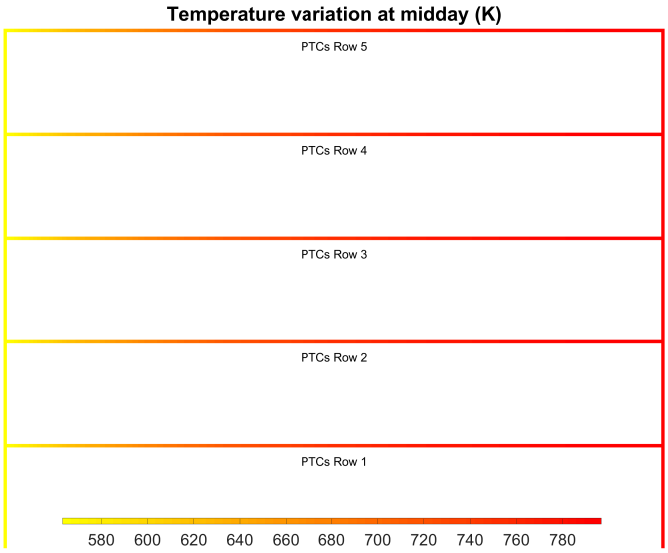

FIG. 4.40: Distribution of the temperature in the network pipes model using model 3.

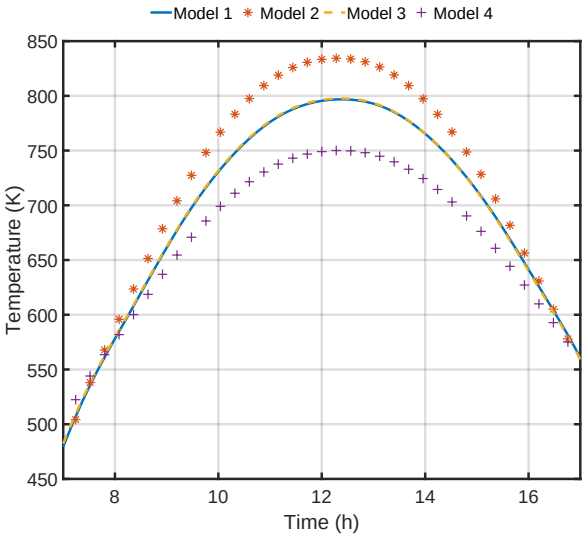

FIG. 4.41: Comparison of hourly variation of the network outlet temperature.

from the inlet to the outlet. While in Fig. 4.41, the outlet temperature for all models appears to behave in a similar way to previous cases. The obtained temperature values using models 1 and 3 are in very good agreement, with a maximum value close to 797 K, while the resulting temperature from model 2 and 4 are not accurate, due to the low order approximation in space as previously explained.

Similarly, Fig. 4.42 shows the density and specific heat capacity distribution over the network system at midday. The inlet to outlet variation of the density and specific heat capacity also show a continuous behavior in the nodes, with a decreasing trend for density and increasing trends for specific heat capacity. The obtained outlet time variations of the density and specific heat capacity for models 1-4 are shown in Fig. 4.43, where the maximum outlet values observed are: 2025 kg/m^3 and 1450 J/(kg K), respectively. The obtained values using models 1 and 3 are in very good agreement while model 2 and 4 are again inaccurate for these quantities.

Concerning the velocity, Fig. 4.44 shows the velocity distribution over the same network system at midday. For this quantity, the inlet to outlet variation shows a discontinuous behavior in the nodes; the velocity in the rows is lower than that of the inlet and outlet pipes, with the inlet/outlet value being 1.022 m/s^3 and the velocity in the rows being 0.204 m/s. This is due to the flow from one pipe to several pipes or vice versa, and the implementation of the proposed coupling conditions between the pipes. The obtained outlet time variations of the velocity for models 1-4 are shown in Fig. 4.45. Similar observation to the previous cases are also made in this case; the velocity is assumed to be constant for model 3-4 as shown in the figure. In addition, the velocity variations obtained from model 1-2 are also very small, thus not affecting the variation of other quantities and explaining the good agreements between the network models 1 and 3.

Finally, and similarly to the previous cases, the computation run times for each network model were compared for different number of space discretization points as shown in Table 4.12. It is clearly demonstrated that model 3 and it space-independent version (model 4) run much quicker and save great amount of time in the 5-rows network case. While the first model take almost 25 times (25x) more time to produce the results obtained in the case of 50 space grid points.

To be precise, the proposed model 3 can be used for very large networks simulations as quicker run times are expected compared to the fully developed

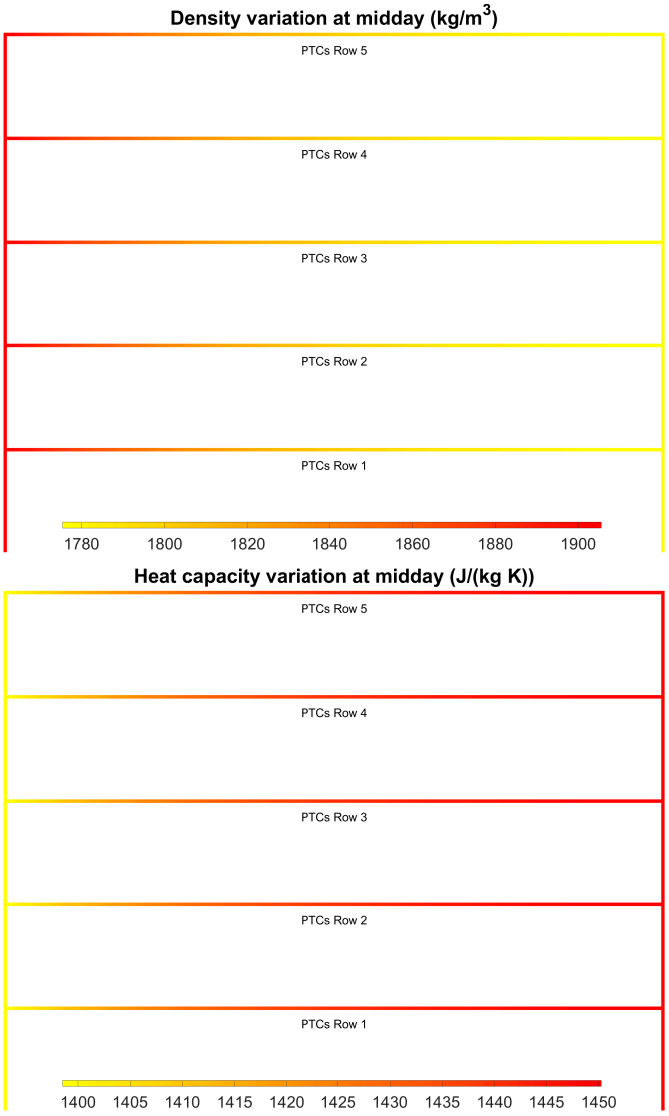

FIG. 4.42: Distribution of the density and specific heat capacity in the network pipes model

heat transfer model. In the next section, the case of 400 rows of PTCs is assumed as a realistic case study of the NOOR I solar field.

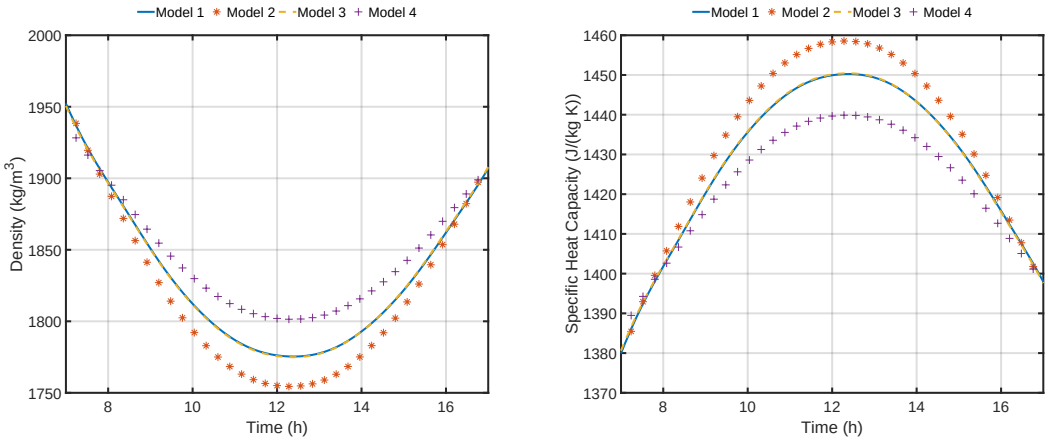

FIG. 4.43: Comparison of hourly variation of the network outlet density and specific heat capacity

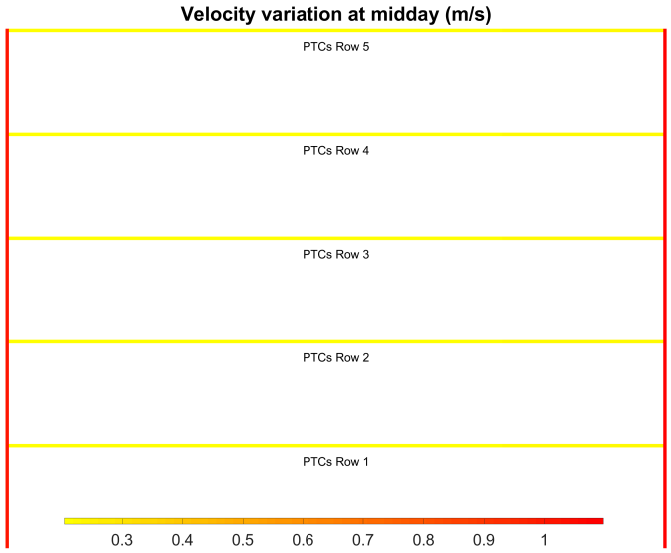

FIG. 4.44: Distribution of the velocity in the network pipes model

Very Large Network: NOOR I Solar Field

In this final section, the case of 400 rows of PTCs is assumed, simulating the actual solar field design of NOOR I power station in Ouarzazate, Morocco, see

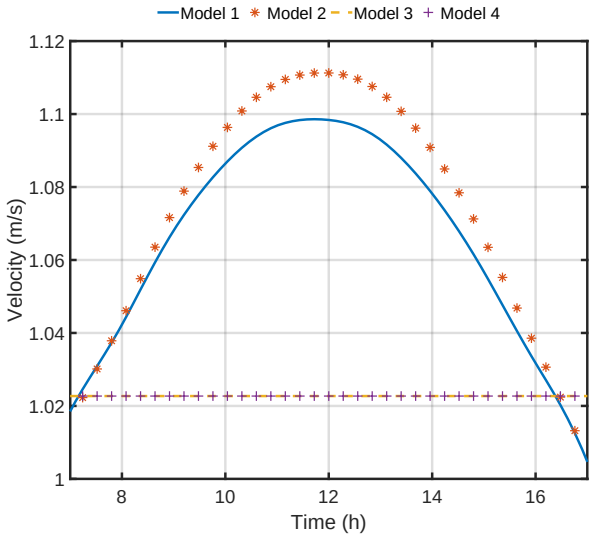

FIG. 4.45: Comparison of hourly variation of the network outlet velocity

Model	n_x	n_t	Runtime (s)
1	10	1000	13.662414
	20	1000	22.113033
	50	1000	56.032248
2	-	1000	6.086647
3	10	1000	2.281388
	20	1000	2.349400
	50	1000	2.383653
4	-	1000	1.686074

TABLE 4.12: Network models comparison with respect to MATLAB runtime.

Fig. 4.46. Similar simulation settings are also set for this case which involves 50 space subdivisions and 1000 time subdivisions, while once again keeping molten salt as the HTF. Figs. 4.47-4.48 illustrate the obtained numerical results for the NOOR I solar field, where the outlet variations of the temperature, density, specific heat capacity are plotted.

Fig. 4.47 shows the outlet temperature using model 3; it appears to behave

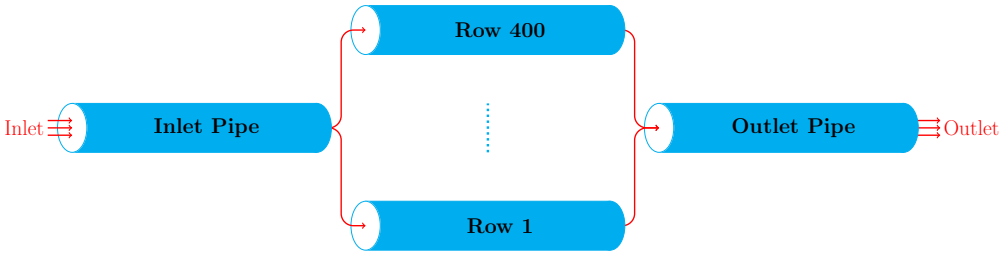

FIG. 4.46

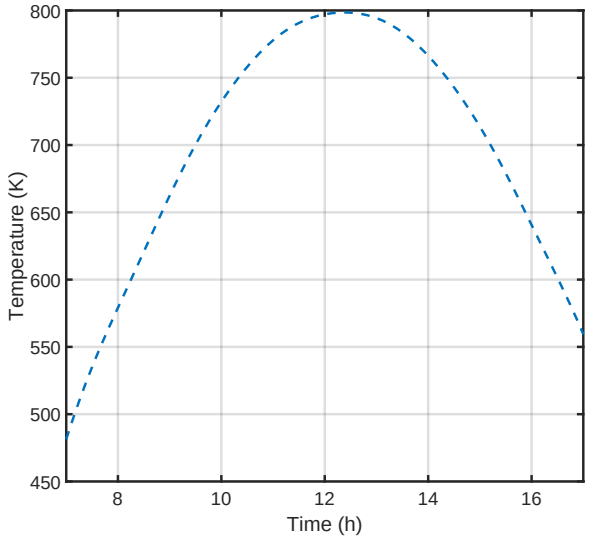

FIG. 4.47: Comparison of hourly variation of the network outlet temperature.

in similar way to previous cases. The outlet temperature has a maximum value of approximately 798 K. On the other hand, in Fig. 4.48, the outlet density and specific heat capacity is also presented using model 3. The maximum observed density and specific heat capacity values are 2024 kg/m^3 and 1451 J/(kg K), respectively.

Finally, in order to show the importance of using model 3 in the case of very large network system, the computation run times for model 1 and 3 are compared and presented in Table 4.13. It is clearly proved that model 3 runs much quicker and saves great amount of time for the large solar field network. As for the first

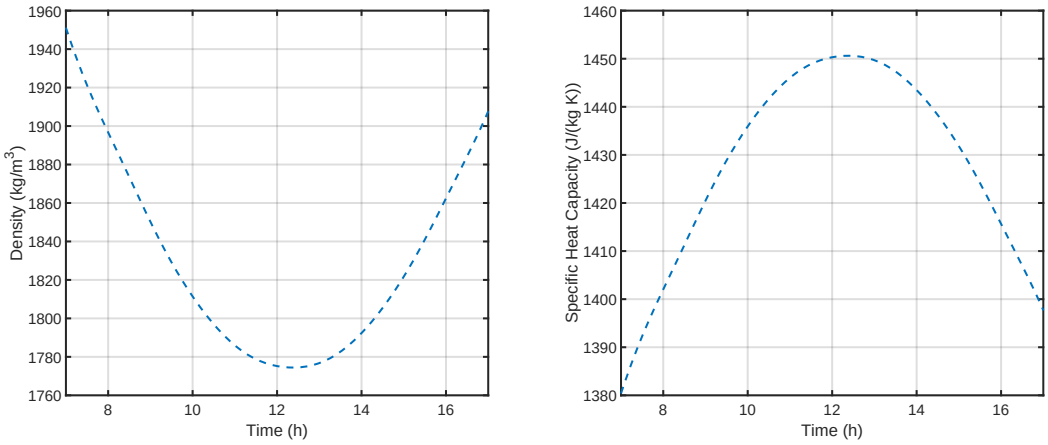

FIG. 4.48: Comparison of hourly variation of the network outlet density and specific heat capacity

Model	n_x	n_t	Runtime (s)
1	50	1000	53058.027463
3	50	1000	104.224693

TABLE 4.13: Network models comparison with respect to MATLAB runtime.

model, it takes almost 15 hours to produce the intended results, compared to only about 2 minutes for model 1, which is a very huge difference in term of the computation costs for the two models.

Conclusion

The present thesis explores the modeling, simulation and optimization of parabolic trough power plants, relying on various models and different approaches and touching on distinct aspects of these complex systems, with the main objective of enhancing the accuracy and thermal efficiency of such power plants.

In chapter 1, a comprehensive exploration of parabolic trough power plants is presented, covering their solar field design, components, heat transfer mechanisms, and efficiency enhancement strategies.

Chapter 2 focuses on the modeling and simulation of solar fields, while simultaneously emphasizing the undeniable importance of parabolic trough power plants (PTPPs) as a means of generating electrical energy from solar radiation. It extensively covers a comprehensive mathematical model tailored to simulate heat transfer within networks of parabolic trough collectors (PTCs) using various heat transfer fluids (HTFs) such as thermal oil and molten salt, while also exploring the potential enhancements via nanofluids. Real-world data from the NOOR I solar power plant validates the model's accuracy in replicating PTC network behavior under realistic conditions.

Investigated key aspects include detailed mathematical models characterizing fluid dynamics within the tube network, and accounting for crucial parameters such as velocity, pressure, temperature, viscosity, heat capacity, and density. In addition, this chapter delves into the temperature-dependent thermal properties of different HTFs; being of essential importance for more precise modeling. Time-space dependent heat transfer models are presented alongside their simplified space-independent models in order to reduce computational complexities in handling large network problems, particularly relevant to PTPPs consisting of multiple parallel rows of solar collectors.

The evolution of the model is evident: it progresses from a single pipe model to integrate multiple tubes in a network, while seeking efficiency without compromising accuracy. The algorithmic development is documented step by

step, initially introducing algorithms for single pipes and advancing to handle the complexities of network systems. The chapter continuously simplifies and refines the models, yet it emphasizes computational efficiency and ensures fidelity to real-world behavior.

Overall, this chapter offers a deep dive into the mathematical modeling and simulation of PTPPs, providing a comprehensive understanding of their functioning and the potential for optimization in both planning and operational phases. The continual refinement and simplification of models highlight the pursuit of efficiency without compromising accuracy. Accordingly, this chapter serves as a valuable resource for understanding and optimizing parabolic trough systems for sustainable energy production.

On the other hand, **Chapter 3** provides an in-depth analysis of the enhancement of the thermal performance of parabolic trough power plants (PTPPs) through the utilization of a simulation model designed for system optimization. The emphasis of the chapter rests on optimizing various parameters within larger network systems; an area relatively understudied despite extensive research on individual parabolic trough collectors (PTCs). The main objective of the chapter is to from a mathematical optimization problem aimed at maximizing output energy by considering diverse heat transfer fluids (HTFs) and system parameters.

This chapter comprises various sections, including an introduction of the power functional and its role in PTPP optimization, and followed by the formulation of the optimization problem, where objectives and constraints are defined. The chapter proposes in detailing algorithmic approaches employed for maximizing PTPP efficiency.

The primary purpose is to maximize the net energy performance functional, aligned with the power functional presented. The chapter explores both single-parameter optimization, focusing on the pressure drop within the network system, and the multivariable optimization considering parameters such as inlet velocity, nanoparticle volume fraction, inlet temperature, and pipe diameter ratios.

To solve the nonlinear energy performance functional while adhering to specified constraints, this chapter introduces an approach involving a sequence of approximate minimization problems utilizing the interior-point method. The implementation, as depicted in the provided algorithm within MATLAB, facilitates numerical experiments and optimization procedures. These procedures involve a comparative analysis using the case of NOOR I plant in Morocco,

evaluating different HTFs and model parameters for diverse optimization scenarios.

Ultimately, this chapter provides a systematic framework for optimizing PTPPs; a crucial aspect in achieving maximum energy output. The presented model and optimization algorithms offer a robust foundation for exploring diverse scenarios, thus aiding in the effective design and operation of these vital renewable energy systems.

In **chapter 4**, the focus shifts toward the practical implementation and simulation of the presented models across various examples, employing MATLAB codes to explore different numerical scenarios. The chapter begins by validating the single pipe model against existing literature, using solar radiation and ambient temperature data specific to the Ouarzazate region in Morocco.

The application of the network model to NOOR I power plant takes into account the case of 8-pipe network configuration, allowing for potential optimization of the power functional, with the optimal pressure drop as the primary outcome of the optimization process. In the chapter, in-depth examination of various collector row designs beyond the standard series arrangement is presented, including three alternative designs in order to investigate potential enhancements in net power output.

Numerical experiments and optimization procedures are conducted within the context of the NOOR I solar plant in Morocco, examining different nanoparticles and varying volume fractions to assess their impact on the system.

In addition, this chapter meticulously compares and simulates the presented models across different scenarios. It dedicates subsections to examine single-pipe cases, PTCs connected in series, and larger network configurations resembling the NOOR I solar field. Each case study involves computing simulation run times for different time and space discretization, providing valuable insights into the computational costs associated with each model.

Overall, this chapter serves as a practical guide of the presented models, offering insights into their applicability across various settings and configurations. The comparisons and simulations performed shed light on the computational efficiency and efficacy of the various models in different scenarios, laying the groundwork for their potential real-world implementation and optimization in solar power plant design and operation.

Bibliography

[1] **Bakhti, H.**, I. Gasser, S. Schuster **and** E. Parfenov, **?**Modelling, simulation and optimisation of parabolic trough power plants, **?** *European Journal of Applied Mathematics*, **jourvol** 34, **number** 3, 592–615, 2023. DOI: 10.1017/S0956792522000274.

[2] **Bakhti, H. and** I. Gasser, **?**Modeling and simulation of parabolic trough collectors using nanofluids: Application to noor i plant in ouarzazate, morocco, **?** *Lecture Notes in Computational Science and Engineering*, **jourvol** 148, **pages** 21–33, 2023, ISSN: 21977100. DOI: 10.1007/978-3-031-45158-4_2/COVER.

[3] **Bakhti, H. and** I. Gasser, **?**Network-based analysis and optimization of parabolic trough power plant operating with nanofluids: Application to ouarzazate solar power station in morocco, **?** *Submitted to International Journal of Applied and Computational Mathematics, Springer Nature*, 2023.

[4] **Bakhti, H. and** I. Gasser, **?**Modeling and simulation of parabolic trough power plant using molten salt: Case study of noor i solar power station in ouarzazate, morocco, **?** **in***The 9th International Conference on Modeling, Simulation and Applied Optimization, AIP Conference Proceedings* 2023.

[5] Directorate-General for Energy (DG ENER), *Renewable Energy Targets*, 2022. **url**: https://energy.ec.europa.eu/topics/renewable-energy_en (**urlseen** 29/12/2022).

[6] Eurostat, *Share of renewable energy in gross final energy consumption by sector, https://ec.europa.eu.*

[7] T. Bouhal, Y. Agrouaz, T. Kousksou, A. Allouhi, T. El Rhafiki, A. Jamil **and** M. Bakkas, **?**Technical feasibility of a sustainable Concentrated Solar Power in Morocco through an energy analysis, **?** *Renewable and Sustainable Energy Reviews*, **jourvol** 81, **pages** 1087–1095, 2018, ISSN: 18790690. DOI: 10.1016/j.rser.2017.08.056.

[8] B. El Ghazzani, D. Martinez Plaza, R. Ait El Cadi, A. Ihlal, B. Abnay **and** K. Bouabid, **?**Thermal plant based on parabolic trough collectors for industrial process heat generation in morocco, **?** *Renewable Energy*, **jourvol** 113, **pages** 1261–1275, 2017, ISSN: 0960-1481. DOI: https://doi.org/10.1016/j.renene.2017.06.063. **url**: https://www.sciencedirect.com/science/article/pii/S0960148117305682.

[9] A. J. Abdulhamed, N. M. Adam, M. Z. A. Ab-Kadir **and** A. A. Hairuddin, **?**Review of solar parabolic-trough collector geometrical and thermal analyses, performance, and applications, **?** *Renewable and Sustainable Energy Reviews*, **jourvol** 91, **pages** 822–831, 2018, ISSN: 1364-0321. DOI: https://doi.org/10.1016/j.rser.2018.04.085. **url**: https://www.sciencedirect.com/science/article/pii/S1364032118303046.

[10] National Renewable Energy Laboratory (NREL), *Concentrating Solar Power Projects (SolarPACES), https://solarpaces.nrel.gov/by-technology/parabolic-trough*.

[11] M. Benasla, D. Hess, T. Allaoui, M. Brahami **and** M. Denaï, **?**The transition towards a sustainable energy system in Europe: What role can North Africa's solar resources play? **?** *Energy Strategy Reviews*, **jourvol** 24, **pages** 1–13, 2019, ISSN: 2211467X. DOI: 10.1016/j.esr.2019.01.007.

[12] M. Mahlooji, L. Gaudard, B. Ristic **and** K. Madani, **?**The importance of considering resource availability restrictions in energy planning: What is the footprint of electricity generation in the Middle East and North Africa (MENA), **?** *Science of the Total Environment*, **jourvol** 717, **page** 135035, 2020, ISSN: 18791026. DOI: 10.1016/j.scitotenv.2019.135035.

[13] F. Trieb, C. Schillings, T. Pregger **and** M. O'Sullivan, **?**Solar electricity imports from the Middle East and North Africa to Europe, **?** *Energy Policy*, **jourvol** 42, **pages** 341–353, 2012, ISSN: 03014215. DOI: 10.1016/j.enpol.2011.11.091.

[14] N. Komendantova, A. Patt **and** K. Williges, **?**Solar power investment in North Africa: Reducing perceived risks, **?** *Renewable and Sustainable Energy Reviews*, **jourvol** 15, **number** 9, **pages** 4829–4835, 2011, ISSN: 13640321. DOI: 10.1016/j.rser.2011.07.068.

[15] Moroccan Agency for Solar Energy (MASEN), *https://www.masen.ma/*.

[16] Z. Aqachmar, A. Allouhi, A. Jamil, B. Gagouch **and** T. Kousksou, **?**Parabolic trough solar thermal power plant Noor I in Morocco, **?** *Energy*, **jourvol** 178, **pages** 572–584, 2019, ISSN: 03605442. DOI: 10.1016/j.energy.2019.04.160.

[17] M. Boulakhbar, B. Lebrouhi, T. Kousksou, S. Smouh, A. Jamil, M. Maaroufi **and** M. Zazi, **?**Towards a large-scale integration of renewable energies in Morocco, **?** *Journal of Energy Storage*, **jourvol** 32, **page** 101 806, 2020, ISSN: 2352152X. DOI: 10.1016/j.est.2020.101806.

[18] A Lepaute, **?**La chaleur solaire et ses applications industrielles., **?** *L'Astronomie*, **jourvol** 2, **pages** 197–199, 1883.

[19] U. Herrmann, B. Kelly **and** H. Price, **?**Two-tank molten salt storage for parabolic trough solar power plants, **?** *Energy*, **jourvol** 29, **number** 5, **pages** 883–893, 2004, SolarPACES 2002, ISSN: 0360-5442. DOI: https://doi.org/10.1016/S0360-5442(03)00193-2. **url**: https://www.sciencedirect.com/science/article/pii/S0360544203001932.

[20] M. Chaanaoui, S. Vaudreuil **and** T. Bounahmidi, **?**Benchmark of Concentrating Solar Power Plants: Historical, Current and Future Technical and Economic Development, **?** *Procedia Computer Science*, **jourvol** 83, **pages** 782–789, 2016, ISSN: 18770509. DOI: 10.1016/j.procs.2016.04.167.

[21] Y. Krishna, M. Faizal, R. Saidur, K. Ng **and** N. Aslfattahi, **?**State-of-the-art heat transfer fluids for parabolic trough collector, **?** *International Journal of Heat and Mass Transfer*, **jourvol** 152, **page** 119 541, 2020, ISSN: 0017-9310. DOI: https://doi.org/10.1016/j.ijheatmasstransfer.2020.119541. **url**: https://www.sciencedirect.com/science/article/pii/S0017931019359411.

[22] G Cohen **and** D Kearney, **?**Improved parabolic trough solar electric systems based on the segs experience, **?** **in***Proceeding of the ASES Annual Conference. SOLAR* **volume** 94, 1994, **pages** 147–150.

[23] S. D. Odeh, G. L. Morrison **and** M. Behnia, **?**Modelling of parabolic trough direct steam generation solar collectors, **?** *Solar Energy*, **jourvol** 62, **number** 6, **pages** 395–406, 1998, ISSN: 0038092X. DOI: 10.1016/S0038-092X(98)00031-0.

[24] M. K. G. Deshmukh, M. Sameeroddin, D. Abdul **and** M. Abdul Sattar, **?**Renewable energy in the 21st century: A review, **?** *Materials Today: Proceedings*, 2022, ISSN: 22147853. DOI: 10.1016/j.matpr.2021.05.501.

[25] M. S. B. Fares **and** S. Abderafi, **?**Water consumption analysis of moroccan concentrating solar power station, **?** *Solar Energy*, **jourvol** 172, **pages** 146–151, 2018, State of the art Solar Energy Materials, ISSN: 0038-092X. DOI: https://doi.org/10.1016/j.solener.2018.06.003. **url**: https://www.sciencedirect.com/science/article/pii/S0038092X18305437.

[26] A. Fernández-García, E. Zarza, L. Valenzuela **and** M. Pérez, **?**Parabolic-trough solar collectors and their applications, **?** *Renewable and Sustainable Energy Reviews*, **jourvol** 14, **number** 7, **pages** 1695–1721, 2010, ISSN: 13640321. DOI: 10.1016/j.rser.2010.03.012.

[27] M. S. Shahin, M. F. Orhan **and** F. Uygul, **?**Thermodynamic analysis of parabolic trough and heliostat field solar collectors integrated with a Rankine cycle for cogeneration of electricity and heat, **?** *Solar Energy*, **jourvol** 136, **pages** 183–196, 2016, ISSN: 0038092X. DOI: 10.1016/j.solener.2016.06.057.

[28] P. Svoboda, E. Dagan **and** G. Kenan, **?**Comparison of direct steam generation vs. htf technology for parabolic trough solar power plants: Performance and cost, **?** *Solar Engineering*, **pages** 381–388, 1997.

[29] M. Eck, M. Eickhoff, J. F. Feldhoff, P. Fontela, N. Gathmann, M Meyer-Grünefeldt, S Hillebrand **and** J. Schulte-Fischedick, **?**Direct steam generation in parabolic troughs at 500 c-first results of the real-diss project, **?** *17th SolarPACES, Granada, Spain*, 2011.

[30] Y. Wang, Q. Liu, J. Lei **and** H. Jin, **?**A three-dimensional simulation of a parabolic trough solar collector system using molten salt as heat transfer fluid, **?** *Applied Thermal Engineering*, **jourvol** 70, **number** 1, **pages** 462–476, 2014, ISSN: 13594311. DOI: 10.1016/j.applthermaleng.2014.05.051.

[31] H. Xu, Y. Li, J. Sun **and** L. Li, **?**Transient model and characteristics of parabolic-trough solar collectors: Molten salt vs. synthetic oil, **?** *Solar Energy*, **jourvol** 182, **pages** 182–193, 2019, ISSN: 0038092X. DOI: 10.1016/j.solener.2019.02.047.

[32] S. Zhang, M. Liu, Y. Zhao, J. Liu **and** J. Yan, **?**Energy and exergy analyses of a parabolic trough concentrated solar power plant using molten salt during the start-up process, **?** *Energy*, **jourvol** 254, **page** 124 480, 2022, ISSN: 03605442. DOI: 10.1016/j.energy.2022.124480.

[33] A. Kasaeian, S. Daviran, R. D. Azarian **and** A. Rashidi, **?**Performance evaluation and nanofluid using capability study of a solar parabolic trough collector, **?** *Energy Conversion and Management*, **jourvol** 89, **pages** 368–375, 2015, ISSN: 01968904. DOI: 10.1016/j.enconman.2014.09.056.

[34] A. K. Tiwar, V. Kumar, Z. Said **and** H. K. Paliwal, **?**A review on the application of hybrid nanofluids for parabolic trough collector: Recent progress and outlook, **?** *Journal of Cleaner Production*, **jourvol** 292, **page** 126 031, 2021, ISSN: 09596526. DOI: 10.1016/j.jclepro.2021.126031.

[35] D. do Carmo Zidan, C. Brasil Maia **and** M. Reza Safaei, **?**Performance evaluation of various nanofluids for parabolic trough collectors, **?** *Sustainable Energy Technologies and Assessments*, **jourvol** 50, **page** 101 865, 2022, ISSN: 22131388. DOI: 10.1016/j.seta.2021.101865.

[36] H. Olia, M. Torabi, M. Bahiraei, M. H. Ahmadi, M. Goodarzi **and** M. R. Safaei, **?**Application of Nanofluids in Thermal Performance Enhancement of Parabolic Trough Solar Collector: State-of-the-Art, **?** *Applied Sciences 2019, Vol. 9, Page 463*, **jourvol** 9, **number** 3, **page** 463, 2019, ISSN: 2076-3417. DOI: 10.3390/APP9030463. **url**: https://www.mdpi.com/2076-3417/9/3/463/htmhttps://www.mdpi.com/2076-3417/9/3/463.

[37] Z. A. Nawsud, A. Altouni, H. S. Akhijahani **and** H. Kargarsharifabad, **?**A comprehensive review on the use of nano-fluids and nano-PCM in parabolic trough solar collectors (PTC), **?** *Sustainable Energy Technologies and Assessments*, **jourvol** 51, **page** 101 889, 2022, ISSN: 22131388. DOI: 10.1016/j.seta.2021.101889.

[38] A. Allouhi, M. Benzakour Amine, R. Saidur, T. Kousksou **and** A. Jamil, **?**Energy and exergy analyses of a parabolic trough collector operated with nanofluids for medium and high temperature applications, **?** *Energy Conversion and Management*, **jourvol** 155, **pages** 201–217, 2018, ISSN: 01968904. DOI: 10.1016/j.enconman.2017.10.059.

[39] R. Forristall, **?**Heat transfer analysis and modeling of a parabolic trough solar receiver implemented in engineering equation solver, **?** National Renewable Energy Lab., Golden, CO.(US), techreport, 2003.

[40] M. Qu, D. H. Archer **and** H. Yin, **?**A linear parabolic trough solar collector performance model, **?** *Proceedings of the Energy Sustainability Conference 2007*, **pages** 663–670, 2007. DOI: 10.1115/ES2007-36052. **url**: https://dx.doi.org/10.1115/ES2007-36052.

[41] M. El Jai **and** F. Chalqi, **?**A modified model for parabolic trough solar receiver, **?** *Americain Journal of Engineerin Research (AJER)*, **jourvol** 2, **number** 05, **pages** 200–211, 2013.

[42] S. D. Odeh **and** G. L. Morrison, **?**Optimization of parabolic trough solar collector system, **?** *International Journal of Energy Research*, **jourvol** 30, **number** 4, **pages** 259–271, 2006, ISSN: 0363907X. DOI: 10.1002/er.1153. **url**: https://onlinelibrary.wiley.com/doi/full/10.1002/er.1153https://onlinelibrary.wiley.com/doi/abs/10.1002/er.1153https://onlinelibrary.wiley.com/doi/10.1002/er.1153.

[43] A. Baghernejad **and** M. Yaghoubi, **?**Genetic algorithm for multi-objective exergetic and economic optimization of parabolic trough collectors integration into Combined Cycle System (ISCCS), **?** *ASME 2010 10th Biennial Conference on Engineering Systems Design and Analysis, ESDA2010*, **jourvol** 1, **pages** 289–297, 2010. DOI: 10.1115/ESDA2010-25137. **url**: https://dx.doi.org/10.1115/ESDA2010-25137.

[44] T. Stuetzle, N. Blair, J. W. Mitchell **and** W. A. Beckman, **?**Automatic control of a 30 MWe SEGS VI parabolic trough plant, **?** *Solar Energy*, **jourvol** 76, **number** 1-3, **pages** 187–193, 2004, ISSN: 0038092X. DOI: 10.1016/j.solener.2003.01.002.

[45] K. Hamza, K. P. Laberteaux **and** K. Saitou, **?**An optimization model for parabolic-trough solar power generation systems, **?** *Proceedings of the ASME Design Engineering Technical Conference*, **jourvol** 1, **number** PARTS A AND B, **pages** 1233–1240, 2010. DOI: 10.1115/DETC2010-28997. **url**: https://dx.doi.org/10.1115/DETC2010-28997.

[46] M. J. Montes, A. Abánades, J. M. Martínez-Val **and** M. Valdés, **?**Solar multiple optimization for a solar-only thermal power plant, using oil as heat transfer fluid in the parabolic trough collectors, **?** *Solar Energy*, **jourvol** 83, **number** 12, **pages** 2165–2176, 2009, ISSN: 0038092X. DOI: 10.1016/j.solener.2009.08.010.

[47] J. a. P. Silva **and** R. Castro, **?**Modeling and simulation of a parabolic trough power plant, **?** 2012.

[48] M. Wirz, **?**Optical and thermal modeling of parabolic trough concentrator systems, **?** phdthesis, ETH Zurich, 2014.

[49] S. Rohani, T. P. Fluri, F. Dinter **and** P. Nitz, **?**Modelling and simulation of parabolic trough plants based on real operating data, **?** *Solar Energy*, **jourvol** 158, **pages** 845–860, 2017, ISSN: 0038092X. DOI: 10.1016/j.solener.2017.10.023.

[50] R. V. Padilla, A. Fontalvo, G. Demirkaya, A. Martinez **and** A. G. Quiroga, **?**Exergy analysis of parabolic trough solar receiver, **?** *Applied Thermal Engineering*, **jourvol** 67, **number** 1-2, **pages** 579–586, 2014, ISSN: 13594311. DOI: 10.1016/j.applthermaleng.2014.03.053.

[51] Z. D. Cheng, Y. L. He, K. Wang, B. C. Du **and** F. Q. Cui, **?**A detailed parameter study on the comprehensive characteristics and performance of a parabolic trough solar collector system, **?** *Applied Thermal Engineering*, **jourvol** 63, **number** 1, **pages** 278–289, 2014, ISSN: 13594311. DOI: 10.1016/j.applthermaleng.2013.11.011.

[52] J. E. Pacheco **and** R Gilbert, **?**Overview of recent results of the solar two test and evaluations program, **?** **url**: https://www.osti.gov/biblio/20030592.

[53] S. Schuster **and** I. Gasser, **?**Masterarbeit: Zur modellierung und simulation eines parabolrinnenkraftwerkes, **?** *Department of Mathematics, Universität Hamburg*, 2016.

[54] E. Parfenov **and** I. Gasser, **?**Diplomarbeit: Zur modellierung und simulation eines parabolrinnenkraftwerkes, **?** *Diploma Thesis, Department of Mathematics, Universität Hamburg*, 2011.

[55] I. Gasser **and** M. Kraft, *Modelling and simulation of fires in tunnel networks*, 2008. DOI: 10.3934/nhm.2008.3.691. **url**: https://www.aimsciences.org/article/id/1c4d786b-dc2c-4c98-b113-374bc1a20418.

[56] I. Gasser, *Modelling and simulation of a solar updraft tower*, 2009. DOI: 10.3934/krm.2009.2.191. **url**: https://www.aimsciences.org/article/id/ca3a13bc-1691-422d-841c-1b06dafda11d.

[57] I. Gasser **and** M. Rybicki, **?**Modelling and simulation of gas dynamics in an exhaust pipe, **?** *Applied Mathematical Modelling*, **jourvol** 37, **number** 5, **pages** 2747–2764, 2013, ISSN: 0307-904X. DOI: https://doi.org/10.1016/j.apm.2012.06.010. **url**: https://www.sciencedirect.com/science/article/pii/S0307904X12003666.

[58] I. Gasser, M. Rybicki **and** W. Wollner, **?**Optimal control of the temperature in a catalytic converter, **?** *Computers & Mathematics with Applications*, **jourvol** 67, **number** 8, **pages** 1521–1544, 2014, ISSN: 0898-1221. DOI: https://doi.org/10.1016/j.camwa.2014.02.006. **url**: https://www.sciencedirect.com/science/article/pii/S0898122114000686.

[59] S. Qazi, **?**Chapter 7 - solar thermal electricity and solar insolation, **?** **in***Standalone Photovoltaic (PV) Systems for Disaster Relief and Remote Areas* S. Qazi, **editor**, Elsevier, 2017, **pages** 203–237, ISBN: 978-0-12-803022-6. DOI: https://doi.org/10.1016/B978-0-12-803022-6.00007-1. **url**: https://www.sciencedirect.com/science/article/pii/B9780128030226000071.

[60] C. Brasil, M. Lucas, R. Neumann, G. De, A. Oliveira, M. Alves, M. M. Walczak, P. P. Brito, C. B. Maia, L. R. Neumann **and** G. D. A. Oliveira, **?**A comprehensive review of solar tower csp systems using tes and molten salts, **?** *International Journal of Ambient Energy*, **jourvol** 44, **pages** 1733–1747, 1 **december** 2023, ISSN: 21628246. DOI: 10.1080/01430750.2023.2185814. **url**: https://www.tandfonline.com/doi/abs/10.1080/01430750.2023.2185814.

[61] X. Xu, K. Vignarooban, B. Xu, K. Hsu **and** A. Kannan, **?**Prospects and problems of concentrating solar power technologies for power generation in the desert regions, **?** *Renewable and Sustainable Energy Reviews*, **jourvol** 53, **pages** 1106–1131, 2016, ISSN: 1364-0321. DOI: https://doi.org/10.1016/

j.rser.2015.09.015. **url**: https://www.sciencedirect.com/science/article/pii/S1364032115009855.

[62] M. A. Eltawil, Z. Zhengming **and** L. Yuan, **?**A review of renewable energy technologies integrated with desalination systems, **?** *Renewable and Sustainable Energy Reviews*, **journvol** 13, **number** 9, **pages** 2245–2262, 2009, ISSN: 1364-0321. DOI: https://doi.org/10.1016/j.rser.2009.06.011. **url**: https://www.sciencedirect.com/science/article/pii/S1364032109000987.

[63] J. Fredriksson, M. Eickhoff, L. Giese **and** M. Herzog, **?**A comparison and evaluation of innovative parabolic trough collector concepts for large-scale application, **?** *Solar Energy*, **journvol** 215, **pages** 266–310, 2021, ISSN: 0038-092X. DOI: https://doi.org/10.1016/j.solener.2020.12.017. **url**: https://www.sciencedirect.com/science/article/pii/S0038092X20312652.

[64] P. D. Tagle-Salazar, K. D. Nigam **and** C. I. Rivera-Solorio, **?**Parabolic trough solar collectors: A general overview of technology, industrial applications, energy market, modeling, and standards, **?** *Green Processing and Synthesis*, **journvol** 9, **number** 1, **pages** 595–649, 2020. DOI: doi:10.1515/gps-2020-0059. **url**: https://doi.org/10.1515/gps-2020-0059.

[65] *Rotork: Rotork manufactures electric, pneumatic and hydraulic valve actuators*. **url**: https://www.rotork.com/en.

[66] K. A. R. III, M. J. Prilliman, T. L. Chambers **and** J. R. Raush, **?**Maintenance of a small-scale parabolic trough concentrating solar power plant in louisiana, **?** *International Journal of Sustainable and Green Energy*, **journvol** 6, **number** 6, **pages** 104–111, 2018. DOI: 10.11648/j.ijrse.20170606.12. eprint: https://download.sciencepg.com/pdf/10.11648.j.ijrse.20170606.12. **url**: https://doi.org/10.11648/j.ijrse.20170606.12.

[67] G. Kumaresan, R. Sridhar **and** R. Velraj, **?**Performance studies of a solar parabolic trough collector with a thermal energy storage system, **?** *Energy*, **journvol** 47, **number** 1, **pages** 395–402, 2012, Asia-Pacific Forum on Renewable Energy 2011, ISSN: 0360-5442. DOI: https://doi.org/10.

1016/j.energy.2012.09.036. **url**: https://www.sciencedirect.com/science/article/pii/S0360544212007141.

[68] *Schott | pioneering the impossible.* **url**: https://www.schott.com/en-us/.

[69] A. R. A. Yasseen, S. Istvan **and** F. Istvan, **?**Selective absorber coatings and technological advancements in performance enhancement for parabolic trough solar collector, **?** *Journal of Thermal Science 2022 31:6*, **jourvol** 31, **pages** 1990–2008, 6 **june** 2022, ISSN: 1993-033X. DOI: 10.1007/S11630-022-1634-5. **url**: https://link.springer.com/article/10.1007/s11630-022-1634-5.

[70] P. V. Gharat, S. S. Bhalekar, V. H. Dalvi, S. V. Panse, S. P. Deshmukh **and** J. B. Joshi, **?**Chronological development of innovations in reflector systems of parabolic trough solar collector (ptc) - a review, **?** *Renewable and Sustainable Energy Reviews*, **jourvol** 145, **page** 111002, 2021, ISSN: 1364-0321. DOI: https://doi.org/10.1016/j.rser.2021.111002. **url**: https://www.sciencedirect.com/science/article/pii/S1364032121002926.

[71] J. Gong **and** K. Sumathy, **?**9 - active solar water heating systems, **?** **in***Advances in Solar Heating and Cooling* R. Wang **and** T. Ge, **editors**, Woodhead Publishing, 2016, **pages** 203–224, ISBN: 978-0-08-100301-5. DOI: https://doi.org/10.1016/B978-0-08-100301-5.00009-6. **url**: https://www.sciencedirect.com/science/article/pii/B9780081003015000096.

[72] Eastman, *Therminol VP-1, Heat Transfer Fluid Data Sheet*, 2019. **url**: https://www.therminol.com/.

[73] S. Akbarzadeh **and** M. S. Valipour, **?**Heat transfer enhancement in parabolic trough collectors: A comprehensive review, **?** *Renewable and Sustainable Energy Reviews*, **jourvol** 92, **pages** 198–218, 2018, ISSN: 1364-0321. DOI: https://doi.org/10.1016/j.rser.2018.04.093. **url**: https://www.sciencedirect.com/science/article/pii/S1364032118303186.

[74] K. Ajith, A. Brusly Solomon **and** M. Sharifpur, **?**Chapter 1 - nanofluids for heat transfer augmentation, **?** **in***Materials for Advanced Heat Transfer Systems* **jourser** Woodhead Publishing Series in Energy, S. Vijay, B. Solomon **and** J. Meyer, **editors**, Woodhead Publishing, 2023, **pages** 1–38, ISBN: 978-0-323-90498-8. DOI: https://doi.org/10.1016/B978-0-323-

90498-8.00004-X. **url**: https://www.sciencedirect.com/science/article/pii/B978032390498800004X.

[75] W. A. K. Al-Maliki, H. Q. A. Khafaji, H. A. Abdul Wahhab, H. M. H. Al-Khafaji, F. Alobaid **and** B. Epple, ?Advances in process modelling and simulation of parabolic trough power plants: A review, ? *Energies*, **journvol** 15, **number** 15, 2022, ISSN: 1996-1073. DOI: 10.3390/en15155512. **url**: https://www.mdpi.com/1996-1073/15/15/5512.

[76] Y. Xuan **and** W. Roetzel, ?Conceptions for heat transfer correlation of nanofluids, ? *International Journal of Heat and Mass Transfer*, **journvol** 43, **number** 19, **pages** 3701–3707, 2000, ISSN: 00179310. DOI: 10.1016/S0017-9310(99)00369-5.

[77] I. M. Shahrul, I. M. Mahbubul, S. S. Khaleduzzaman, R. Saidur **and** M. F. Sabri, ?A comparative review on the specific heat of nanofluids for energy perspective, ? *Renewable and Sustainable Energy Reviews*, **journvol** 38, **pages** 88–98, 2014, ISSN: 13640321. DOI: 10.1016/j.rser.2014.05.081.

[78] K. H. Solangi, S. N. Kazi, M. R. Luhur, A. Badarudin, A. Amiri, R. Sadri, M. N. Zubir, S. Gharehkhani **and** K. H. Teng, ?A comprehensive review of thermo-physical properties and convective heat transfer to nanofluids, ? *Energy*, **journvol** 89, **pages** 1065–1086, 2015, ISSN: 03605442. DOI: 10.1016/j.energy.2015.06.105.

[79] Dynalene, Inc., *Dynalene MS-2, Molten Salt Heat Transfer Fluid, https://www.dynalene.com/*, 2020.

[80] J. Brouwer, I. Gasser **and** M. Herty, ?Gas pipeline models revisited: Model hierarchies, nonisothermal models, and simulations of networks, ? *Multiscale Modeling & Simulation*, **journvol** 9, **number** 2, **pages** 601–623, 2011. DOI: 10.1137/100813580. eprint: https://doi.org/10.1137/100813580. **url**: https://doi.org/10.1137/100813580.

[81] H. von Allwörden, I. Gasser **and** M. J. Kamboh, ?Modeling, simulation and optimization of general solar updraft towers, ? *Applied Mathematical Modelling*, **journvol** 64, **pages** 265–284, 2018, ISSN: 0307-904X. DOI: https://doi.org/10.1016/j.apm.2018.07.023. **url**: https://www.sciencedirect.com/science/article/pii/S0307904X18303391.

[82] M. Bauer **and** I. Gasser, **?**Modeling, asymptotic analysis, and simulation of an energy tower, **?** *SIAM Journal on Applied Mathematics*, **jourvol** 72, **number** 1, **pages** 362–381, 2012. DOI: 10.1137/100797977. eprint: https://doi.org/10.1137/100797977. **url**: https://doi.org/10.1137/100797977.

[83] S. A. Kalogirou, **?**Solar Energy Engineering: Processes and Systems: Second Edition, **?** *Solar Energy Engineering: Processes and Systems: Second Edition*, **jourvol** 1, **number** Hybrid photovoltaic/thermal collectors; Photovoltaic applications; Photovoltaic effect; Photovoltaic panels; Photovoltaic systems; PV system design; Related equipment; Semiconductors, **pages** 1–819, 2014. DOI: 10.1016/C2011-0-07038-2. **url**: http://sena.metaproxy.org/proxy/nph-0.pl/en/40/http/www.sciencedirect.com/science/article/pii/B9780123972705000091.

[84] M. Sterner **and** I. Stadler, *Energiespeicher-bedarf, technologien, integration*. Springer-Verlag, 2014.

[85] R. H. Byrd, M. E. Hribar **and** J. Nocedal, **?**An interior point algorithm for large-scale nonlinear programming, **?** *SIAM Journal on Optimization*, **jourvol** 9, **number** 4, **pages** 877–900, 1999, ISSN: 10526234. DOI: 10.1137/S1052623497325107. **url**: https://epubs.siam.org/doi/10.1137/S1052623497325107.

[86] R. H. Byrd, J. C. Gilbert **and** J. Nocedal, **?**A trust region method based on interior point techniques for nonlinear programming, **?** *Mathematical Programming, Series B*, **jourvol** 89, **number** 1, **pages** 149–185, 2000, ISSN: 00255610. DOI: 10.1007/PL00011391. **url**: https://link.springer.com/article/10.1007/PL00011391.

[87] R. A. Waltz, J. L. Morales, J. Nocedal **and** D. Orban, **?**An interior algorithm for nonlinear optimization that combines line search and trust region steps, **?** *Mathematical Programming*, **jourvol** 107, **number** 3, **pages** 391–408, 2006, ISSN: 00255610. DOI: 10.1007/s10107-004-0560-5. **url**: https://link.springer.com/article/10.1007/s10107-004-0560-5.

[88] W. Karush, **?**Minima of Functions of Several Variables with Inequalities as Side Conditions, **?** **in***Traces and Emergence of Nonlinear Programming* Springer Basel, 2014, **pages** 217–245, ISBN: 978-3-0348-0439-4. DOI: 10.

1007/978-3-0348-0439-4_10. **url**: https://doi.org/10.1007/978-3-0348-0439-4_10.

[89] H. W. Kuhn **and** A. W. Tucker, **?**Nonlinear programming, **?** *Traces and Emergence of Nonlinear Programming*, **jourvol** 2, **pages** 247–258, 1951. DOI: 10.1007/978-3-0348-0439-4_11. **url**: https://projecteuclid.org/ebooks/berkeley-symposium-on-mathematical-statistics-and-probability/Proceedings-of-the-Second-Berkeley-Symposium-on-Mathematical-Statistics-and/chapter/Nonlinear-Programming/bsmsp/1200500249.